Leopold-Franzens University of Innsbruck

High temperature superconducting ion traps

A Thesis
submitted to the Faculty of
Mathematics, Computer Science and Physics,
in partial fulfillment of the requirements
for the degree of

MASTER OF SCIENCE

carried out at the Institute for Experimental Physics
under the guidance of Prof. Dr. Rainer Blatt

presented by
DOMINIC SCHÄRTL

MAY 2016

Abstract

Trapped ions are a promising candidate for quantum computation and simulation. Using surface-electrode ion traps with ions trapped close to the surface allows one to realise a scalable structure for a quantum computer. However, the small ion-electrode separation (typically below $100\,\mu\mathrm{m}$) increases the motional heating of the ions and limits the fidelity of two-qubit gates. The origin of this motional heating is not well understood in many ion traps.

The work discussed in this thesis is the start of a project that aims to characterise Johnson noise and another yet unknown noise source in a single ion trap. The high-temperature superconductor YBCO is used as a trap electrode material to switch between the two noise sources by scanning the trap temperature T over the critical temperature T_c. It is the first report of using a high-temperature superconductor as the trap electrode material. For $T < T_\mathrm{c}$ we expect motional heating to be dominated by a local source on the trap surface. On the other hand, for $T > T_\mathrm{c}$, we designed the trap so that motional heating should be dominated by Johnson noise. In this way, the theoretical prediction for motional heating caused by Johnson noise can be tested. We aim to measure the characteristic dependence on the frequency and on the ion's position for both noise sources in order to compare them.

In this thesis we present two different designs of YBCO traps simulated with the infinite plane and the gapless approximation. A new trap mount for an existing cryostat setup was built and enables us to precisely adjust the trap temperature while keeping the surrounding electronics thermally decoupled from the heated trap. The measured heating rates on a YBCO trap were around one phonon per second for trapping frequencies around $1\,\mathrm{MHz}$ at a trap temperature of $10\,\mathrm{K}$. These low heating rates are comparable to the heating rates measured recently in the same setup using silicon substrate traps with the same ion-electrode distance of $226\,\mu\mathrm{m}$. Additionally, trapping frequencies were measured for different voltage settings in order to test the accuracy of the simulations. The measured trapping frequencies were in agreement with the simulations to within a few percent.

Acknowledgements

Many people supported my work for this thesis. I want to thank Rainer Blatt for giving me the opportunity to work in his group and Mike Brownnutt for introducing me to the cryotrap subgroup. My project is based on an idea from Yves Colombe who supervised my work during the last year. I thank him for many enlightening discussions and his patience in reading and correcting the drafts of my thesis. Special thanks also to the other members of the cryotrap group: Kirill Lakhmanskiy introduced me to the cryostat and teached me all technical details for my project: the cleanroom work, glueing and bonding surface traps and loading ions to name just a few things. Philip Holz helped me with the simulations of the traps and also contributed a lot in improving the drafts of my thesis. Muir Kumph patiently discussed with me all the trap electronics in order to improve the trap designs.

I also want to thank my fellow students, my friends and my girlfriend who made my time in Innsbruck wonderful years. Finally, I want to thank my parents who enabled my studies.

Contents

Chapter 1

Introduction

Computer chips are nowadays the base for a wide variety of applications like laptops, mobile phones, smart watches and self-driving cars. All the applications are possible, because the performance of computer chips got better and better. This was achieved by reducing the size of the most important chip component, the transistor. For the past five decades technological research enabled the semiconductor industry to double the amount of transistors per microprocessor every two years. This exponential rate, known as Moore's law [1], has enabled not only applications concerning everyday's life, but also the performance increase of supercomputers. However, according to a recent review [2], it is very likely, that within the next decade the cost will impede this progress even before it is limited by the physics. This would limit the achievable performance of supercomputers.

In many research fields numerical simulations with the help of supercomputers improve the understanding of physics. Despite the massive computing power achieved with the current supercomputers, certain problems remain intractable, e.g. problems in quantum chemistry or material science. Solving these problems, may e.g. simplify the development of a catalyst for carbon sequestration or enable the development of new artificial nanotechnologies [3, 4]. 1982, R. P. Feynmann proposed to solve quantum mechanical problems with a new computer that is based on the laws of quantum mechanics, a quantum computer [5]. It has already been shown that a quantum computer could outperform a classical computer in such quantum simulations [6].

Different physical systems are currently investigated for a possible implementation of a quantum computer [4]. Ions trapped in a radio-frequency (RF) trap seem to be a promising candidate. In several proof-of-principle experiments it was shown that they fulfil all the requirements for quantum computing [7]. The ion's electronic ground state and a metastable excited state can serve as the basic unit of an ion trap quantum computer, the so-called quantum bit (qubit). The motional state of a string of ions is used as a bus and allows the implementation of multi-qubit gates (usually two-qubit-gates) [8, 9]. One major challenge for realising an ion trap quantum computer is scaling up the system to provide control over tens or hundreds of qubits. One approach uses a two dimensional array of single trapped ions [10, 11], while another approach uses several small traps that contain strings of a few ions where ions can be shuttled between the different strings [12]. Both strategies require control over many trap electrodes. Furthermore, in these trap architectures ions have to be confined close to the surface of the traps (with an ion-

electrode distance of less than $100\,\mu\mathrm{m}$) in order to increase the coupling between the ions [13], allow a tight confinement of the ions and fast shuttling [14].

The required complex trap structures can be realised in ion traps with all electrodes in one plane, so-called surface-electrode ion traps [12, 15, 16]. Surface-electrode traps are produced with microfabrication technology. Similar technology is used for semiconductor manufacturing, the fabrication of microelectromechanical systems (MEMS) and the production of solar cells. These techniques got well developed in the semiconductor industry during the last decades. Therefore a wide variety of fabrication techniques are available and can be applied for building surface-electrode traps.

A still unresolved issue in ion traps is motional heating of the ions caused by electric field noise. While motional heating has been studied now for more than two decades and several sources of electric field noise have been investigated, its origin is still unclear in many ion traps [17]. Therefore the heating resulting from the noise is often called anomalous heating [18]. As the motional state is used to perform two-qubit-gates, heating the motional state decreases the fidelity of gate operations reducing the accuracy of computations [9].

One source of electric field noise is Johnson noise generated by thermal motion of charge carriers in a resistor. It is well studied as a voltage noise in electronic circuits and was suspected to be the dominant source of motional heating in some ion traps [19, 20]. While the characteristics of Johnson noise from a resistor are well known [21, 22], its effect on motional heating in ion traps is more complex. Not only the resistance, but also the whole electronic circuit influences the characteristics of motional heating from Johnson noise. The trap design described in this thesis provides a possibility to study the effects of Johnson noise on a trapped ion with minimised influences from surrounding electronics. In order to minimise these influences, our design includes the resistance R directly on the trap chip. In order to provide external control over the resistance, a superconducting trap electrode material is used. The resistance of a superconductor vanishes below its critical temperature T_c and increases by several orders of magnitude within a temperature range of a few kelvins above T_c [23]. For $T < T_\mathrm{c}$ we expect motional heating to be dominated by a local source on the trap surface. Heating up the trap by a few kelvins to be above T_c will not affect this noise source. On the other hand, for $T > T_\mathrm{c}$, the design of the trap is such that motional heating should be dominated by Johnson noise. We aim to characterise both noise sources by measuring their frequency dependence and their dependence on the ion's position, the spatial dependence.

We haven chosen YBCO, a superconductor with a high critical temperature T_c, a so-called high-temperature superconductor as the material for the trap electrodes. YBCO is used in applications like Josephson junctions and SQUIDs (superconducting quantum interference devices) [24]. Therefore microfabrication techniques for YBCO are well developed making it a promising material for our project and for surface-electrode traps in general. Furthermore, our YBCO traps are the first ion traps made of a high-temperature superconducting material.

This thesis is organized as follows. At the beginning of this thesis, chapter 2 provides an introduction into the theory for ion trap quantum information processing and corresponding experimental techniques . Chapter 3 explains the theoretical model for Johnson noise in ion traps and presents examples in the literature for electric field noise mea-

surements in ion traps. Furthermore, in this chapter we explain a sideband spectroscopy method to probe electric field noise with an ion. The development of the trap design is described in chapter 4. Details on the chip fabrication and an introduction to superconductivity are also included in this chapter. The experimental setup is presented in chapter 5, with a focus on a variable-temperature trap mount. Finally, chapter 6 presents the experimental results. The observation of the superconducting transition is described in section 6.1. Section 6.3 presents a comparison between the simulation of trap potential and the experiment and section 6.4 contains the results of heating rate measurements in the YBCO traps.

Chapter 2

Basic concepts of ion trap experiments for quantum information processing

The experiments in this thesis were carried out with $^{40}Ca^{+}$ ions trapped in radio-frequency (RF) ion traps. This chapter provides the theoretical background and an introduction to important experimental techniques required to trap ions and manipulate their electronic state. The operation of RF traps is described in section 2.1. The laser-ion interaction is explained in section 2.2. The relevant electronic states of $^{40}Ca^{+}$ are discussed in section 2.3. Finally, several basic experimental techniques used for trapping ions are presented in section 2.4.

2.1 Ion trap generics

2.1.1 Fundamentals of ion trapping in a Paul trap

RF ion traps or Paul traps are named after their inventor Wolfgang Paul [25, 26]. In these traps ions are confined by a combination of time-dependent (AC) and static (DC) electric fields.

The original Paul trap consists of symmetric hyperbolically shaped electrodes. Figure 2.1 shows an example of a Paul trap, where four electrodes have a hyperbolic shape in the x-y-plane. If a voltage $V(t) = V_{\mathrm{RF}} \cos(\Omega_{\mathrm{RF}} t)/2$ is applied to two opposite electrodes and $V(t) = -V_{\mathrm{RF}} \cos(\Omega_{\mathrm{RF}} t)/2$ is applied to the other two opposite electrodes, then the electric quadrupole potential

$$\Phi(x, y, t) = \frac{V_{\mathrm{RF}}}{2d^2}(x^2 - y^2)\cos(\Omega_{\mathrm{RF}} t) \tag{2.1}$$

is obtained, where $2d$ is the closest separation between two opposite electrodes. In the resulting AC electric field, an ion with charge Q and mass m follows the equations of motion

$$\ddot{x} = -\frac{V_{\mathrm{RF}} Q}{d^2 m} x \cos(\Omega_{\mathrm{RF}} t) \tag{2.2}$$

$$\ddot{y} = \frac{V_{\mathrm{RF}} Q}{d^2 m} y \cos(\Omega_{\mathrm{RF}} t), \tag{2.3}$$

which are special cases of the Mathieu equation [27]. For

$$q = \frac{2QV_{\mathrm{RF}}}{md^2\Omega_{\mathrm{RF}}^2} < 0.908 \tag{2.4}$$

an ion can be trapped stably and its motion is a combination of two distinct oscillations in the x-y-plane [28].

The first oscillation is called micromotion. Its frequency is Ω_{RF} and its amplitude increases with the distance of the ion from the RF minimum. Such a displacement of the ion can occur due to electric stray fields. This creates unwanted effects and should therefore be minimized. These effects and the experimental methods to compensate the micromotion are explained in section 2.4.5.

The second oscillation is called secular motion and has the frequency [30]

$$\omega_{\mathrm{sec}} = \frac{QV_{\mathrm{RF}}}{\sqrt{2}md^2\Omega_{\mathrm{RF}}}. \tag{2.5}$$

The secular frequency ω_{sec} is smaller compared to the micromotion frequency Ω_{RF} by a factor $q/\sqrt{8}$. If the ion is trapped in the RF minimum the micromotion can be neglected in the so-called secular approximation. In this case, the secular motion can also be interpreted as an undriven motion in a pseudopotential which is created by the RF electric field. The pseudopotential is given by

$$U_{\mathrm{pseudo}}(x, y) = \frac{1}{2}m\omega_{\mathrm{sec}}^2(x^2 + y^2). \tag{2.6}$$

If d is small compared to the length of the electrodes along the z-direction, the RF-field produces a pseudopotential tube along the z-axis and the trap is called a linear trap. In this case the secular frequency ω_{sec} in the x- and y-direction are called radial trap frequencies.

The confinement along the z-axis is then achieved by applying a DC voltage to additional electrodes called endcaps. In the centre of the trap the resulting potential $U(x, y, z)$ can be approximated by the quadrupole potential:

$$U(x, y, z) \approx \frac{1}{4}m\omega_{\mathrm{z}}^2(2z^2 - x^2 - y^2), \tag{2.7}$$

with the axial frequency ω_z. The DC field produces anti-trapping in the x- and y-direction. Hence a simulation of the trapping potential must always contain the combination of the DC potential and the RF pseudopotential to ensure confinement in all 3 dimensions. Additionally, the stability of the trap has to be analysed [28].

The hyperbolic electrodes of the Paul trap shown in figure 2.1 provide only limited access for lasers and for collecting the fluorescence light of the ion. Therefore other designs are used for ion traps for quantum information processing, e.g. the Innsbruck trap consists of four blades replacing the four hyperbolic electrodes [7]. In those traps the potential at the trap minimum can still be approximated to be harmonic. Other examples of a modified trap structure are surface-electrode traps presented in the next section.

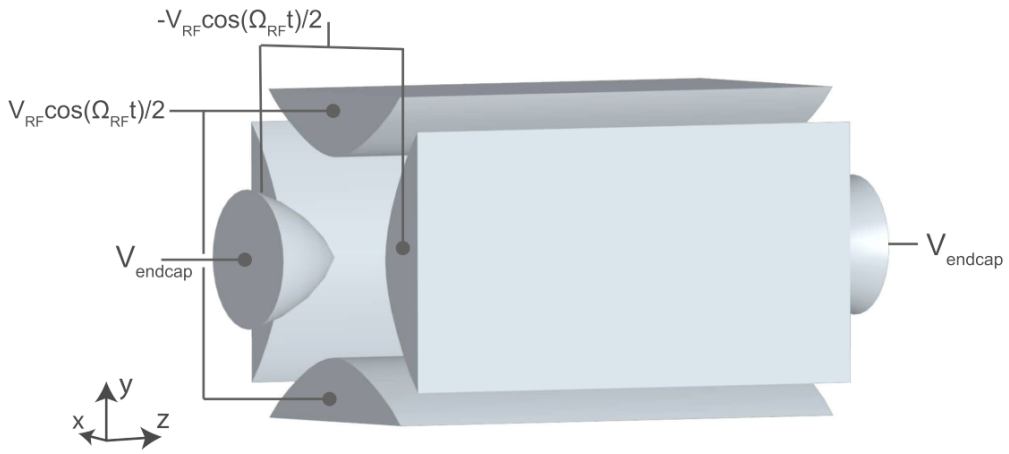

Figure 2.1: Schematic of a linear Paul trap [29]. A sinusoidal RF-voltage applied to the four hyperbolically shaped electrodes creates an harmonic confinement of the ion in the x-y-plane. The elongated form of the electrodes in the z-direction results in a pseudopotential tube along the z-axis. This confines the ion in the x-y-plane. Additional DC voltages on the endcaps result in a confinement along the z-axis. The combination enables one to trap an ion in the centre of the trap. Figure courtesy of Michael Niedermayr.

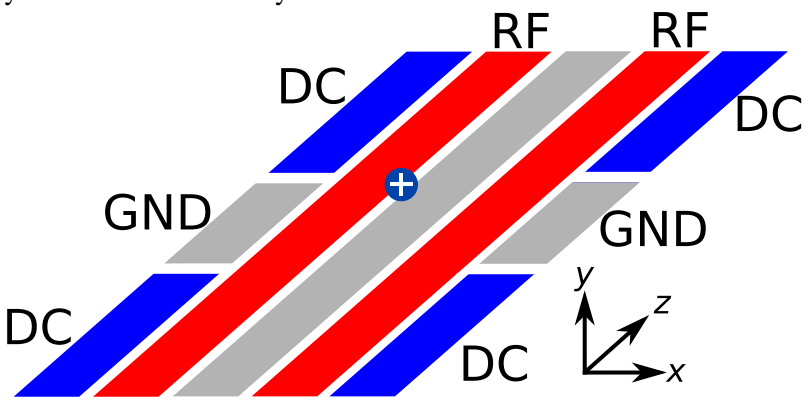

Figure 2.2: Schematic of a linear surface-electrode ion trap. The ion (positive charge, blue point in the schematic) is confined in the x-y-plane by the RF-field created by the RF electrodes (red). Additional DC-electrodes (blue) enable the confinement along the z-axis.

2.1.2 Trapping in a surface-electrode Paul trap

The electrodes of the Paul trap in figure 2.1 can be replaced by electrodes in one plane as shown in figure 2.2. An ion trap with all electrodes in one plane is called surface-electrode ion trap. Comparing the two traps shows the following analogies: Two opposite hyperbolic RF-electrodes are replaced by rectangular surface electrodes. The rest of the surface is RF-grounded and therefore represents the two remaining hyperbolic electrodes. This results in a pseudopotential tube situated above the surface between the two RF-electrodes. The endcaps are now realised by additional DC-electrodes next to the RF-electrodes and confine the ion along the z-axis.

The electrodes on the surface do not produce the ideal quadrupole potential described in the previous section. However, in the vicinity of the trap minimum it is sufficient to consider the leading terms of the multipole expansion. Therefore a combination of DC- and RF-voltages can lead to a harmonic confinement of the ion.

In contrast to the hyperbolic Paul trap, surface-electrode ion traps provide sufficient laser access parallel to the surface in the x-z-plane. The fluorescence of the ion can be collected orthogonal to the surface.

The experiments described in this thesis were performed in a surface-electrode ion trap and its detailed simulation is given in section 4.3.3.

2.2 Laser-ion interaction

Manipulating the electronic state of the ion is a central part for quantum information experiments with ions. It enables one to cool ions in the trap. Furthermore, it is required for spectroscopy of the electronic states of the ion and additionally it forms the base for heating rate measurements. These manipulations are achieved by the interaction of laser light with the ion, which is described in the following.

2.2.1 The laser-ion Hamiltonian in the Schrödinger picture

For two discrete energy levels of an ion with the energy difference $\hbar\omega_\mathrm{a}$ the system is described by the Hamiltonian

$$H_\mathrm{a} = \frac{\hbar}{2}\omega_\mathrm{a}\sigma_3, \tag{2.8}$$

where σ_3 is the third Pauli spin matrix. The eigenvectors have the eigenvalues $\pm\hbar\omega_a/2$ and are the ground state of the ion $|S\rangle$ and an excited D-state $|D\rangle$.

As the ion is trapped in a harmonic potential, the motional states $|n\rangle$ (with $n \in \mathbb{N}_0$) are given by the Hamiltonian

$$H_\mathrm{t} = \hbar\omega(a^\dagger a + \frac{1}{2}), \tag{2.9}$$

with the trap frequency ω corresponding to one of the radial frequencies ω_x, ω_y or to the axial frequency ω_z, the creation operator a and the annihilation operator $a^\dagger$. The eigenvalues are $E_n = \hbar\omega(n + 1/2)$, where n is also called phonon number. For the description of the system only energy differences are relevant and hence the $+1/2$ can be omitted.

The interaction of a travelling wave laser beam with the ion can be described by [30, chapter 3]

$$H_\mathrm{l} = \hbar\Omega(\sigma_+ + \sigma_-)\cos(k\hat{x} - \omega_\mathrm{l} t). \tag{2.10}$$

ω_l is the frequency and k the wave number of the laser field. Ω is called Rabi frequency and is a measure of the interaction strength between the ion and the laser field. It is derived from a semiclassical treatment of the interaction [31, chapter 7].

The complete Hamiltonian is then given by

$$H = H_\mathrm{a} + H_\mathrm{t} + H_\mathrm{l}. \tag{2.11}$$

In order to analyse the system further the Hamiltonian is transformed into the interaction picture given by $H_0 = H_\mathrm{a} + H_\mathrm{t}$. In this case the operator H_L results from the transformation of H_l to the interaction picture and is given by

$$H_\mathrm{L} = e^{iH_0 t} H_\mathrm{l} e^{-iH_0 t}. \tag{2.12}$$

As the ion is in a harmonic potential, the position operator $\hat{x}$ can be expressed by the creation and annihilation operators

$$k\hat{x} = \eta(a + a^\dagger). \tag{2.13}$$

This leads to the definition of the Lamb-Dicke parameter

$$\eta = k\sqrt{\frac{\hbar}{2m\omega}}. \tag{2.14}$$

η is a measure of the relation between the width of the wave packet describing the ion in the ground state $\sqrt{\hbar/(2m\omega)}$ and the wavelength of the laser $\lambda = 2\pi/k$. Equation (2.12) can be simplified in several steps. First the fastest oscillating terms are neglected. This step is called rotating wave approximation. Afterwards a further simplification can be done by assuming that the wavelength of the laser is much bigger than the width of the wave packet describing the ion motion. This is called the Lamb-Dicke approximation [30]: $\eta^2(2\bar{n} + 1) \ll 1$, where $\bar{n}$ is the mean phonon number.

Depending on the laser detuning $\Delta = \omega_\mathrm{l} - \omega_\mathrm{a}$ further simplifications can be done. The important cases are $\Delta = 0$ and $\Delta = \pm\omega$, where an additional rotating wave approximation is possible. The calculations are carried out in [30, chapter 3]. The results are presented in the next section.

2.2.2 Special cases of the Hamiltonian in the interaction picture

An overview of the energy level scheme and the three different transitions for $\Delta = 0$ and $\Delta = \pm\omega$ is given in figure 2.3. The three transitions discussed in the following differ by their coupling strength and their effect on the motional state of the ion.

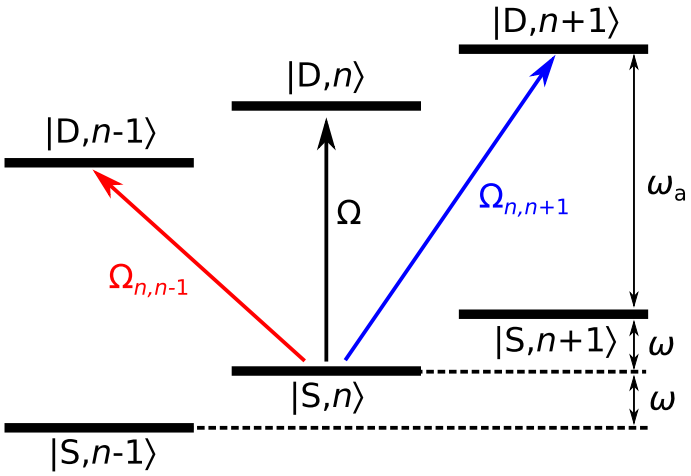

Figure 2.3: Energy level scheme of a two level atomic system with energy difference ω_a in a harmonic trapping potential with trapping frequency ω. The transitions are driven by laser light. The red sideband transition decreases the phonon number n, the carrier transition in the middle does not affect n and the blue sideband transition increases n. The transitions are labelled with their respective coupling strengths.

Carrier transition: For $\Delta = 0$ the above described approximations for (2.12) lead to

$$H_{\mathrm{C}} = \hbar\frac{\Omega}{2}(\sigma_+ + \sigma_-). \tag{2.15}$$

The time evolution of the ion's electronic ground state $|S\rangle$ is given by

$$|S\rangle \rightarrow \cos\left(\frac{\Omega t}{2}\right)|S\rangle - i\sin\left(\frac{\Omega t}{2}\right)|D\rangle\,. \tag{2.16}$$

Consequently, the resonant laser light produces an oscillation of the population between $|S\rangle$ and $|D\rangle$. It only affects the electronic state of the ion and not the motional state.

Red sideband transition: For $\Delta = -\omega$ the Hamiltonian is given by

$$H_{\mathrm{RSB}} = i\hbar\eta\frac{\Omega}{2}(\sigma_+ a - \sigma_- a^\dagger). \tag{2.17}$$

In this case the only transitions that are driven change the motional state and the electronic state. These transitions are crucial for the heating rate measurements described in section 3.3 and therefore the time evolution resulting from H_{RSB} is analysed in more detail.

The coupling strength $\Omega_{n,n-1}$ between $|S,n\rangle$ and $|D,n-1\rangle$ depends on the motional state n and is given by

$$\Omega_{n,n-1} = \eta\Omega\sqrt{n}. \tag{2.18}$$

Shining the laser light onto an ion in the state $|S\rangle\,|n\rangle$ leads to the following time evolution:

$$|S\rangle\,|n\rangle \rightarrow \cos\left(\frac{\Omega_{n,n-1}t}{2}\right)|S\rangle\,|n\rangle + \sin\left(\frac{\Omega_{n,n-1}t}{2}\right)|D\rangle\,|n-1\rangle\,. \tag{2.19}$$

As shown in figure 2.3, this time evolution enables one to reduce the motional state by one when the ion is transferred to its excited electronic state. The probability of measuring the ion in the excited state $|D\rangle$ is

$$p_D(t,n) = \sin^2\left(\frac{\Omega_{n,n-1}t}{2}\right). \tag{2.20}$$

Blue sideband transitions: In this case $\Delta = \omega$ and the Hamiltonian is

$$H_{\mathrm{BSB}} = i\hbar\eta\frac{\Omega}{2}(\sigma_+ a^\dagger - \sigma_- a). \tag{2.21}$$

Similarly to the red sideband transitions the coupling strength $\Omega_{n,n+1}$ depends on n and is given by

$$\Omega_{n,n+1} = \eta\Omega\sqrt{n+1} = \Omega_{n+1,n}. \tag{2.22}$$

Analogously to (2.19) the time evolution is described by

$$|S\rangle|n\rangle \rightarrow \cos\left(\frac{\Omega_{n,n+1}t}{2}\right)|S\rangle|n\rangle + \sin\left(\frac{\Omega_{n,n+1}t}{2}\right)|D\rangle|n+1\rangle. \tag{2.23}$$

As shown in figure 2.3, this time evolution enables one to increase the motional state by one when the ion is transferred to its excited electronic state. The probability of measuring the ion in $|D\rangle$ is

$$p_D(t,n) = \sin^2\left(\frac{\Omega_{n,n+1}t}{2}\right). \tag{2.24}$$

2.3 Ca^+ level scheme

In the experiments in this thesis $^{40}Ca^+$ was used as the trapped ion. This section is based on the description in [29] and sums up the important information about the electronic energy level scheme shown in figure 2.4.

$4^2S_{1/2}$ is the ground state of the ion. It has a $397\,\mathrm{nm}$ dipole transition to the $4^2P_{1/2}$, which is used for Doppler cooling (see section 2.4.2) and state detection (see section 2.4.4). As the $4^2P_{1/2}$ state has a $7.5\,\%$ probability to decay to the $3^2D_{3/2}$ state, a $866\,\mathrm{nm}$ laser is used for repumping the electron to $4^2P_{1/2}$.

The $729\,\mathrm{nm}$ transition from the ground state to the $3^2D_{5/2}$ state is a quadrupole transition and therefore the upper state is metastable with a lifetime $\tau = 1.17\,\mathrm{s}$. The effective lifetime of the $3^2D_{5/2}$ state can be reduced by coupling it to the $4^2P_{3/2}$ state with a $854\,\mathrm{nm}$ laser. Due to the Zeeman splitting the $729\,\mathrm{nm}$ transition splits up into the 10 different transitions shown in figure 2.5. The $m_J = -1/2$ to $-1/2$ transition is used for the heating rate measurements (section 3.3). Additionally, the two levels can serve as the qubit for quantum information processing. The $m_J = -1/2$ to $-5/2$ transition is used for sideband cooling as described in section 2.4.3.

The ion can be initialised in the $m_J = -1/2$ state by driving the $m_J = 1/2$ to $-3/2$ transition. Thereby any population in the $m_J = 1/2$ state is first transferred to the excited state with $m_J = -3/2$. $854\,\mathrm{nm}$ laser light drives the dipole transition to the $4^2P_{3/2}$ state.

From there it decays into the ground state with either $m_J = 1/2$ or $m_J = -1/2$. This cycle is repeated several times. As soon as the ion decays into the $m_J = -1/2$ state, it stays there, because the $729\,\mathrm{nm}$ laser is not resonant with any transition. This technique is called optical pumping.

Since only the described states are relevant for the experimental techniques and they can be distinguished without the principal quantum number and the multiplicity, these two numbers are omitted in the following. For example, $4^2P_{3/2}$ is written as $P_{3/2}$.

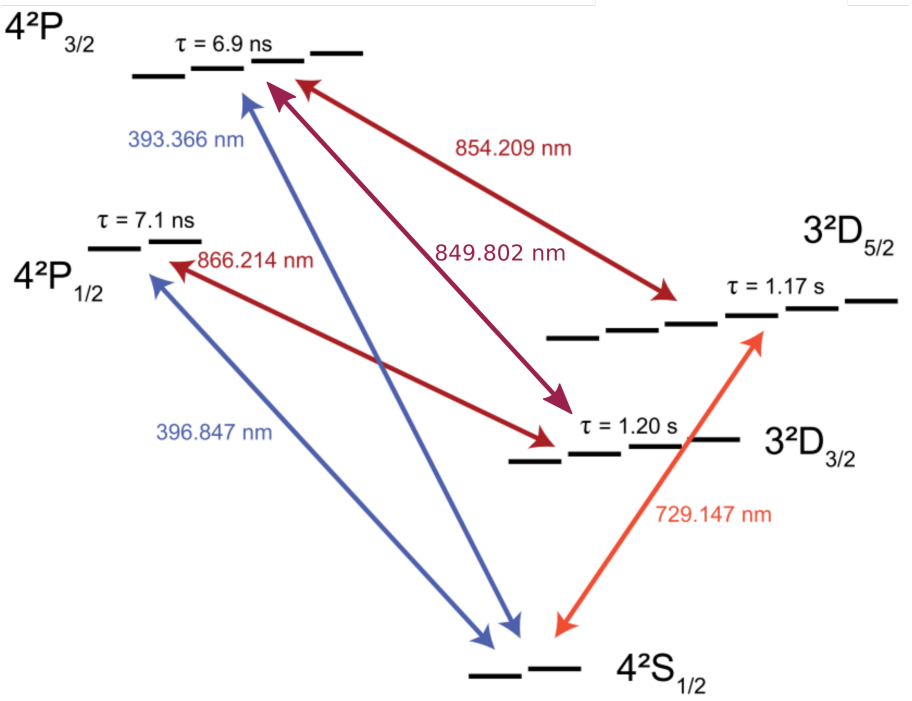

Figure 2.4: Relevant energy levels of $^{40}Ca^+$ together with the Zeeman sublevels. Additionally the lifetime τ and the wavelength of the transitions in nm are given. The $397\,\mathrm{nm}$ dipole transition is used for Doppler cooling and state detection. The $866\,\mathrm{nm}$ dipole transition serves as a repumper from the $3^2D_{3/2}$ state. The $729\,\mathrm{nm}$ quadrupole transition can be used as a qubit transition and together with the $854\,\mathrm{nm}$ dipole transition it serves for sideband cooling and optical pumping. The original figure from [29] was modified and uses the information from [32–34]. Figure courtesy of Michael Niedermayr.

2.4 Experimental techniques

The experimental techniques described in this section are used for realizing the trap experiments of this thesis. They are well established techniques in ion trapping experiments [30] and are presented here only briefly.

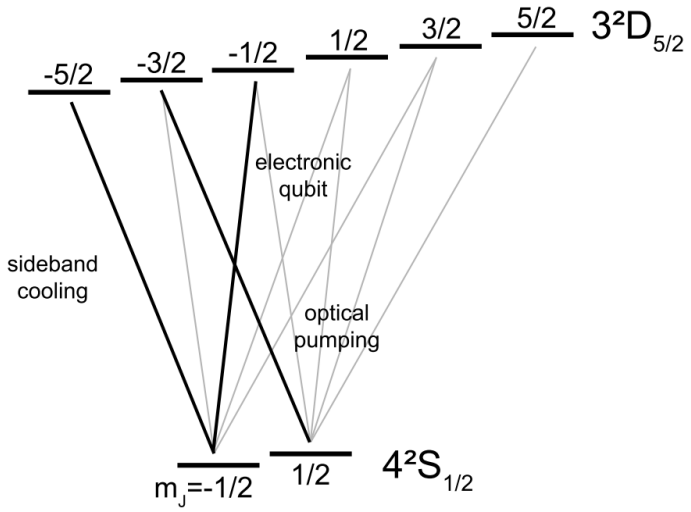

Figure 2.5: Zeeman splitting of the $3^2\mathrm{D}_{5/2}$ and the $4^2\mathrm{S}_{1/2}$ state in an external magnetic field. The highlighted transitions are used in the following way: Spectroscopy is done on the $m_\mathrm{J} = -1/2$ to $-1/2$ transition. These two levels can be used as the qubit. Sideband cooling is performed on the $m_\mathrm{J} = -1/2$ to $-5/2$ transition. The $m_\mathrm{J} = 1/2$ to $-3/2$ transition is used for optical pumping. Figure courtesy of Michael Niedermayr [29].

2.4.1 Photoionisation of neutral Ca-atoms

In order to trap $^{40}\mathrm{Ca}^+$ ions, neutral ^{40}Ca-atoms have to be ionised at the trapping location of the ion trap. In the ground state electron configuration the ^{40}Ca-atom has two electrons in the outermost shell. The ionisation process is performed in two steps. First a $422\,\mathrm{nm}$ laser excites one of the electrons from the ground state $4^1\mathrm{S}_0$ to the $4^1\mathrm{P}_1$ state and then an additional laser at $377\,\mathrm{nm}$ wavelength excites the electron into the continuum [35]. A beam of neutral Ca-atoms from an oven is crossed with the two overlapped laser beams to perform this ionisation process at the trapping location.

2.4.2 Doppler cooling

In the weak binding regime $\Gamma \gg \omega$, where $\Gamma = 2\pi/\tau$ is the natural linewidth of the cooling transition, the fundamentals of Doppler cooling can be described using a semiclassical picture [28]: The ion is treated as two-level atomic system with an energy difference $\hbar\omega_\mathrm{a}$ that undergoes classical motion. Laser light with frequency ω_l shone onto the ion induces an excitation of the electronic state of the ion and increases its momentum by $\hbar k_\mathrm{l} = \hbar\omega_\mathrm{l}/c$ in the direction of the laser (c is the speed of light). After a spontaneous decay the ion loses the momentum $\hbar k_\mathrm{a} = \hbar\omega_\mathrm{a}/c$ in a random direction. If the laser is red-detuned ($\Delta = \omega_\mathrm{l} - \omega_\mathrm{a} < 0$), the ion absorbs predominantly photons that travel in the opposite direction of the ion. Therefore on average the absorption and emission process reduces the momentum of the ion. This reduces the ion's motional energy described by its mean phonon number. On the other hand, the finite momentum transfer in the spontaneous decay produces a random walk of the ion in momentum space. Overall this leads to a

minimal residual phonon number

$$n_{\min} \approx \frac{\Gamma}{2\omega}, \tag{2.25}$$

given by the Doppler limit [36]

$$E_{\mathrm{D}} = \frac{\hbar\Gamma}{2}, \tag{2.26}$$

with the minimum energy E_{D} achieved for $\Delta = -\Gamma/2$.

In $^{40}Ca^{+}$ the $397\,\mathrm{nm}$ transition is used for Doppler cooling. The natural linewidth Γ of this transition is $\Gamma = 2\pi \cdot 22.4\,\mathrm{MHz}$ (see figure 2.4). For a trapping frequency $\omega = 2\pi \cdot 1\,\mathrm{MHz}$, the Doppler limit is $n_{\min} \approx 11$. For the heating rate measurements, the mean phonon number $\bar{n}$ needs to be close to the ground state $\bar{n} < 1$. Consequently, an additional cooling method has to be applied.

2.4.3 Sideband cooling

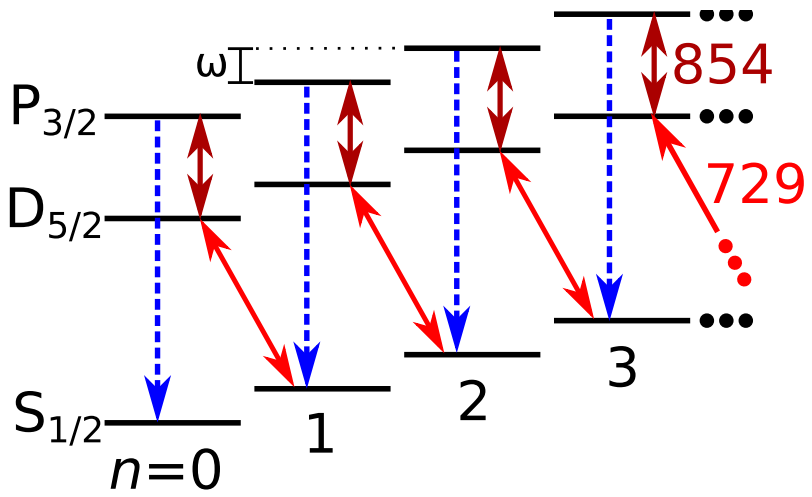

Figure 2.6: Sideband cooling cycle for $^{40}Ca^{+}$ ions. The red transition lines indicate applied laser light with $854\,\mathrm{nm}$ and $729\,\mathrm{nm}$ transferring the electron to the $P_{3/2}$ state. The blue dotted line shows the spontaneous decay back into the ground state $S_{1/2}$. Due to the detuning $\Delta = -\omega$ of the $729\,\mathrm{nm}$ laser the phonon number n is reduced by one quantum in each cycle.

For sideband cooling it is necessary that the linewidth Γ of the used transition is smaller than the trap frequency ω. If this condition holds the system is in the so-called resolved sideband regime. The $729\,\mathrm{nm}$ transition in $^{40}Ca^{+}$ fulfils this criterion for the $D_{5/2}$ state with $\Gamma \approx 0.9\,\mathrm{Hz}$ (see figure 2.4).

In this case a reduction of the motional energy can be achieved by applying the $729\,\mathrm{nm}$ laser resonant with the red sideband ($\Delta = -\omega$). This drives mainly transitions that excite the ion and reduce the motional state. The ion can then decay spontaneously back to the ground state. Therefore the phonon number is reduced by one quantum in each excitation cycle.

As the $D_{5/2}$ state has a lifetime of $\tau = 1.17\,\mathrm{s}$, the decay rate back to the ground state can be enhanced significantly by applying the $854\,\mathrm{nm}$ laser to couple the $D_{5/2}$ state to

the fast decaying $P_{3/2}$ state. The combined cycle is illustrated in figure 2.6 and greatly enhances the sideband cooling efficiency. It was shown that in this way it is possible to reach a ground state occupation of up to 99.9 % [37]. The smallest mean phonon number that can be achieved is limited by the cooling efficiency and the heating mechanisms in the trap (see chapter 3). Reaching the motional ground state is essential for the heating rate measurement technique described in section 3.3. A more detailed description can be found in [30].

2.4.4 State detection by electron shelving

For performing the heating rate measurements it is required to read out the electronic state of the ion. That means a measurement has to project the ion into the ground state $S_{1/2}$ or the excited state $D_{5/2}$. Shining the $397\,\mathrm{nm}$ laser on the ion drives the transition to the $P_{1/2}$ state, if the ion is in $S_{1/2}$. The fluorescence of this dipole transition is collected by a CCD-camera or a photomultiplier tube (PMT). This fluorescence signal is absent if the ion is initially in the $D_{5/2}$ state.

Consequently, measuring fluorescence light from the ion is equivalent to detecting the ion state to be $S_{1/2}$. It should be noted that additionally $866\,\mathrm{nm}$ laser light has to be used to repump the ion from the $D_{3/2}$ state. This technique is called electron shelving and makes it possible to achieve detection efficiencies of nearly $100\,\%$ [38].

2.4.5 Micromotion compensation

As described in section 2.1.1, micromotion is an oscillation of the ion at the RF-frequency Ω_{RF} caused by a displacement of the ion away from the RF-minimum. This motion is undesirable, because it affects the lineshape due to a Doppler effect on the ion's transition frequencies. This negatively affects some of the above described essential experimental methods:

On the $S_{1/2}$-$P_{1/2}$ transition the Doppler effect is observed in a Doppler broadening of the transition linewidth and therefore it reduces the Doppler cooling efficiency.

For transitions in the resolved sideband regime, micromotion decreases the coupling strength of resonant laser light due to micromotion sidebands [39]. Accordingly, the sideband cooling efficiency is decreased.

It is therefore very important to minimise the micromotion. In order to move the ion into the RF-minimum additional DC-electrodes are commonly integrated in the trap design. Several methods exist for using these electrodes to compensate the micromotion. Detailed information about them can be found in [30, 39]. In the following, a brief description of the methods applied during this thesis is provided.

Varying the RF-confinement: The detected fluorescence light of the ion makes it possible to observe its position on a CCD-camera. If the ion is displaced from the RF-minimum by stray fields, a reduction of the RF-voltage moves the ion further away from the RF-minimum. This position change is visible on the CCD-camera and the micromotion is reduced in the following iterative scheme:

The ion position at the normal RF-voltage is marked on the camera image. After lowering the RF-voltage the ion displacement is compensated by applying corresponding changes on the DC-voltages. The procedure is repeated until the ion does not move when the RF-voltage is decreased.

This method is usually applied at the beginning of the trap operation, because it allows one to roughly reduce the micromotion in a fast way. However, it has a significant drawback in the current trap setup: movements of the ion perpendicular to the trap surface cannot be seen on the CCD-camera. Accordingly, additional methods have to be applied.

Doppler broadening of the $S_{1/2}$-$P_{1/2}$ transition: The linewidth of the transition can be obtained by scanning the $397\,\mathrm{nm}$ laser over the resonance frequency and simultaneously measuring the fluorescence light of the ion. Repeating this measurement for different voltages on the compensation electrodes enables one to reduce the Doppler broadening of the $S_{1/2}$-$P_{1/2}$ transition and hence decreases the micromotion. The Doppler broadening is only observed if the movement of the ion has a component parallel to the laser beam. Therefore only the micromotion along the laser beam can be detected. We used this method for a rough compensation of the micromotion and it was always followed by an additional method using resolved sideband measurements.

Resolved sideband measurements: The small linewidth of the $S_{1/2}$-$D_{5/2}$ transition allows one to resolve micromotion sidebands at $\Delta = \pm\Omega_{\mathrm{RF}}$. The Rabi frequency Ω_{ms} on the micromotion sideband depends on the micromotion amplitude of the ion along the laser beam direction. Thus a reduction of this micromotion by changes in the compensation voltages is observable in a reduction of Ω_{ms}. When the compensation voltages are changed, one has to ensure that the reduction of Ω_{ms} does not result from moving the ion out of the focus of the laser beam. This can be achieved by additionally measuring the Rabi frequency on the carrier ($\Delta = 0$) and keeping it at a comparable level by following the movement of the ion with the laser focus.

2.4.6 Sideband spectroscopy on the $S_{1/2}$-$D_{5/2}$ transition

In order to perform sideband cooling and optical pumping, it is necessary to identify the different transitions in the $S_{1/2}$-$D_{5/2}$ spectrum. Additionally, the sidebands have to be determined to calculate the trapping frequencies. To find these transitions the following pulse sequence was used for spectroscopy during this thesis:

1. **Doppler cooling:** The $397\,\mathrm{nm}$ laser together with the $866\,\mathrm{nm}$ repumper is used to cool the ion. At the end of this cooling step, the ion decays back to the ground state $S_{1/2}$.

2. **Driving the $S_{1/2}$-$D_{5/2}$ transition:** A pulse of $729\,\mathrm{nm}$ laser-light at a fixed frequency is applied to the ion to transfer part of the population from the $S_{1/2}$ state to the metastable $D_{5/2}$ state.

3. **State detection:** The electron shelving technique is used to determine the electronic state of the ion.

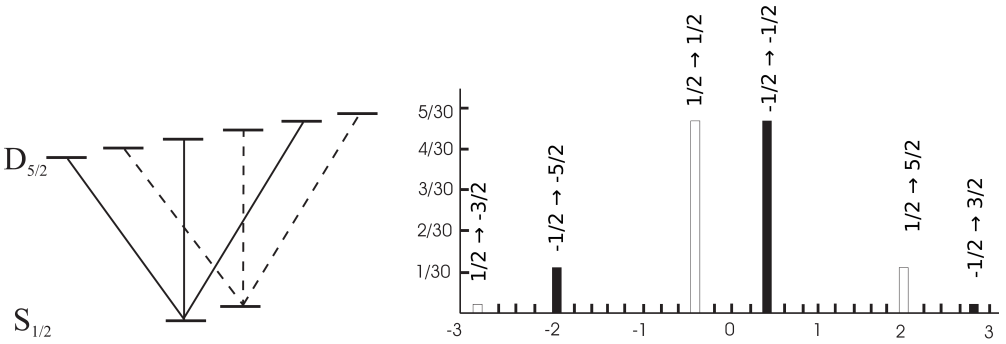

Figure 2.7: Allowed transitions of the $S_{1/2}$-$D_{5/2}$ transition in the following specific experimental setup: The angle between the $729\,\mathrm{nm}$ laser beam and the magnetic field is $45\,^\circ$ and the angle between the polarization of the laser and the magnetic field vector projected into the plane of incidence is $0\,^\circ$. The height of the peaks corresponds to their squared Clebsch-Gordan factors [30]. Figure courtesy of Christian Roos.

The pulse sequence is repeated typically 50 times to determine the $D_{5/2}$ state population.

By scanning the frequency of the $729\,\mathrm{nm}$ laser the different transitions between the Zeeman sublevels of the $S_{1/2}$ state and the $D_{5/2}$ state can be found. In general the $S_{1/2}$-$D_{5/2}$ transition splits into 10 components in a non-zero magnetic field, the so-called carrier transitions.

In our experiment the angle between the $729\,\mathrm{nm}$ laser beam and the magnetic field is $45\,^\circ$ and the angle between the polarization of the laser and the magnetic field vector projected into the plane of incidence is $0\,^\circ$. This configuration leads to a reduction of the allowed transitions to the 6 transitions shown in figure 2.7 [30].

If the spectroscopy is performed in the resolved sideband regime, the red- and blue-sideband transitions can be observed. These are shifted from the carrier transitions by the trapping frequencies. The reduced coupling strengths of the sideband transitions (see section 2.2.2) lead to a narrower peak in the observed spectrum. It should be noted that the only sidebands that can be observed are those where the trap mode of the corresponding frequencies has a component along the laser beam direction. An example of a sideband spectrum is shown in figure 6.8.

Chapter 3

Motional heating in ion traps

With the methods presented in the previous chapter it is possible to trap and cool ions, manipulate their electronic state and read out this state. The ion's electronic ground state and a metastable excited state can be used as a qubit for quantum computations and simulations. The ion's motional state does not have to be manipulated to perform single qubit gates and high fidelities exceeding 0.99 can be reached [7]. However, computations require also two qubit gates using the common motional state of the ion string [8, 9]. Therefore two qubit gates are affected by motional heating. Electric field noise heats the common motional mode. The energy of this mode is quantified by its thermal average phonon number $\bar{n}$ and the motional heating is given by the heating rate Γ_{h}. The heating leads to decoherence of the motional state and therefore limits the fidelity of the two qubit gates. The relation between the spectral electric field noise density S_{E} and Γ_{h} for a single ion with trap frequency ω, mass m and charge e is given by [17]

$$\Gamma_{\mathrm{h}} = \frac{e^2}{4m\hbar\omega} S_{\mathrm{E}}(\omega). \tag{3.1}$$

There are different known sources for S_{E}. The most relevant one in this thesis is Johnson noise described in detail in section 3.1.

In an ion trap setup, it is often difficult to identify the main source of RF electric field noise to which the ion is subjected. Additionally, in several ion traps the heating rate was measured to be higher than its prediction by all known sources. In these cases the phenomenon of motional heating is often called "anomalous" heating [18, 17].

In this project it is planned to characterise Γ_{h} by measuring the frequency scaling of Γ_{h} by varying the trap frequency. Another characteristic is the spatial dependence of Γ_{h} which can be obtained by measuring Γ_{h} for several positions of the ion in the trap. These characteristics provide information about the dominant source of noise in an ion trap. A few examples of recent experimental measurements are presented in section 3.2.

In this thesis Γ_{h} is measured by resolved sideband spectroscopy. This technique is explained in section 3.3.

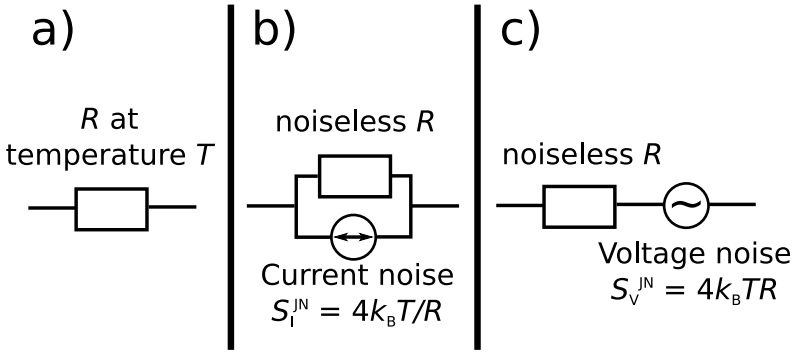

Figure 3.1: Three equivalent electronic circuits modelling Johnon noise. **a)** A resistor R at temperature T. **b)** A noiseless resistor with a current noise source in parallel with power spectral density $S_{\mathrm{I}}^{\mathrm{JN}}$. **c)** A noiseless resistor with a voltage noise source in series with power spectral density $S_{\mathrm{V}}^{\mathrm{JN}}$.

3.1 Johnson noise and technical noise

The theoretical description in this section is based on [17, 11]. Johnson noise (or Johnson-Nyquist noise or thermal noise) is a source of electrical noise generated by thermal motion of charge carriers in a resistor. The power spectral density of this voltage noise at the frequency ω is given by

$$S_{\mathrm{V}}^{\mathrm{JN}} = 4k_{\mathrm{B}}TR(\omega, T), \tag{3.2}$$

with the Boltzmann constant k_{B} and the resistance $R(\omega, T)$ depending on the temperature T. In an electronic circuit it can be modelled as a current noise source connected in parallel or as a voltage noise source connected in series to the resistor, as shown in figure 3.1. If this voltage noise is present on a trap electrode it creates the electric field noise density

$$S_{\mathrm{E}}^{(\mathrm{JN})} = \frac{S_{\mathrm{V}}^{\mathrm{JN}}}{D^2} = \frac{4k_{\mathrm{B}}TR(\omega, T)}{D^2}, \tag{3.3}$$

where D is the characteristic distance between the ion and the electrode defined later in this section. The resistance of the trap electrode is not the only source of Johnson noise that has to be considered. In order to calculate $S_{\mathrm{E}}^{(\mathrm{JN})}$, the effective real resistance $R_{\mathrm{eff}}(\omega, T)$ between the trap electrode and electrical ground has to be used in equation 3.3. This includes losses in dielectrics of the capacitors integrated on the filterboard and the real resistance of inductors. To analyse the expected Johnson noise $S_{\mathrm{E}}^{(\mathrm{JN})}$ the circuit of each trap electrode has to be considered individually.

Additionally, one has to calculate the characteristic distance D for each electrode. Therefore the i-th component of the electric field $E_{i,j}$ at the ion's position resulting from the voltage V_j applied to the j-th electrode has to be calculated. This can be done by first computing the electrical potential Φ everywhere in space using the Laplace equation $\triangle\Phi = 0$ and the voltages on the electrodes as boundary conditions. The electric field is then given by $E = -\nabla\Phi$, from which D can be calculated using

$$D_{i,j} = \frac{V_j}{E_{i,j}}. \tag{3.4}$$

To calculate the corresponding heating rate Γ_{h} in each trap mode $\tilde{i}$ at frequency $\omega_{\tilde{i}}$, the electric field components E_i have to be transformed to the Cartesian coordinate system given by the trap modes.

Two other voltage noise sources S_{V} can be linked to the electric field noise density by the characteristic distance of the electrode in the same way as Johnson noise. First, noisy voltage sources caused by the imperfect nature of the power supplies in laboratory equipment or produced by digital-to-analog cards can result in voltage fluctuations on the trap electrodes if they are not properly filtered. These sources are referred to as technical noise. Second, fluctuating electromagnetic fields in the laboratory can be picked up by wires from the power supplies to the trap electrodes due to their inductance. This creates the so-called electromagnetic pickup noise.

In [17] it is stated that in some literature technical noise and electromagnetic pickup is lumped together with the above considered Johnson noise. It is emphasized that for the calculations in this thesis only noise produced directly by the electronic circuit leading to the trap electrodes is considered as Johnson noise.

Frequency scaling:

In general, resistors are considered to produce white noise, i.e. noise that does not depend on the frequency. This is valid for many resistors over a wide range of frequencies and implies that Johnson noise should not depend on the trap frequency. However, the fact that the effective real resistance $R_{\mathrm{eff}}(\omega, T)$ has to be taken into account can lead to a totally different frequency behaviour. Therefore the electronic circuit has to be modelled in details to predict the observable frequency dependence. An example is given in equation (4.7) in section 4.6.1 where the effect of a bypass capacitor on $R_{\mathrm{eff}}(\omega, T)$ is calculated.

Spatial dependence:

As the Johnson noise seen by the ion depends on the characteristic distance of the ion to the trap electrodes, its dependence on the ion position (the spatial dependence[1]) has to be calculated with equation 3.4. Consequently, no general remarks can be made on the spatial dependence and it has to be analysed individually for each trap design. Concerning our trap design presented in section 4.5 the following information can be given. If it is assumed that the voltage fluctuations on each electrode caused by Johnson noise have a similar magnitude, then the noise does not vary significantly while the ion is scanned along the trap axes. However, if the noise from one electrode exceeds the noise from the other electrodes by far, then the motional heating of the ion can change by more than an order of magnitude along the trap axes (see e.g. figure 4.12).

[1] In the literature, the name spatial dependence is also often used for the scaling of Γ_{h} with the distance d of the ion from the surface. In this case Johnson noise, electromagnetic pickup and technical noise scales as $1/d^2$ [17].

3.2 Anomalous heating

As the causes of motional heating are not fully understood yet, the phenomenon is often called anomalous heating. In this section several examples of heating rate measurements in ion traps are presented to show that anomalous heating has to be further investigated to better understand the phenomenon. Further information about this issue is published in [17].

3.2.1 Frequency scaling

In many ion traps, the frequency dependence of the electric field noise is considered to locally (within the range of the trapping frequencies) follow a power-law leading to the ansatz

$$S_{\mathrm{E}} \propto \nu^{-\alpha}. \tag{3.5}$$

Three examples of measured frequency scaling in an ion trap are given in the following:

Daniilidis et al. [19] measured heating rates in a surface trap with $^{40}Ca^{+}$ ions $100\,\mu\mathrm{m}$ above the surface before and after Ar^{+} ion beam bombardment. The noise level was reduced by two orders of magnitude after the treatment implying that surface contaminations have a significant effect on Γ_{h}. Before the treatment the frequency scaling was determined to be $\alpha = 1.27 \pm 0.23$ in the frequency range from $200\,\mathrm{kHz}$ to $1\,\mathrm{MHz}$. After the treatment $\alpha = 0.95 \pm 0.28$ is obtained in the frequency range from $200\,\mathrm{kHz}$ to $580\,\mathrm{kHz}$ with noise levels between $2.05(7) \times 10^{-13}\,\mathrm{V^2/(m^2Hz)}$ and $2.61(3) \times 10^{-14}\,\mathrm{V^2/(m^2Hz)}$. Since they are able to give a lower bound on Johnson noise, which is close to the reported noise level, they expect to be limited by Johnson and technical noise. In the same setup an increased heating rate around 800 kHz is observed and attributed by the authors to a resonance on the filter board. This exemplifies the importance of analysing the electronic circuit connected to the trap to interpret the frequency scaling.

Hite et al. [40] investigated a surface trap with ion-electrode distance of $40\,\mu\mathrm{m}$ with $^{9}Be^{+}$ ions. They also measured the heating rate before and after Ar^{+} ion beam bombardment. The treatment reduced the noise level by 2 orders of magnitude down to values from $10^{-14}\,\mathrm{V^2/(m^2Hz)}$ to $10^{-12}\,\mathrm{V^2/(m^2Hz)}$ in the frequency range of $1.7\,\mathrm{MHz}$ to $4.7\,\mathrm{MHz}$. It is expected that the reduction of Γ_{h} after the treatment is due to reduced surface contaminations. Before and after cleaning α was 2.53(7) and 2.57(4). They claimed that this scaling is consistent with surface-diffusion-noise models and certain parameter ranges of other models.

Turchette et al. [41] reported on measurements with $^{9}Be^{+}$ ions in several traps. Among them were two circular ring traps with an ion-electrode distance of $123\,\mu\mathrm{m}$ and $277\,\mu\mathrm{m}$. When the trap frequency was varied from $1.2\,\mathrm{MHz}$ to $8\,\mathrm{MHz}$, S_{E} was measured to be between $10^{-15}\,\mathrm{V^2/(m^2Hz)}$ and $10^{-13}\,\mathrm{V^2/(m^2Hz)}$ in the large trap and in the small trap it was between $10^{-13}\,\mathrm{V^2/(m^2Hz)}$ and $10^{-10}\,\mathrm{V^2/(m^2Hz)}$. From the data plots in [41], the frequency scaling was extracted by Brownnutt et al. [17]. The scaling was determined to be $\alpha = 6.0(2)$ and $4.0(8)$ differing significantly from the above reported values. The origin of the noise in these traps remains unclear.

These examples show that different values are reported for α. As concluded in [17], these results reported in the literature show that the heating rates in many ion traps can

not be linked to one specific origin.

3.2.2 Spatial dependence

To our knowledge the spatial dependence of motional heating in an ion trap was examined and reported only in the following two experiments:

Daniilidis et al. [42] measured the motional heating of $^{40}Ca^{+}$ ions in a linear ion surface trap with an ion-electrode separation of $240\,\mu m$. In these measurements the axial position of the ion was scanned by approximately $1.5\,mm$, measuring Γ_h in steps of $0.2\,mm$. After several months of trap operations, Γ_h increased in the loading zone of the trap. There Γ_h was 20 times higher than in the beginning of the trap operation and 20 times higher than in a region $0.8\,mm$ away from the loading zone. They concluded that this increase is due to surface contaminations at the loading zone produced in the following ways: First, the trap electrodes can be bombarded by electrons created during photoionization of Ca-atoms outside of the trapping volume. Furthermore, $^{40}Ca^{+}$ ions that hit the electrodes with energies of a few eV can form chemical compounds on the surface. $^{40}Ca^{+}$ ions with higher energies can sputter material from the surface of the electrodes.

Allcock et al. [43] reported on cleaning the trap surface with ns pulses from a tripled Nd:YAG laser at $355\,nm$. They measured the motional heating with $^{40}Ca^{+}$ ions trapped about $98\,\mu m$ away from the closest electrode. The heating rate measurements were performed at two positions along the trap axis separated by $320\,\mu m$. One of the two trapping sites on the surface was cleaned with ns pulses from the tripled Nd:YAG laser. Above the cleaned surface Γ_h was reduced by $\approx 50\,\%$ compared to the untreated area. The reduction of surface contaminations could be a possible explanation.

In summary, both experiments were able to further characterise the origin of Γ_h in their trap by measuring its spatial dependence. In these traps surface contaminations seemed to have a significant effect on Γ_h. In general other noise sources can have a characteristic spatial dependence as well. For example Γ_h from technical noise or Johnson noise on a trap electrode depends on the characteristic distance (see equation (3.3)). This can lead to a difference of more than an order of magnitude in the induced Γ_h at different ion positions. Examples of such a spatial dependence are shown in figure 4.8 and figure 4.12 in the next chapter.

In conclusion, measuring the spatial dependence of Γ_h in ion traps can be a promising method to determine the origin of anomalous heating.

3.3 Measuring heating rates via resolved sideband spectroscopy

The heating rate in an ion trap can be measured with different techniques [17]. In the experiments described in this thesis a resolved sideband spectroscopy method was used and accordingly it is explained in detail in this section (based on [17, 41]). In this thesis, we refer to this method as ratio method.

The ratio method enables the measurement of the heating rate for all three trap frequencies separately. In the following theoretical treatment, the method is described for a given trap frequency ν.

It is assumed that the ion's motional state has a thermal distribution with an average phonon number $\bar{n}$. The probability P_n of the nth level being occupied is given by

$$P_n = \frac{\bar{n}^n}{(1+\bar{n})^{n+1}}. \tag{3.6}$$

The ratio method enables the measurement of $\bar{n}$, if $\bar{n} \lesssim 10$. Consequently, Doppler and sideband cooling have to be applied to cool the ion close to its motional ground state. After that $729\,\mathrm{nm}$ laser light with $\Delta = -\nu$ (resonant with the red sideband) is applied for a time t. Following equation (2.20), the probability of the ion to be in the excited state $|D\rangle$ is

$$P_{D,\mathrm{RSB}}(t) = \sum_{n=1}^{\infty} P_n \sin^2\left(\frac{\Omega_{n,n-1}t}{2}\right). \tag{3.7}$$

Similarly, applying laser light resonant to the blue sideband for the same time t after ground state cooling results in

$$\begin{aligned} P_{D,\mathrm{BSB}}(t) &= \sum_{n=0}^{\infty} P_n \sin^2\left(\frac{\Omega_{n,n+1}t}{2}\right) && (3.8)\\ &= \sum_{n=0}^{\infty} \frac{\bar{n}^n}{(1+\bar{n})^{n+1}} \sin^2\left(\frac{\Omega_{n+1,n}t}{2}\right) && (3.9)\\ &= \frac{1+\bar{n}}{\bar{n}} \sum_{m=1}^{\infty} \frac{\bar{n}^m}{(1+\bar{n})^{m+1}} \sin^2\left(\frac{\Omega_{m,m-1}t}{2}\right) && (3.10)\\ &= \frac{1+\bar{n}}{\bar{n}} P_{D,\mathrm{RSB}}(t). && (3.11) \end{aligned}$$

From these two probabilities, the mean phonon number can be calculated as

$$\bar{n} = \frac{P_{D,\mathrm{RSB}}(t)}{P_{D,\mathrm{BSB}}(t) - P_{D,\mathrm{RSB}}(t)}. \tag{3.12}$$

To choose an optimal pulse length t_{opt} the following two points should be considered:

First, if the decoherence time $\tau < t$, the time evolution does not result in the expected sinusodial Rabi oscillations as predicted by equation (2.23). Instead the oscillations converge to a steady state [44]. As equation (3.12) is based on a coherent time evolution, $t < \tau$ must hold to be able to use it.

Second, in the denominator of equation (3.12) the difference between the excitation on the blue sideband and the one on the red sideband is taken. This produces large errors for $P_{D,\mathrm{BSB}}(t) \approx P_{D,\mathrm{RSB}}(t)$. Therefore t should be chosen in a way to maximize $P_{D,\mathrm{BSB}}(t) - P_{D,\mathrm{RSB}}(t)$. Assuming a ground state cooled ion with $\bar{n} \ll 1$, $P_{D,\mathrm{RSB}}(t) \approx 0$ and therefore $P_{D,\mathrm{BSB}}(t) - P_{D,\mathrm{RSB}}(t) \approx P_{D,\mathrm{BSB}}(t)$. Consequently, the optimal time t_{opt} should be chosen at the first maximum of $P_{D,\mathrm{BSB}}(t)$. This conclusion is still valid for small phonon numbers $\bar{n} \lesssim 10$.

In order to measure the heating rate with the help of the above described method, a waiting time t_{wt} has to be included in the measurement sequence:

1. The ion is ground state cooled via Doppler and sideband cooling and initialised in the ground state of the electronic qubit by optical pumping.
2. During a waiting time t_{wt} all lasers are turned of.
3. A blue sideband (red sideband) pulse with constant intensity and excitation time t_{opt} is applied.
4. The ion's electronic state is detected by electron shelving.

Repeating this sequence enough times to reduce statistical errors (typically around 1000 repetitions), allows one to determine $P_{D,\mathrm{BSB}}(t_{\mathrm{wt}})$ and $P_{D,\mathrm{RSB}}(t_{\mathrm{wt}})$. This enables one to calculate the mean phonon number for different waiting times. The heating rate Γ_{h} is then given by the slope of a linear fit of the obtained data.

Chapter 4

Design of high-temperature superconducting traps

In the previous chapter it was described that the origin of anomalous heating is not well understood and the magnitude of motional heating is higher than expected from theoretical models in many ion traps. Too large motional heating can reduce the fidelity of two-qubit-gates and therefore reduce the accuracy of computations with an ion trap quantum computer [9]. It is especially an issue for surface-electrode ion traps, because the heating rates are higher when ions are trapped closer to surfaces [17]. The fact that the origin of anomalous heating is not well understood, complicates the search for means to reduce it.

The aim of this project is to gain further knowledge about the underlying effects of motional heating by investigating two different sources of noise. In electronic circuits Johnson noise is well characterised, but its effect on motional heating in an ion trap has not been verified yet. Our designs presented in this chapter should enable us to characterise the effects of Johnson noise produced by a resistor. To minimise the influence of wires and the electronic circuit, a resistor is directly integrated on the trap chip. Besides Johnson noise other noise sources presumably caused by the trap surface will be present in our system. To compare the characteristics of these other noise sources with Johnson noise, the trap is designed in a way such that the magnitude of Johnson noise can be varied by several orders of magnitude without affecting the other noise sources. This control over the magnitude of Johnson noise can be achieved by using a superconductor as the trap electrode material. As the resistance vanishes below the critical temperature T_{c}, Johnson noise is negligible at these temperatures and the other noise sources can be characterised. Increasing the temperature by only a few Kelvin above T_{c}, increases the resistance by several orders of magnitude and allows us to design the trap in a way that Johnson noise should be the dominant source of motional heating above T_{c}.

As Johnson noise is proportional to T, using a high-temperature superconductor simplifies reaching a high enough magnitude of Johnson noise to make it dominant above T_{c}. Additionally, this project is the first report of a high-temperature superconductor used as a material for ion traps. The high-temperature superconducting material YBCO is already used for many applications like Josephson-junctions or SQUIDS and therefore reliable microfabrication techniques are existing [24]. This is the reason why it is a promising

trap electrode material for our project.

At the beginning of this chapter a short introduction to the general properties of superconductors and in particular to the trap electrode material YBCO is presented in section 4.1. Informations about the trap chip production are given in section 4.2. The trap design is based on the silicon traps in [45]. It is presented and simulated in section 4.3 and serves as a starting point for the calculations on how to make Johnson noise dominant in section 4.4. These calculations show the need of a high resistance causing the issue of a not RF-grounded DC-electrode addressed in section 4.4.3. As this issue cannot be solved without modifying the design, it motivates the final optimised designs for this project. With the focus on the applied modifications, they are presented in section 4.5. Finally, additional means to reduce the effects of a not RF-grounded DC-electrode are given in section 4.6.

4.1 High-temperature superconductor YBCO

4.1.1 Introduction to superconductivity

The absence of resistivity below a critical temperature T_c was discovered by H.K. Onnes in 1911 [46]. He measured a sudden drop of the resistivity to zero at $4.2\,\mathrm{K}$ in pure mercury. In 1933 Meissner and Ochsenfeld discovered that perfect diamagnetism is another property of the superconducting state [47]. At closer observation, a superconductor has the following properties [23]:

1. The resistivity $\rho = 0$ for all $T < T_\mathrm{c}$ as long the current does not exceed a material-dependent critical current density j_c.

2. The magnetic field $B = 0$ inside the superconductor as long as the magnitude of the external magnetic field is below a material-dependent critical field strength.

An example of the temperature dependence of the resistivity of a superconducting material is depicted in figure 4.1. The sharp increase of the resistivity above T_c is characteristic for a superconductor. At higher temperatures it shows a metal-like linear temperature dependence.

Superconducting materials are sorted into two groups [23]:

1. For $T_\mathrm{c} < 77\,\mathrm{K}$, the boiling point of nitrogen, they are typically called conventional superconductors.

2. For $T_\mathrm{c} > 77\,\mathrm{K}$ they are called high-T_c or high-temperature superconductors.

It should be noted that this is not a strict definition. For example, LaBaCuO ($T_\mathrm{c} = 30\,\mathrm{K}$) is usually considered a high-T_c superconductor [49].

4.1.2 High-temperature superconductors

The superconductivity in $\mathrm{La}_{2-x}\mathrm{Ba}_x\mathrm{CuO}_4$ was first measured by Georg Bednorz and Klaus Alex Müller in 1986 and their publication "Possible High-T_c Superconductivity in the Ba-La-Cu-O System" [49] can be seen as the discovery of high-temperature superconductors.

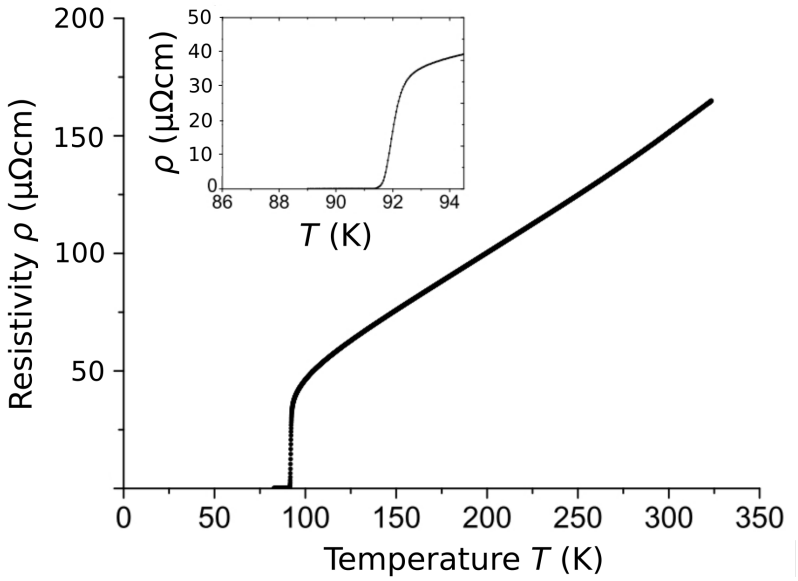

Figure 4.1: The plot from [48] shows the temperature dependence of ρ in a YBCO-film. Below $T_c \approx 91\,\mathrm{K}$ the resistivity is zero. Around T_c the resistivity increases strongly in a small temperature range of around 2 K. For higher temperatures the resistivity depends linearly on the temperature like it is typical for metals. Figure courtesy of German Hammerl.

A year later Maw-Kuen Wu and Paul Chu discovered the superconductivity in YBCO ceramics with $T_c \approx 92\,\mathrm{K}$ [23]. The fact that the transition temperature is above the temperature of liquid nitrogen made these superconductors attractive for many applications, because cooling with liquid nitrogen is much cheaper than with liquid helium. An example are SQUIDs (superconducting quantum interference devices), which are very sensitive magnetometers with applications in medicine among other things [24]. Another example would be low loss power lines. Until now the copper oxide with the highest critical temperature at ambient pressure is $HgBa_2Ca_2Cu_3O_{8+\delta}$ with $T_c \approx 135\,\mathrm{K}$ [50]. Higher critical temperatures can be reached under a high pressure. For example, $HgBa_2Ca_2Cu_3O_{8+\delta}$ was measured to be superconducting up to $164\,\mathrm{K}$ at $31\,\mathrm{GPa}$ [51]. In 2015 an even higher critical temperature of $203\,\mathrm{K}$ was discovered in H_3S at $150\,\mathrm{GPa}$ [52].

For this project a high-T_c superconductor has the following advantage: At $T = T_c$ Johnson noise is higher for a high-T_c superconductor than for a conventional superconductor, because it is proportional to the temperature T. As for this project, it should be the dominant source of motional heating above T_c, the required resistance to produce enough Johnson noise is smaller for a high-T_c superconductor than for a conventional superconductor (details on the calculation of the required resistance are given in section 4.4.2). YBCO was chosen for this project and its properties are described in the next section.

4.1.3 The properties of YBCO

The abbreviation YBCO stands for $YBa_2Cu_3O_{6+x}$. The partial oxygen content x is crucial for the properties of the material. For $x < 0.4$ it is an insulator, whereas for $0.4 < x < 1$ it is a superconductor [23]. Different oxygen contents lead to a spread of the critical

temperature around $90\,\mathrm{K}$. Like many superconductors, the resistivity ρ shows a linear temperature dependence above the sharp increase at T_c. Compared to metals ρ is rather high. Additionally, ρ is highly anisotropic. In the plane of the YBCO structure where the material exhibits superconductivity, $\rho \approx 10^2\,\mu\Omega\,\mathrm{cm}$ for $T \approx 100\,\mathrm{K}$ [23]. This is approximately 500 times higher than the resistivity of copper [53].

YBCO is a type-II superconductor, i.e. it has two critical magnetic fields $B_{\mathrm{c}1}$ and $B_{\mathrm{c}2}$ with $B_{\mathrm{c}1} < B_{\mathrm{c}2}$. For $B < B_{\mathrm{c}1}$ the magnetic field is completely expelled from the material (similar to type-I superconductors). For $B_{\mathrm{c}2} > B > B_{\mathrm{c}1}$, type-II superconductors are in a mixed state, where the magnetic field partly penetrates the material and the resistivity is still zero. For $B > B_{\mathrm{c}2}$ they become normal. This behaviour leads to high critical fields $B_{\mathrm{c}2}$ up to several Tesla and critical current densities j_c up to $10^7\,\mathrm{A/cm^2}$ [23].

4.2 Trap chip production

The chips were produced by two companies. The YBCO film was produced by Ceraco[1] in Munich. Afterwards the chips were patterned by STAR Cryoelectronics[2] in Santa Fe. All available information about the production is given in this section.

4.2.1 Thin layer deposition

The layer of YBCO was deposited on a 3-inch wafer made of a $0.5\,\mathrm{mm}$ thick sapphire substrate. Ceraco offers 8 different substrates [54]. We chose sapphire, because it has low RF losses and a very high thermal conductivity of $10^3\,\mathrm{W/(mK)} - 10^5\,\mathrm{W/(mK)}$ in the range of $10\,\mathrm{K} - 100\,\mathrm{K}$. This is comparable to the thermal conductivity of copper at these temperatures [53]. Additionally, the small dielectric constant $\epsilon_r \approx 10$ reduces the coupling between the RF- and the DC-electrodes. The magnitude of this coupling affects the RF-grounding of DC-electrodes as described in section 4.4.3.

Between the $50\,\mathrm{nm}$ thick YBCO layer and the sapphire substrate, a $40\,\mathrm{nm}$ thick buffer layer of CeO_2 is added. Ceraco offers three different types of YBCO layers, which differ in the amount of partial oxygen content and therefore in the characteristic specifications for T_c and j_c. One of these types is called S-type and it is most suitable for our project, because structures down to a few microns can be patterned and it has a rather high T_c and j_c. A scanning electron microscope (SEM) picture taken from a test structure in the same fabrication run shows the typical surface of the film (see figure 4.2).

The YBCO layer was covered by an in situ evaporated $200\,\mathrm{nm}$ gold layer. In general, the gold layer is used to protect the YBCO from influences due to direct contact with air. In particular, high humidity can lead to a degradation of the superconducting properties. In addition, the gold layer is needed to contact the chip electrodes with gold wire bonds.

Ceraco measured the properties of the YBCO film right after the fabrication process and found a critical temperature $T_\mathrm{c} = 85.6(5)\,\mathrm{K}$ and a critical current $j_\mathrm{c} = 3.3\,\mathrm{MA/cm^2}$ at $77\,\mathrm{K}$.

[1] Ceraco ceramic coating GmbH http://www.ceraco.de

[2] http://www.starcryo.com

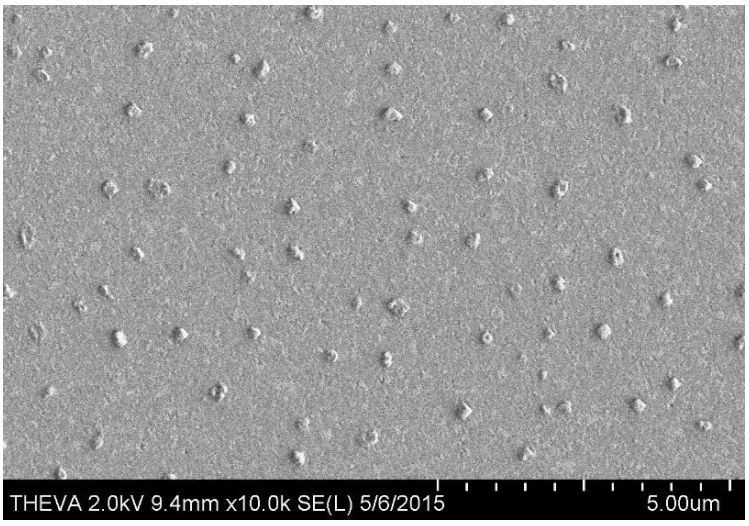

Figure 4.2: Scanning electron microscope (SEM) picture of the YBCO-film right after its deposition done by Ceraco. The surface topography is typical for S-type YBCO-films, one of three possible types produced by Ceraco. Picture courtesy of Robert Semerad.

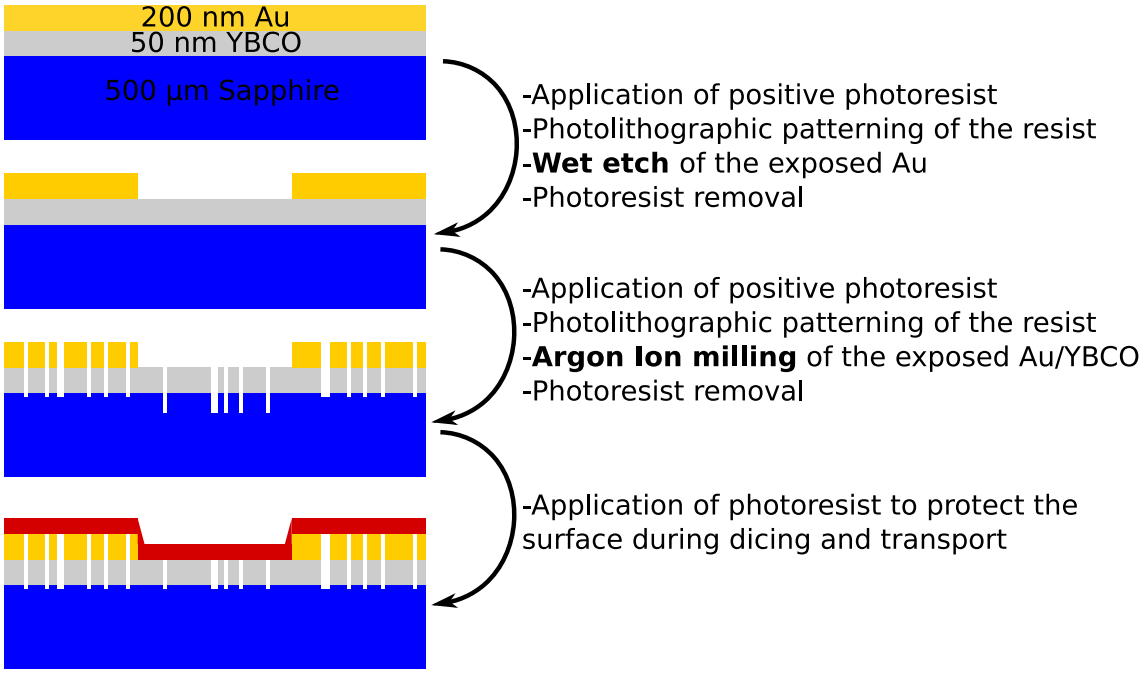

Figure 4.3: Overview over the involved steps during the chip fabrication process. In the first step on some parts of the chip the Au layer is removed, because parts of the chip should have the high resistance of YBCO above T_c. During the next step the electrode structure is patterned into the chip. This is indicated by the gaps in the 3rd and 4th schematic. Finally, the chips are covered by a photoresist to protect them from damage during dicing and transport.

4.2.2 Chip patterning

The patterning and the dicing was done by STAR Cryoelectronics. The steps are described in the following and are shown in a schematic overview in figure 4.3.

As a first step, on some parts of the chip the gold layer was removed by a wet etch process [55]. This is necessary, because parts of the chip should have a high resistance above T_c. This is only possible if the gold layer, which has a much smaller resistance compared to the YBCO layer is removed from these parts. Additionally, on some traps the gold layer is removed completely around the trapping area in order to investigate the surface noise properties of YBCO. Afterwards the wafer was patterned by argon ion milling [55]. Before dicing the chips were covered by a photoresist in order to protect the surface.

4.3 Simulation of the linear trap design

The trap design of this project is based on the Yedikule-3 design [29]. Due to some slight modifications it is named 'HTCYK1' in this thesis. The layout of HTCYK1 is depicted in figure 4.4. It consists of an $8\,\mathrm{mm}$ long RF-electrode with one central DC-electrode and 3 DC-electrodes on each side. The trap in [29] was simulated with COMSOL Multiphysics 3.4 in combination with MATLAB, whereas the "*electrode package*" [56] was used for the simulations in this thesis. Therefore a short introduction about the basic assumptions behind this simulation and a description how these simulations are done will be given in this section.

4.3.1 The gapless approximation for surface traps

To calculate the electric fields and potentials in an arbitrary setup of given electrodes, one in general has to solve differential equations with an appropriate software like for example COMSOL Multiphysics. However, as shown in [57], above a surface trap they can be calculated analytically under the following assumptions:

- **The gapless approximation**: No gaps are present in between the electrodes.
- **Infinite plane approximation**: The electrodes are assumed to cover an infinite plane.

This approach results in a much shorter computation time. Due to the above given assumptions the effects of the electrode thickness and the dielectric properties of the underlying substrate are also neglected in the simulations. However, Roman Schmied demonstrates that these influences are small in realistic situations, the errors are usually exceeded by those due to stray fields and microfabrication tolerances [58]. He implemented this calculations in a Mathematica code (available at [59]). Based on that Robert Jördens programmed the *electrode package* in Python [56]. The latter one is used for the simulations in this master thesis and therefore in the following section we present how to use the *electrode package* for simulating ion traps with a given electrode structure. Despite the fact that they were not used in this thesis, it should be noted, that the software also includes trap geometry optimization functions based on [60].

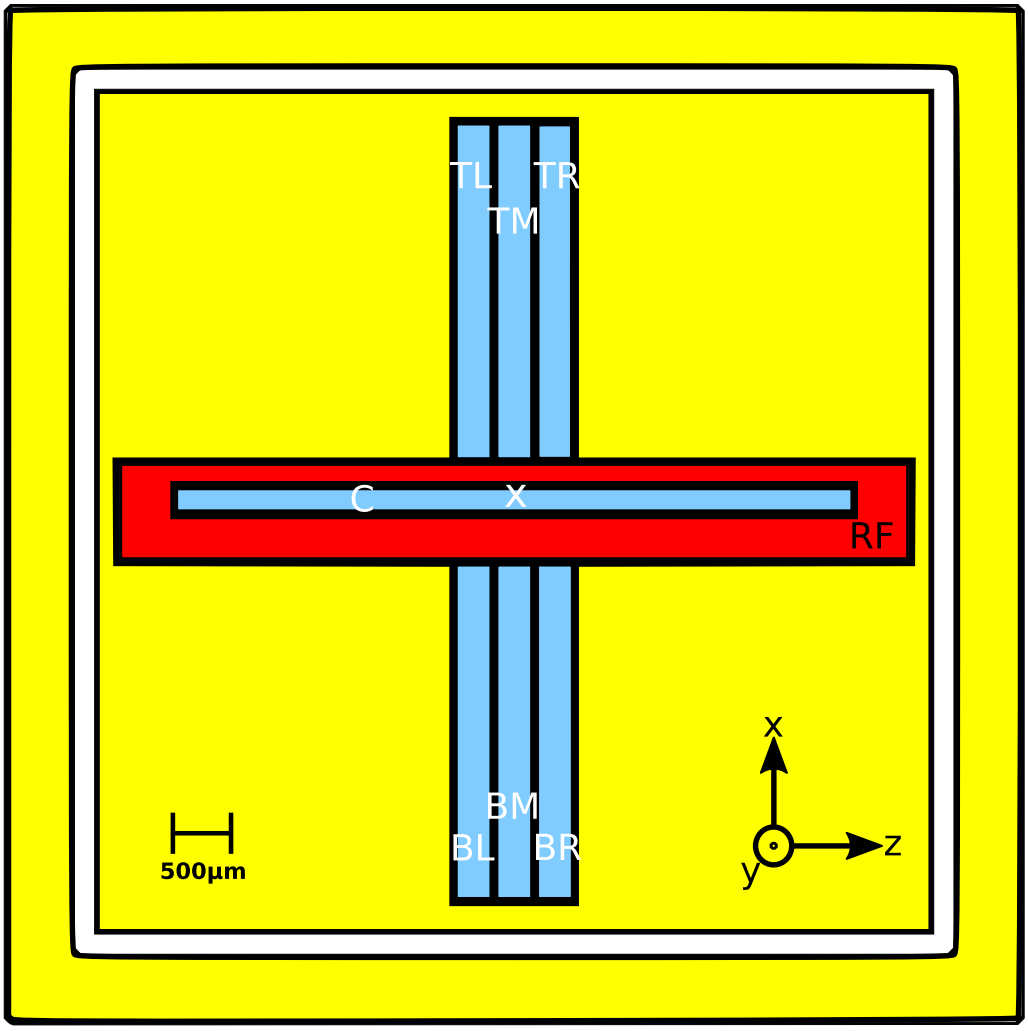

Figure 4.4: Layout of the basic linear trap design (HTCYK1). The red colored electrodes are connected to an RF-resonator, the blue ones are DC-electrodes and the yellow parts are electrically grounded. The DC-electrodes are labelled according to their position (TL = top left, TM = top middle, ... , C = center). The x in the center marks the position of the ion and the origin of the coordinate system for the simulations. The gap size between the electrodes is $10\,\mu\mathrm{m}$.

4.3.2 Simulating ion traps with the electrode package

This section is an introduction to surface trap simulations using the *electrode package*. It is partly based on the tutorial by Robert Jördens [56]. In the following, the software functions are written in *italic* and the classes are written in **bold**. An example code is given in appendix C.

The first step to simulate a given electrode structure in the *electrode package* is defining the electrode layout using the classes **System** and **PolygonPixelElectrode**, where each electrode is represented by a polygon. To define the electrode layout the following points have to be considered:

- It is not possible to implement gaps in the electrode structure. Therefore we increased the size of the two electrodes next to a gap such that each of them fills up half of the gap space.
- The polygon points should be given in a counterclockwise order. Otherwise the voltage assigned to the electrodes will have a reversed sign in the simulations.
- The dimension of the electrodes affect the dimension of the simulations. This means if the size of the electrodes is given in $\mu\mathrm{m}$, then the electric fields will be given in $\mathrm{V}/\mu\mathrm{m}$.

To visually control the implemented electrode layout, it can be plotted using *System.plot*.

After that the RF-voltage is assigned to the RF-electrode. As shown in section 2.1.1 the RF-field creates a pseudopotential that traps the ion. If one scales the RF-voltage by a factor $Q^2/(4m\Omega_{\mathrm{RF}}^2)$, the value of the simulated potential is identical to the pseudopotential seen by the ion. The minimum of the pseudopotential can be found with *System.minimum*. In the case of a linear trap, the RF-field confines the ion in only two dimensions. One must apply DC-voltages to the DC-electrodes in order to trap the ion in all 3 dimensions. An appropriate set of DC-voltages can be calculated with *System.shims*. This function calculates voltage sets according to constraints, which are given to the function as arguments. By constraining the DC electric field to be zero at the desired trapping position, a voltage set for axial confinement can be calculated. After assigning the voltages to the DC-electrodes the secular frequencies are calculated with the help of *System.modes*.

System.shims additionally enables one to calculate shim voltage sets, i.e. voltage sets that produce an electric field with only an x-,y- or z-component at the position of the ion. These can be used to move the ion in order to compensate for micromotion without affecting the curvature of the electric field and consequently without affecting the trapping frequencies.

The trap-depth is obtained in the following way: First the position of the lowest saddle point around the trap minima can be approximated by looking at a plot of the total effective potential (an example is shown in figure 4.5). Then this approximation is used to calculate the exact position with *System.saddle*. It calculates also the potential Φ_{sp} of this saddle point. Finally, the trap depth is given by $\Phi_{\mathrm{sp}} - \Phi_{\mathrm{m}}$, where Φ_{m} is the potential at the trap minimum. The results of the simulations for HTCYK1 are presented in the next section.

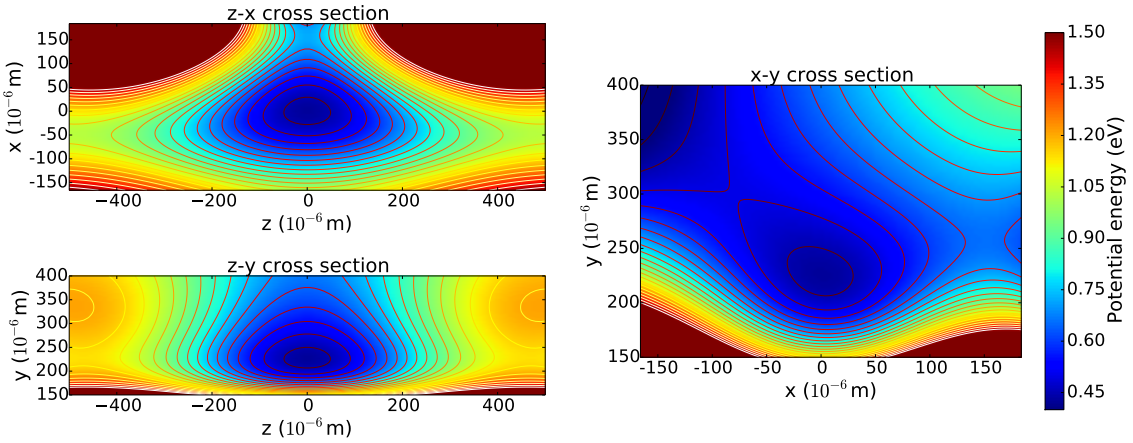

Figure 4.5: Total effective potential (with applied DC- and RF-voltages) of HTCYK1 for the cross sections through the trap minimum at $x = 0\,\mu\text{m}, y = 226\,\mu\text{m}$ and $z = 0\,\mu\text{m}$. The main escape channel for the ion is through the saddle point at $(-79\,\mu\text{m}, 299\,\mu\text{m}, 0\,\mu\text{m})$. The spacing between contour lines is $50\,\text{meV}$.

RF		TL	TM	TR	BL	BM	BR	C
RF-amplitude V_{peak} (V)	Drive frequency $\Omega_{\text{RF}}/2\pi$ (MHz)	DC-voltage (V)						
176	18.97	29.38	-29.38	29.38	6.48	-29.38	6.48	1.10

Table 4.1: RF- and DC-voltages, used for the simulations of HTCYK1 in this section. The chosen RF-frequency is the resonance frequency of the RF-circuit used for the measurements in section 6.3.

4.3.3 Simulation results

The simulation of HTCYK1 is obtained with the program code given in appendix C. The voltages which are used for the simulations are given in table 4.1. As described in the previous section, the first step to analyse the trap is to find the minimum of the pseudopotential resulting from the applied RF-voltage. A plot of the pseudopotential is shown in figure 4.6; the trap minimum is $226\,\mu\text{m}$ above the surface (at $x = 0\,\mu\text{m}, y = 226\,\mu\text{m}$ and $z = 0\,\mu\text{m}$). One can clearly see the pseudopotential tube along the z-axis, which is characteristic for linear traps. As expected for a surface trap the escape channel for an ion is nearly orthogonal to the trap surface. In a linear trap it is assumed that the RF-field produces only a negligible small curvature along the z-axis. This assumption holds for HTCYK1, because $\omega_{\text{RF},z}/\omega_{\text{RF},r} = 6 \times 10^{-5}$, where $\omega_{\text{RF},z}$ is the secular frequency in the z-direction and $\omega_{\text{RF},r}$ the secular frequency in the radial direction.

Adding the DC-voltages confines the ion along the z-axis. The DC-voltage set for this simulation is given in table 4.1 and results in an axial secular frequency $\omega_z = 2\pi \cdot 1.05\,\text{MHz}$. The resulting total effective potential is depicted in figure 4.5. The main

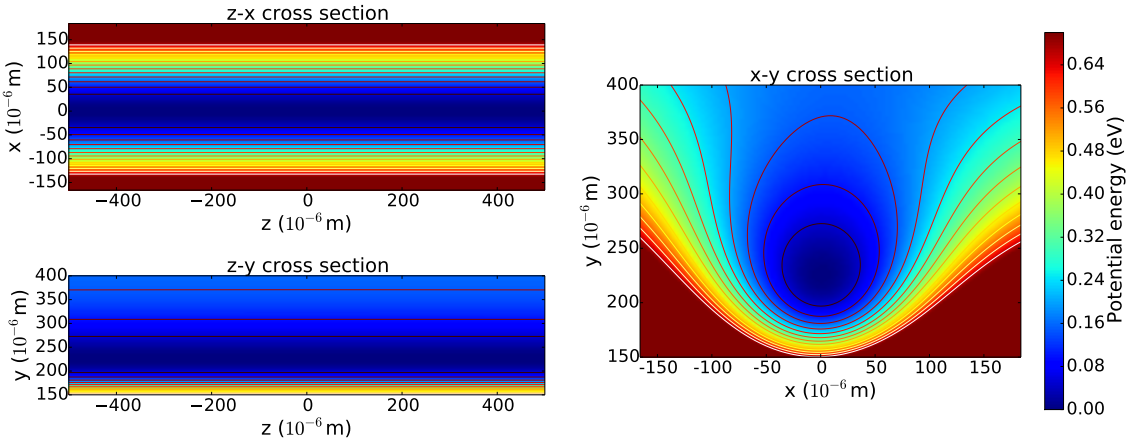

Figure 4.6: Pseudopotential resulting from an applied RF-voltage on the RF-electrode of HT-CYK1. Cross sections are taken through the trap minimum at $x = 0\,\mu\mathrm{m}, y = 226\,\mu\mathrm{m}$ and $z = 0\,\mu\mathrm{m}$. Along the z-axis one can see a pseudopotential tube which is characteristic for linear traps. The spacing between contour lines is $50\,\mathrm{meV}$.

Trap depth (meV)	Secular frequencies		
	$\omega_z/2\pi$ (MHz)	$\omega_{r1}/2\pi$ (MHz)	$\omega_{r2}/2\pi$ (MHz)
72	1.05	1.70	2.47

Table 4.2: Trap parameters obtained from the RF- and DC-voltages listed in table 4.1.

escape channel for the ion is now through the saddle point at $(-79\,\mu\mathrm{m}, 299\,\mu\mathrm{m}, 0\,\mu\mathrm{m})$. The potential that goes through the trap minimum and the saddle point is shown in figure 4.7. The trap depth is $\Phi_{\mathrm{sp}} - \Phi_{\mathrm{m}} = 72\,\mathrm{meV}$. The fact that the radial modes are tilted out of the plane parallel to the trap surface is important as it allows us to cool all modes with a laser that is parallel to the trap surface. The secular frequencies are calculated from the potential at the ion position. They are given in table 4.2.

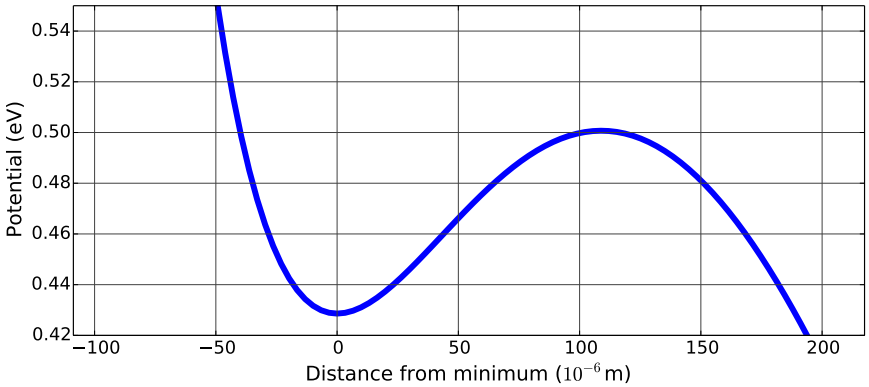

Figure 4.7: Total effective potential along the line going through the trap minimum Φ_{m} and the saddle point Φ_{sd}. The trap depth is given by $\Phi_{\mathrm{sp}} - \Phi_{\mathrm{m}} = 72\,\mathrm{meV}$.

4.4 How to make Johnson noise dominant above T_{c} and the resulting problems

In section 3.1 it was explained that the motional heating resulting from Johnson noise can be calculated in the following way: The characteristic distance from the electrode to the ion and the effective real resistance between the trap electrode and electrical ground have to be determined. Due to the fact that the effective resistance is always finite, Johnson noise is present in all ion traps. However, as long as the resistance is low enough, Johnson noise is negligible compared to other heating mechanisms. To produce on purpose a level of Johnson noise exceeding the level of the other noise sources, a high resistance has to be connected to one of the electrodes.

In this project the resistance is formed by a structure made of YBCO integrated on the trap chip. Above the critical temperature of YBCO $T_{\mathrm{c}} \approx 86\,\mathrm{K}$, the resistance of this structure increases strongly and produces Johnson noise.

In the experiment we want to be able to identify two regimes: Below T_{c} we will be limited by an yet unknown noise source with the electric field noise density $S_{T_{\mathrm{c}}}$. Above T_{c} we want Johnson noise to be the dominant noise source. In order to clearly identify the two regimes, the electric field noise density of Johnson noise S_{JN} has to be at least an order of magnitude higher than the other noise sources $S_{T_{\mathrm{c}}}$. In order to determine the resistance required to make Johnson noise dominant, we first estimate $S_{T_{\mathrm{c}}}$ in section 4.4.1. Afterwards in section 4.4.2, the Johnson noise per resistance S_{JN}/R is calculated. To ensure that Johnson noise is dominant above T_{c}, we chose R so that $S_{\mathrm{JN}} = 10 S_{T_{\mathrm{c}}}$.

4.4.1 Expected electric field noise around $T_c \approx 86\,\mathrm{K}$

The heating rate Γ_h in ion traps depends on many different parameters, e.g. the trap frequency, the ion-electrode separation, the trap temperature and the experimental setup around the trap [17]. In addition, surface contaminations on the trap seem to affect the heating rate [17].

These complex dependencies make it impossible to precisely predict the heating rate in the YBCO-traps. Nevertheless, it is estimated in the following. The traps in [29] serve as a starting point, because they have the same ion-electrode separation and were used in the same experimental setup as the YBCO traps. Two types of traps were tested in [29]. In one of them silica is used as the substrate material, in the other one the substrate is silicon. Both of them use gold as a top electrode layer. The silica trap shows on average $\Gamma_h = 41(5)\,\mathrm{phonons/s}$ for an axial frequency $\nu \approx 1\,\mathrm{MHz}$. At the same trap frequency most of the investigated silicon traps have a heating rate of approximately $1\,\mathrm{phonon/s}$. All these traps were operated at temperatures around $10\,\mathrm{K}$ and therefore the heating rates have to be extrapolated to $T \approx 86\,\mathrm{K}$.

The overview of motional heating rate measurements in ion traps given in [17] clearly shows a reduction of the heating rate with decreasing temperature. A rough estimation shows that it is reduced by two orders of magnitude between room temperature and $T \approx 6\,\mathrm{K}$. Until now only two experiments investigated the temperature scaling of traps within one setup [61, 62]. While these two experiments observe a different temperature scaling, both measure an increase of Γ_h by approximately one order of magnitude from $10\,\mathrm{K}$ to $86\,\mathrm{K}$. Consequently, we expect $\Gamma_h(86\,\mathrm{K}) \lessapprox 4 \times 10^2\,\mathrm{phonons/s}$, which according to equation (3.1) corresponds to an electric field noise spectral density $S_{T_c} \lessapprox 3 \times 10^{-12}\,\mathrm{V^2/(m^2Hz)}$.

4.4.2 Calculation of the required resistance

We need to choose an appropriate resistance based on the estimations above. This is done by first calculating the Johnson noise per resistance S_{JN}/R and then choosing R, so that $S_{JN} = 10 S_{T_c} \approx 3 \times 10^{-11}\,\mathrm{V^2/(m^2Hz)}$. R is a YBCO-structure connected to the TM-electrode (the DC-electrode in the middle on the top side; see layout in figure 4.4). The heating rate measurement will be done in the axial mode z with frequency ω_z. With equation (3.3) the Johnson noise is then given by

$$\frac{S^{JN}_{z,TM}}{R(\omega_z, T)} = \frac{4 k_B T}{D^2_{z,TM}}, \tag{4.1}$$

with the characteristic distance $D_{z,TM} = V_{TM}/E_{z,TM}$. The induced electric field in the z-direction $E_{z,TM}$ resulting from the voltage V_{TM} on the TM-electrode is calculated with the *electrode package* by using *System.individual_potential*. Figure 4.8 shows the resulting Johnson noise as a function of the ion position along the z-axis. The maximum noise $S_{E,max}$ is reached at $z_m = \pm 285\,\mu\mathrm{m}$. For $T = 100\,\mathrm{K}$ and $R = 1\,\Omega$ it is $S_{E,max} = 2.5 \times 10^{-17}\,\mathrm{V^2/(m^2Hz)}$ .Therefore $S_{JN} \approx 3 \times 10^{-11}\,\mathrm{V^2/(m^2Hz)}$ is reached when a resistance $R \approx 1\,\mathrm{M\Omega}$ is connected to the TM-electrode.

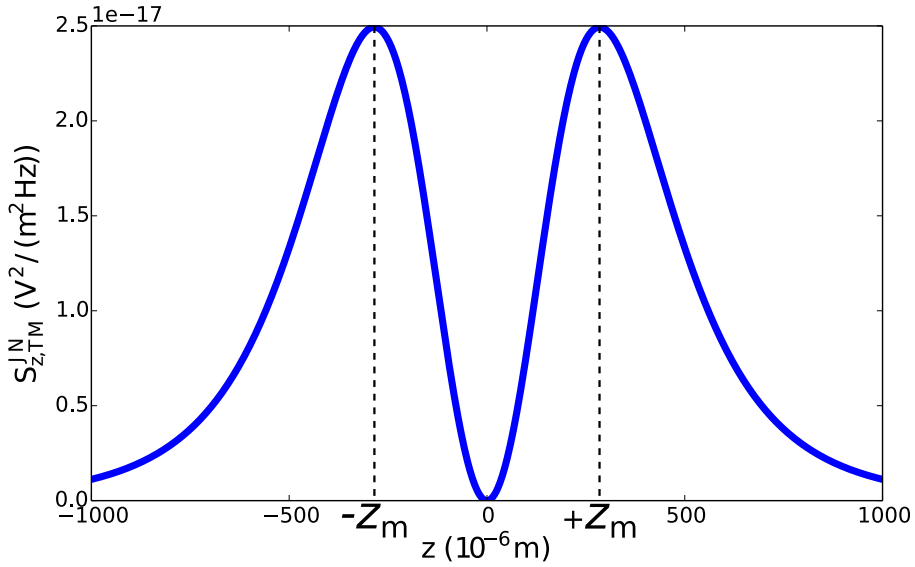

Figure 4.8: Johnson noise from the TM-electrode for $T = 100\,\mathrm{K}$ and $R = 1\,\Omega$ as a function of the ion position along the z-axis of the trap. The Johnson noise is obtained with equation 4.1, where the characteristic distance was calculated using the *electrode package*.

To include such a large resistance on the trap chip, a long and thin trace of YBCO is needed. For a $10\,\mu\mathrm{m}$ trace width and a $50\,\mathrm{nm}$ thick YBCO layer the trace would have to be $0.3\,\mathrm{m}$ long. A practical way to include such a trace on the trap chip is to form a meander shape (examples can be seen in figure 4.10).

However, connecting $R_{\mathrm{meander}} \approx 1\,\mathrm{M}\Omega$ to a DC-electrode (the meander-electrode) hinders the RF-grounding of this electrode. This issue is explained in detail in the following section.

4.4.3 Proper RF-grounding of DC-electrodes

In a trap design it is usually assumed that all DC-electrodes are RF-grounded. If this is not ensured in the experimental setup, an RF-pickup is present on the DC-electrodes. Depending on the phase and the amplitude of the RF-pickup, it can lead to non compensable micromotion [63], it can reduce the trap depth or even prevent from trapping an ion.

To understand how an RF-pickup can arise on a DC electrode we consider the circuit in figure 4.9. It shows the complete electronic circuit between the RF-electrode and the DC-voltage source including the capacitive coupling C_{C} between the RF- and the DC-electrode and filters. The capacitive coupling C_{C} can create an RF-pickup $V_{12,\mathrm{RF}}$ on the DC-electrode. An electrode is considered RF-grounded, if no RF-voltage $V_{12,\mathrm{RF}}$ is present on the DC-electrode. Proper RF-grounding of the DC-electrodes can be achieved in the following way: A capacitance C_{F} to electrical ground is installed along the connection to the DC-electrode. It is shown later in this section that the rest of the filter components apart from C_{F} do not influence the RF-grounding of the DC-electrode. The RF-pickup

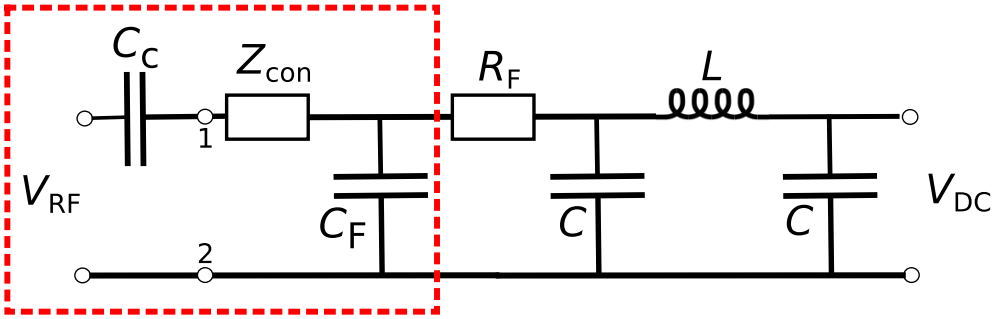

Figure 4.9: Schematic electronic circuit of the RF-grounding of a DC-electrode. On the left side is the RF-voltage V_{RF} applied to the RF-electrode. C_C is the capacitive coupling between the RF-electrode and the DC-electrode (point 1), C_F is a capacitance to ground (point 2) and Z_{con} is the impedance of the wiring between them. $V_{12,RF}$ is the RF-voltage between point 1 and 2 and is also called RF-pickup. The DC-electrode at point 1 is RF-grounded, if $V_{12,RF} \approx 0$. The components outside of the red box are the rest of the DC-filter components and the DC power supply V_{DC}. R_F and C_F form a RC-filter. The two other capacitors C and the inductance L build up a PI-filter. It will be verified in the main text, that only the components inside the red box affect the RF-grounding.

$V_{12,RF}$ is negligible for

$$Z_{C_C} \gg Z_{C_F} + Z_{con}, \tag{4.2}$$

where the impedance of the capacitances are $Z_{C_F} = 1/(i\omega C_F)$ and $Z_{C_C} = 1/(i\omega C_C)$, ω is the radio-frequency and Z_{con} is the impedance of the connection between C_C and C_F. In this case the whole RF-voltage V_{RF} between the RF-electrode and electrical ground drops at C_C and $V_{12,RF}$ is negligibly small. The following calculation shows that if a high resistance like a YBCO meander structure is connected to the DC-electrode, than the DC-electrode is RF-grounded below T_c. However, above T_c a significant RF-pickup is present on the DC-electrode.

In our setup, for the TM-electrode it can be approximated that $0.03\,\mathrm{pF} < C_C < 0.5\,\mathrm{pF}$ (see appendix A). $C_F = 330\,\mathrm{nF}$ is given by the last capacitor of the filterboard. The next filter component is a resistor $R_F = 100\,\Omega$. For a radio frequency $\omega_{RF} = 2\pi \cdot 19\,\mathrm{MHz}$, the impedance $|Z_{C_F}| = 1/(\omega C_F) \approx 0.03\,\Omega \ll R_F$. Therefore all the filter components besides C_F and the DC-power source do not affect the RF-grounding.

The YBCO meander with the resistance $R_{meander}$ is directly on the trap chip and it is part of Z_{con}. For $T < T_c$, $R_{meander} = 0$. Z_{con} is usually at maximum a few Ω. For $C_C = 0.1\,\mathrm{pF}$ and $\omega_{RF} = 2\pi \cdot 19\,\mathrm{MHz}$, $Z_{C_C} \approx 8\,\mathrm{k}\Omega$. Therefore the requirement $Z_{C_C} \gg Z_{C_F} + Z_{con}$ is fulfilled and the DC-electrode is properly RF-grounded.

For $T > T_c$, Z_{con} is dominated by $R_{meander}$ and $V_{12,RF}$ is given by

$$V_{12,RF} = \frac{R_{meander} + Z_{C_F}}{R_{meander} + Z_{C_F} + Z_{C_C}} \cdot V_{RF}. \tag{4.3}$$

As $C_F \gg C_C$, $Z_{C_F} \ll Z_{C_C}$ and $R_{meander} \gg Z_{C_F}$, equation (4.3) can be simplified to

$$V_{12,RF} \approx \frac{R_{meander}}{R_{meander} + Z_{C_C}} \cdot V_{RF}. \tag{4.4}$$

Taking the same values as above ($C_\mathrm{C} = 0.1\,\mathrm{pF}$ and $\omega_\mathrm{RF} = 2\pi \cdot 19\,\mathrm{MHz}$, $Z_{\mathrm{C_C}} \approx 8\,\mathrm{k\Omega}$) and $R_\mathrm{meander} = 1\,\mathrm{M\Omega}$ leads to $V_\mathrm{12,RF} \approx V_\mathrm{RF}$ and the DC-electrode is not properly RF-grounded.

In summary, for $T < T_\mathrm{c}$ the DC-electrode with the attached meander is well RF-grounded, whereas for $T > T_\mathrm{c}$ the meander resistance causes an RF-pickup $V_\mathrm{12,RF}$ on the DC-electrode that has the same magnitude as the RF-voltage V_RF. This pickup could prevent from trapping or at least produce not compensable micromotion. Consequently, the trap design was modified in a way to minimize $V_\mathrm{12,RF}$. The optimised designs are presented in the following section. Additional means to reduce $V_\mathrm{12,RF}$ are presented in section 4.6.

4.5 Final trap designs

To overcome the problems described in the last section, two new trap designs were developed: the one-meander and the two-meander design. Both of them have in common that the central DC-electrode is split into three electrodes. In the one-meander design one of these is used as the meander-electrode. In the two-meander design two are used as the meander-electrodes. In both designs the meander-electrodes have a smaller characteristic distance than the TM-electrode and the Johnson noise per resistance is increased. Therefore, a smaller resistance can be used to produce the magnitude of Johnson noise required to exceed the other noise sources.

4.5.1 One-meander design

The one-meander design is optimised in a way to minimize the characteristic distance D of the meander-electrode while the capacitive coupling C_C between the meander-electrode and the RF-electrode is not increased significantly. The empirical optimisation was performed by simulating different electrode sizes and shapes. The final design is shown in figure 4.10.

The general layout is similar to HTCYK1. It consists of a $7\,\mathrm{mm}$ long RF-electrode and 5 DC-electrodes on each side. The main difference is that the central DC-electrode is split into three parts. One of them is situated in the centre of the trap right under the trapping site. This so-called CC-electrode is $400\,\mu\mathrm{m}$ long in the z-direction, on the upper side it is separated from the RF-electrode by a $10\,\mu\mathrm{m}$ gap and on the lower side it ends next to a $30\,\mu\mathrm{m}$ trace of the other central electrode (a zoom in on the CC-electrode is provided in figure 4.11). The CC-electrode is used as the meander-electrode. It can be connected to the meanders on the lower side of the chip via a trace that goes from the CC-electrode to the left end of the RF-electrode and then downwards. This trace introduces an asymmetry, which is reduced by a second trace from the CC-electrode to the right. The other two remaining parts of the central electrode can be connected together by bonding wires and they are used together as one DC-electrode.

The spatial dependence of Johnson noise from the CC-electrode is depicted in figure 4.12. It was calculated for $T = 100\,\mathrm{K}$ and $R = 1\,\Omega$. The Johnson noise has two maxima along the z-axis. The highest is $S_\mathrm{E1} = 1.04 \times 10^{-15}\,\mathrm{V^2/(m^2Hz)}$, and is located

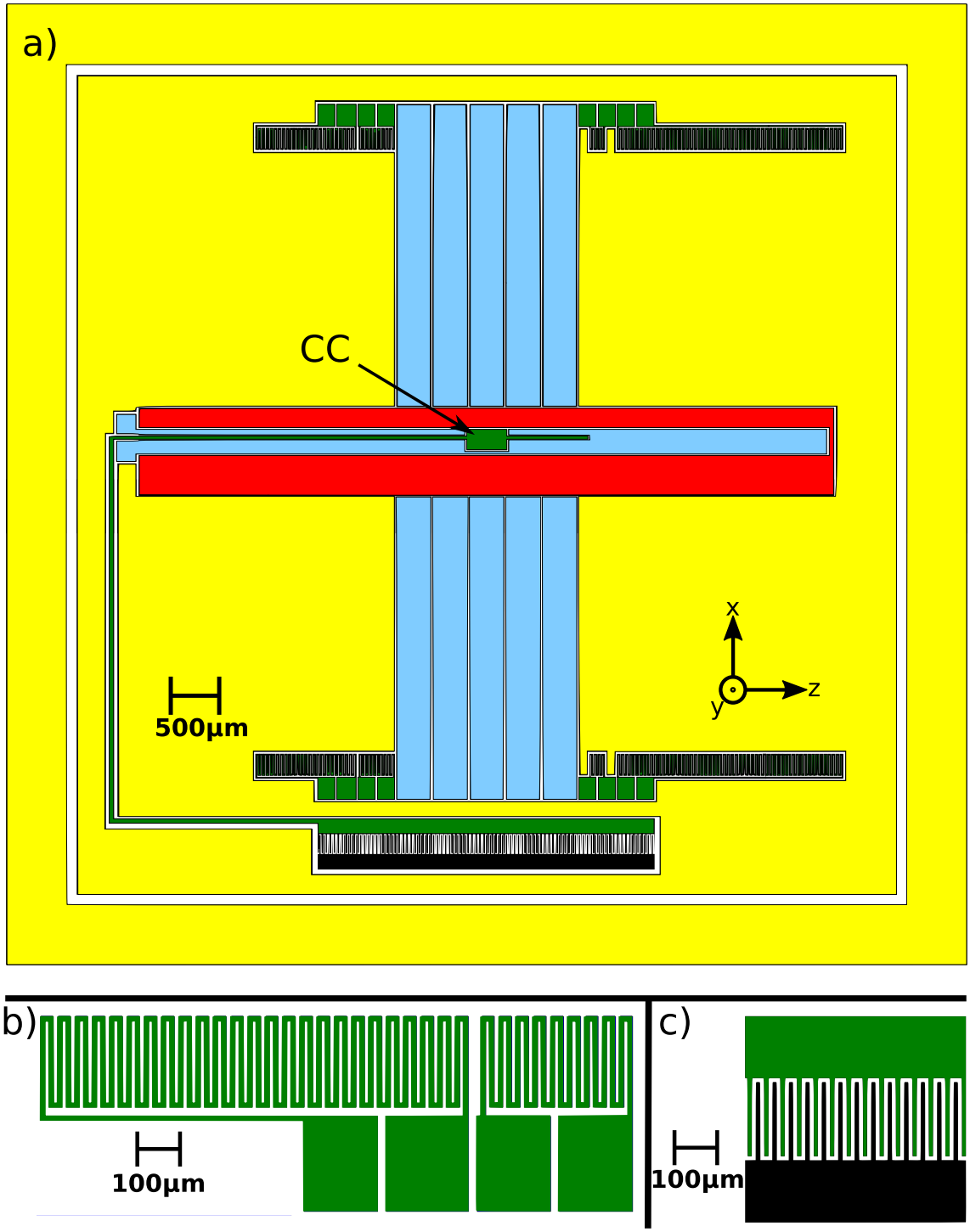

Figure 4.10: **a)** Layout of the one-meander design. The CC-electrode is used as the meander-electrode. The CC-electrode and the different meanders are shown in green. The red colored electrodes are connected to an RF-resonator, the blue ones are DC-electrodes and the yellow parts are electrically grounded. The lower part of the interdigitated finger electrodes is black. A zoom in on the CC-electrode is provided in figure 4.11. **b)** Zoom in on two meanders with their respective bonding pads. **c)** Zoom in on a part of the interdigitated finger electrode. The trace width of the meander and the width of each finger is $10\,\mu\mathrm{m}$. All electrode gaps in **b** and **c** are $10\,\mu\mathrm{m}$.

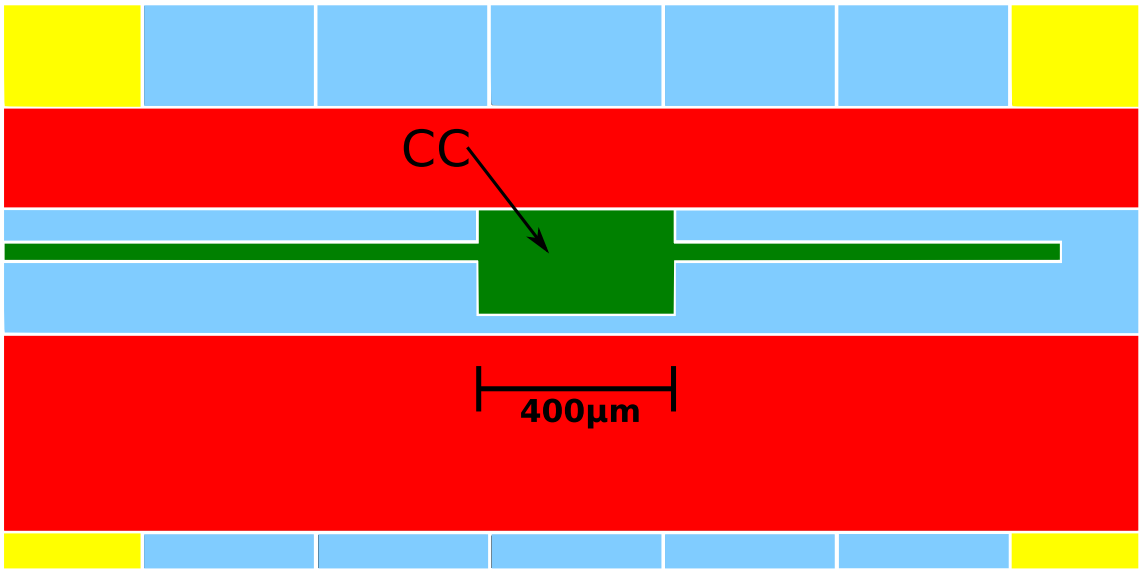

Figure 4.11: Zoom in on the CC-electrode (shown in green). The CC-electrode is connected to the meanders via the trace to the left side. The trace to the right side serves to reduce the asymmetry introduced by the trace on the left side. The red colored electrodes are connected to an RF-resonator, the blue ones are DC-electrodes and the yellow parts are electrically grounded. The gap size between the electrodes is $10\,\mu\mathrm{m}$.

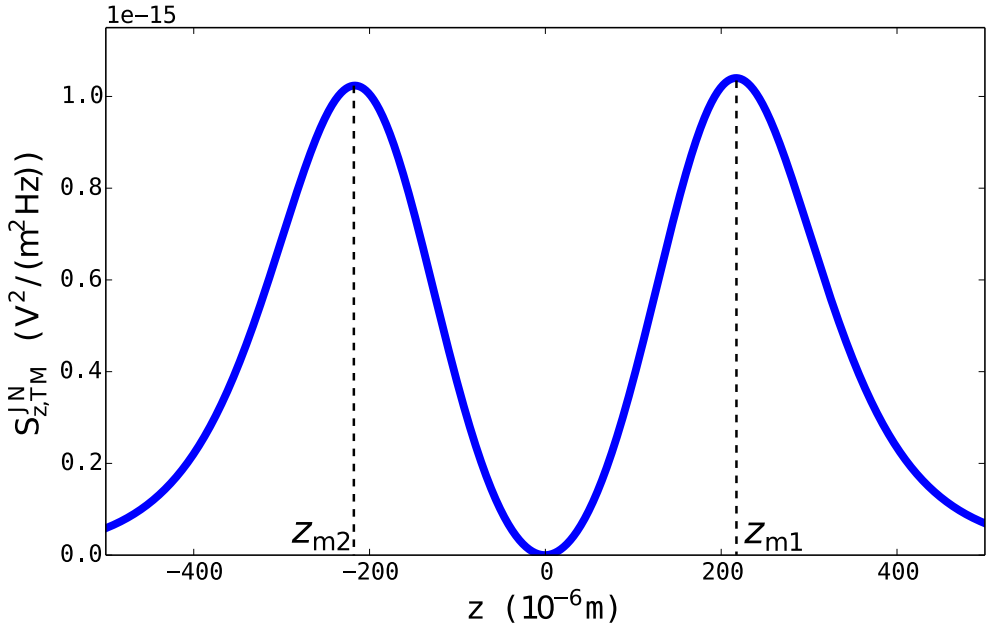

Figure 4.12: Johnson noise from the CC-electrode of the one-meander design for $T = 100\,\mathrm{K}$ and $R = 1\,\Omega$ as a function of the ion position along the z-axis of the trap. The Johnson noise is obtained with equation 4.1, where the characteristic distance was calculated using the *electrode package*.

l (µm)	R at 100 K (kΩ)	$S_{\mathrm{E_{max}}}$ ($\mathrm{V^2/(m^2Hz)}$)	$S_{\mathrm{E}}/S_{\mathrm{T_c}}$	Γ_{h} (phonons/s)
26840	70	7.3×10^{-11}	24	1.07×10^4
11670	30.5	3.18×10^{-11}	10	4.64×10^3
3990	10.4	1.09×10^{-11}	3.6	1.59×10^3
1790	1.69	4.88×10^{-12}	1.6	7.1×10^2

Table 4.3: Length l of the meanders integrated on the one-meander design, the corresponding resistance R, the electric field spectral noise density S resulting from Johnson noise and the corresponding heating rate Γ_{h}. Additionally, the relation between $S_{\mathrm{E}}/S_{\mathrm{T_c}}$ is shown, where $S_{\mathrm{T_c}} \approx 3 \times 10^{-12}\,\mathrm{V^2/(m^2Hz)}$ is the upper bound for the expected electric field noise at $T = T_{\mathrm{c}}$ calculated in section 4.4.1. The resistances are calculated by $R = \rho l/wd$, with the resistivity $\rho = 131(2)\,\mu\Omega\,\mathrm{m}$, the meander trace width $w = 10\,\mu\mathrm{m}$ and the thickness of the YBCO film $d = 50\,\mathrm{nm}$. The resistivity was determined by averaging over measurements of the resistance of three different meander structure at $T = 100\,\mathrm{K}$. An example of a resistance measurement is presented in section 6.1.1.

at $z_{\mathrm{m1}} = 217\,\mu\mathrm{m}$. The second maximum of the Johnson noise at $z_{\mathrm{m2}} = -217\,\mu\mathrm{m}$ has a slightly smaller magnitude $S_{\mathrm{E2}} = 0.98 S_{\mathrm{E1}}$ due to the asymmetric CC-electrode (see figure 4.12). Compared to the TM-electrode of the HTCYK1 design the characteristic distance is reduced by a factor of 6.5. Therefore, the maximum noise is increased by a factor of 42 independent from R and T.

The calculations in the previous section show that the RF-grounding of the meander-electrode depends on the meander-resistance R_{meander}; it is improving with decreasing R_{meander}. Consequently, R_{meander} should be as low as possible. The required R_{meander} to make Johnson noise dominant depends on the unknown heating rate of the other noise sources. Therefore several different meander lengths are placed on the trap chip. The different meanders have bonding pads in order to connect them to the trace of the CC-electrode by bonding wires. The different meander lengths together with the expected resistances and the expected heating rates are listed in table 4.3. These meanders are replicated on the upper part of the design to allow one to measure the resistance of the meander during the trap operation. At $T = 100\,\mathrm{K}$ the different meander sizes produce Johnson noise ranging from $1.6 S_{\mathrm{T_c}}$ to $24 S_{\mathrm{T_c}}$, where $S_{\mathrm{T_c}} \approx 3 \times 10^{-12}\,\mathrm{V^2/(m^2Hz)}$ is the upper bound for the expected electric field noise at $T = T_{\mathrm{c}}$ calculated in section 4.4.1.

The one-meander design makes it possible to reduce the required resistance significantly. Nevertheless, a RF-pickup $V_{\mathrm{12,RF}}$ might be present on the CC-electrode. Additional means may be used to reduce $V_{\mathrm{12,RF}}$ (see section 4.6). One of these means is to inject an additional RF signal via a capacitive coupling. The interdigitated electrodes at the bottom of the chip serve as a capacitor to inject this RF signal. The capacitance $C = 2.7\,\mathrm{pF}$ between the electrodes is calculated by [64]

$$C = pq\frac{4}{\pi a}\epsilon_{\mathrm{r}}\epsilon_0 \sum_{n=1}^{\infty} \frac{1}{2n-1} J_0^2\left(\frac{(2n-1)\pi s}{2a}\right), \tag{4.5}$$

where $p = 180\,\mu\mathrm{m}$ is the length of the overlapping fingers, $q = 3330\,\mu\mathrm{m}$ is the width of the whole structure, $a = w + s = 20\,\mu\mathrm{m}$ is the sum of the width $w = 10\,\mu\mathrm{m}$ of one finger and the spacing between two fingers $s = 10\,\mu\mathrm{m}$ and J_0 is the zeroth Bessel function of

the first kind.

4.5.2 Two-meander design

The two-meander design uses meander-electrodes with reduced characteristic distance compared to the HTCYK1 design (like the one-meander design). Additionally, this second design takes the effects of the RF-pickup into account. The meander-electrodes described in the following are designed in a way to overlap the minimum of the electric field resulting from the RF-pickup with the trapping position of the ion.

As shown in figure 4.13, the central electrode is split into three parts. The C1- and the C2-electrode are symmetric to each other with respect to the ion position. Both electrodes have long traces going to meanders on the bottom part of the trap chip. The meanders on the left and on the right side are identical. In this way the symmetry of the C1- and the C2-electrode is not broken if a meander is connected to each electrode. The meander is connected to the electrode by a bonding wire from the bonding pad of the meander to the bonding pad of the trace to the electrode.

The RF-pickup on the C1- and the C2-electrode are expected to be identical, both in phase and in amplitude, because of the symmetry between the C1-, the C2- and the RF-electrode. Consequently, there exists a point between the two electrodes where the electric field resulting from the RF-pickup, vanishes. The size and the position of the electrodes are chosen in order to overlap this point with the trapping position of the ion. In this way the RF-pickup does not prevent from compensating the micromotion.

The Johnson noise from the two electrodes is totally uncorrelated, because it is produced by two different meanders. Therefore, the spectral electric field noise density adds up linearly [17]. In sum it is $S_{\mathrm{E}} = 4.25 \times 10^{-16}\,\mathrm{V^2/m^2Hz}$ for $T = 100\,\mathrm{K}$ and $R = 1\,\Omega$, which is about a half of the value in the one-meander design. The different meander lengths and the resulting expected heating rates are shown in table 4.4. At $T = 100\,\mathrm{K}$ the different meander sizes produce Johnson noise ranging from $1.9 S_{\mathrm{T_c}}$ to $13 S_{\mathrm{T_c}}$, where $S_{\mathrm{T_c}} \approx 3 \times 10^{-12}\,\mathrm{V^2/(m^2Hz)}$ is the upper bound for the expected electric field noise at $T = T_{\mathrm{c}}$ calculated in section 4.4.1.

First heating rate measurements in a two-meander design trap were already performed and the results are discussed in section 6.4.2.

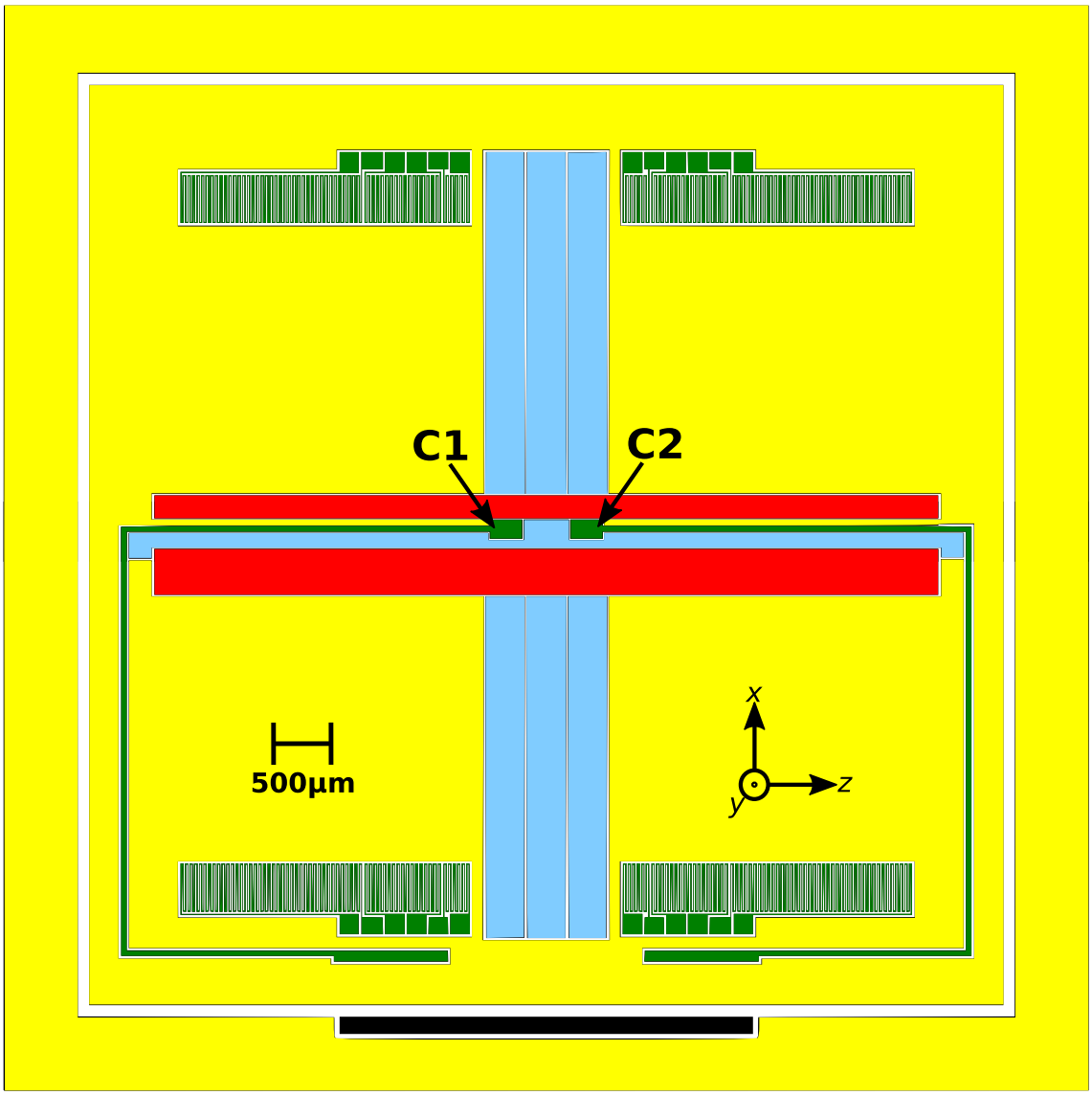

Figure 4.13: Layout of the two-meander design. The meander-electrodes C1 and C2-elctrode and the different meanders are shown in green. The red colored electrodes are connected to an RF-resonator, the blue ones are DC-electrodes and the yellow parts are electrically grounded. The black electrode on the bottom provides a possiblity to connect the C1- and the C2-electrode. The gaps between the electrodes are $10\,\mu\mathrm{m}$. The meanders have the same width as in the one-meander design ($10\,\mu\mathrm{m}$). Only their length differs from the one-meander design.

l (µm)	R at 100 K (kΩ)	S_E ($\mathrm{V^2/(m^2Hz)}$)	$S_\mathrm{E}/S_{\mathrm{T_c}}$	Γ_h (phonons/s)
35840	94	3.99×10^{-11}	13	5.82×10^3
14960	39.2	1.67×10^{-11}	5.6	2.43×10^3
5190	13.6	5.78×10^{-12}	1.9	8.4×10^2

Table 4.4: Length l of the meanders integrated on the two-meander design, the corresponding resistance R, the electric field spectral noise density S_E resulting from Johnson noise and the corresponding heating rate Γ_h. Additionally, the relation between $S_\mathrm{E}/S_{\mathrm{T_c}}$ is shown, where $S_{\mathrm{T_c}} \approx 3 \times 10^{-12}\,\mathrm{V^2/(m^2Hz)}$ is the upper bound for the expected electric field noise at $T = T_\mathrm{c}$ calculated in section 4.4.1. The resistances are calculated by $R = \rho l/wd$, with the resistivity $\rho = 131(2)\,\mu\Omega\,\mathrm{m}$, the meander trace width $w = 10\,\mu\mathrm{m}$ and the thickness of the YBCO film $d = 50\,\mathrm{nm}$. S and Γ_h are the sum of the noise from 2 identical meanders, one connected to the C1-electrode and one to the C2-electrode.

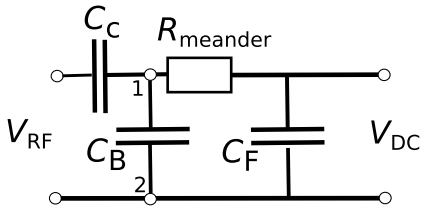

Figure 4.14: Schematic electronic circuit of the improved RF-grounding of the meander-electrode by a bypass capacitor C_B. On the left side is the RF-voltage V_RF applied to the RF-electrode. C_C is the capacitive coupling between the RF-electrode and the DC-electrode (point 1), C_F is the last capacitance to ground (point 2) of the filter components and R_meander is the resistance between them. As explained in section 4.4.3 the other filter components between C_F and the DC-source V_DC do not affect the RF-grounding of the DC-electrode and therefore they are not shown.

4.6 Additional means to reduce the RF-pickup voltage

4.6.1 Bypass capacitor

The first possible means is to connect a bypass capacitor C_B to ground to the connection between the meander-electrode and the meander. The resulting electric circuit can be seen in figure 4.14. As C_B is parallel to R_meander the overall impedance from point 1 to ground (point 2) is reduced. This reduces the RF-pickup $V_\mathrm{12,RF}$:

$$V_\mathrm{12,RF} \approx \frac{R_\mathrm{meander}}{R_\mathrm{meander}(1+\frac{C_\mathrm{B}}{C_\mathrm{C}})+Z_{C_\mathrm{C}}} \cdot V_\mathrm{RF}, \tag{4.6}$$

where the impedance of C_F was neglected as in equation (4.4). Compared to that equation it is apparent that the reduction of $V_\mathrm{12,RF}$ depends on the ratio between C_B and C_C. Consequently, C_B should be chosen as high as possible.

The drawback of this method is that C_B reduces the effective real resistance R_eff connected to the electrode. This reduces the Johnson noise as $S_\mathrm{JN} \propto R_\mathrm{eff}$ (see section 3.1). R_eff is given by

$$R_\mathrm{eff} = \frac{R_\mathrm{meander}}{1+(R_\mathrm{meander}\omega C_\mathrm{B})^2}. \tag{4.7}$$

It has to be noted that in this equation ω is the frequency at which the Johnson noise is measured, i.e. the axial secular frequency ω_z of the ion in the trap. In contrast, in equation (4.6) the drive radio-frequency ω_RF has to be used to calculate Z_{C_C}. This makes a significant difference as typically $\omega_\mathrm{RF} \approx 20\omega_z$.

An optimised value of C_B cannot be given before the first measurements with a trap. It depends on the unknown value of C_C (it can only be approximated like in appendix A), the required R_eff and the maximum reasonable pickup voltage $V_\mathrm{12,RF}$.

How different values of C_B affect the Johnson noise and the RF-grounding is shown in the plots of figure 4.15. For them the following values are taken: $\omega_\mathrm{sec} = 2\pi \cdot 1\,\mathrm{MHz}$, $\omega_\mathrm{RF} = 2\pi \cdot 19\,\mathrm{MHz}$ and $C_\mathrm{C} = 0.1\,\mathrm{pF}$. The plotted range of R_meander covers the values of the smallest meander on the two-meander design within the relevant temperature for the experiment (up to $T \approx 110\,\mathrm{K}$).

Plot a) of figure 4.15 results from equation (4.6) and shows that the relative RF-pickup $V_\mathrm{12,RF}/V_\mathrm{RF}$ decreases with increasing C_B. In plot b) it can be seen that $C_\mathrm{B} = 50\,\mathrm{pF}$ results in an R_eff that decreases with increasing R_meander. As it is planned to measure the temperature dependence of the heating rate, the latter case must be avoided. The increase of R_meander for increasing temperature would lead to a reduction of R_eff and the resulting Johnson noise would decrease with increasing temperature. This would make it complicated to verify that the heating rate is dominated by Johnson-noise above T_c.

The two plots show that $C_\mathrm{B} = 10\,\mathrm{pF}$ could be a reasonable value, because $V_\mathrm{12,RF}/V_\mathrm{RF}$ is reduced significantly while R_eff does not decrease within the range of R_meander.

Finally, it should be mentioned that the meander electrode has already a capacitive coupling to ground on the trap chip. For geometric reasons, this coupling is smaller than the coupling between the interdigitated fingers on the one-meander design (see figure 4.10) and larger than the coupling between the TM-electrode and the RF-electrode which

is approximated in appendix A. Therefore a bypass capacitor with $0.03\,\mathrm{pF} < C_\mathrm{B} < 2.7\,\mathrm{pF}$ is always present in the system.

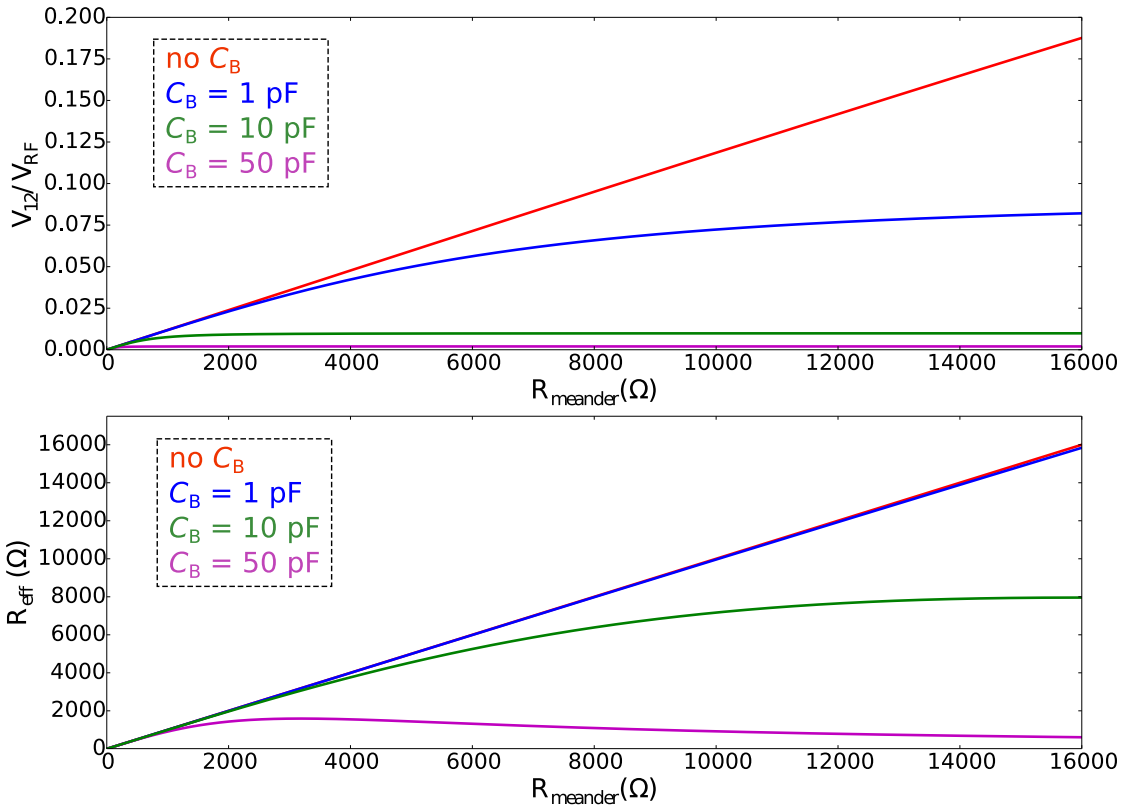

Figure 4.15: Simulations of the effect of different bypass capacitors C_B: in blue $1\,\mathrm{pF}$, in green $10\,\mathrm{pF}$, in magenta $50\,\mathrm{pF}$. For comparison red shows the calculation without C_B. In both plots R_meander is given on the horizontal axis. The range of the resistance covers the values of the smallest meander on the two-meander design within the relevant temperature for the experiment (up to $110\,\mathrm{K}$). a) The relative RF-pickup $V_{12,\mathrm{RF}}/V_\mathrm{RF}$ as a function of R_meander. It decreases for higher values of C_B. Additionally, it can be seen that for $C_\mathrm{B} = 10\,\mathrm{pF}$ and for $50\,\mathrm{pF}$ it saturates after a certain resistance. b) The effective real resistance R_eff depending on R_meander. The blue curve shows that for low values of C_B the effect on R_eff is negligible. From the magenta curve it can be seen that a too high value of C_B results in an R_eff that decreases with increasing meander resistance.

4.6.2 Compensating the RF-pickup using a second RF signal

Compensating the RF-pickup by an external RF-source was already demonstrated in [63]. In our setup, the RF signal has to be injected between the meander and the meander-electrode as depicted in figure 4.16. The injection can be realised by a capacitive coupling. The capacitive coupling C_RF acts additionally as a bypass capacitor. Consequently, the

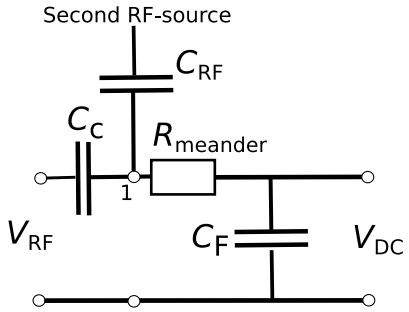

Figure 4.16: Schematic electronic circuit of the capacitive coupling from the RF-electrode to the meander-electrode with a second RF signal inserted via C_{RF} to compensate the pickup-voltage on the meander-electrode (point 1).

reduction of R_{eff} has to be considered when one chooses C_{RF}. The amplitude of the additional RF signal has to match the one of the RF-pickup and the phase difference has to be -180° in order to fully compensate the RF-pickup. The appropriate amplitude and phase have to be determined by minimizing the micromotion of the ion.

Chapter 5

Experimental setup

The experiments described in this thesis are carried out using a cryogenic setup, which was mainly built by Michael Niedermayr and is described in his PhD thesis [29]. After briefly motivating the use of cryogenic ion trap setups, the existing setup is described in section 5.1. The operation temperature of the cryostat is $T \approx 10\,\mathrm{K}$. For this project, the YBCO traps have to be operated in the temperature range (10-120) K. To achieve these temperatures in the existing cryostat setup, a variable-temperature trap mount was built and integrated into the setup. As the filterboard and the RF-resonator are permanently fixed to the trap mount, they had to be rebuilt for the new mount and they are described in section 5.2. The design of the variable-temperature trap mount and its measured characteristics are presented in section 5.3. Additionally, a 4-wire resistance measurement was integrated in the setup in order to measure the meander resistance $R(T)$ during the trap operation. It is shown in section 5.4.

5.1 Cryogenic environment

The following section provides information about the experimental setup and is based on a more detailed description in [29].

5.1.1 Advantages of operating ion traps at cryogenic temperatures

Ion traps for quantum information processing have to be operated in ultra high vacuum with a pressure p around $10^{-11}\,\mathrm{mbar}$ to prevent collisions of background molecules with the ion. Such collisions can lead to ion loss or chemical reactions, both necessitating reloading of ions. Cryogenic temperatures make it possible to reach extremely high vacuum ($p < 10^{-12}\,\mathrm{mbar}$), because of the cryopumping effect. At $T = 10\,\mathrm{K}$, all molecules apart from noble gases and hydrogen have a saturation pressure below $10^{-12}\,\mathrm{mbar}$ [65]. If a vacuum pump is used for evacuating the system to a medium vacuum ($< 10^{-5}\,\mathrm{mbar}$) before the cryostat is turned on, then the amount of hydrogen and helium in the chamber is sufficiently low that most of these residual molecules stick to the cold surface due to physical adsorption [65]. This allows turnaround times of 2 days, i.e. changing from one operated trap to another by heating up the system to room temperature, breaking the

vacuum, changing the trap, pumping the system and cooling it down. In contrast, room temperature setups usually have to be baked for at least a week to reach sufficiently low pressures.

Another advantage of operating ion traps at cryogenic temperatures is that the electric field noise is reduced significantly compared to room-temperature setups [17]. Besides that, cryogenic temperatures allow the usage of materials that have too high outgassing rates at room temperature. At room temperature these prevent reaching ultra high vacuum.

Finally, the high conductivity of copper at cryogenic temperatures offers the possibility to build up a strong electromagnetic shield around the trap [66].

5.1.2 Existing setup

For cooling down the ion trap setup a closed-cycle Gifford-McMahon cryostat is connected to the vacuum chamber. It is anchored to the ceiling of the room and the vacuum chamber is mounted on an optical table. The cryostat consists of two cooling stages, a $50\,\mathrm{K}$ and a $10\,\mathrm{K}$ stage, and reaches temperatures below $10\,\mathrm{K}$. A drawback of this type of cryostat is that it produces large vibrations ($\approx 10\,\mu\mathrm{m}$ amplitude). This can cause oscillations of the ion with respect to the laser beams, which leads to intensity fluctuations at the ion and reduces the fidelity of quantum gates [30]. To provide vibration isolation of the vacuum chamber from the cryostat and at the same time maintain high thermal contact, helium is used as a buffer gas. A GMX-20[1] adapter, which has a diameter $10\,\mathrm{mm}$ larger than the cold head of the cryostat, is connected to the cryostat by a rubber bellow. The closed volume between the GMX-20 adapter and the cold head is filled with helium. In this way the residual vibrations of the vacuum chamber caused by the cryostat are reduced to $(200 - 300)\,\mathrm{nm}$ [29].

The GMX-20 adapter is connected to a CF160 full nipple and together they form the vacuum chamber. A cross section of the whole vacuum chamber is shown in figure 5.1. In order to thermally isolate the ion trap from thermal radiation of the vacuum chamber, it is surrounded by $50\,\mathrm{K}$ and $10\,\mathrm{K}$ copper shields. The two shields are thermally anchored to the $50\,\mathrm{K}$ and $10\,\mathrm{K}$ cooling stages of the cryostat. The vacuum pump station is connected to the chamber by a valve and electrical connections are integrated by two BNC feedthroughs and a D-sub feedthrough. The cables from the feedthroughs to the trap are thermally anchored to the cold stages to minimize the heat conduction to the trap.

The trap itself is installed on a trap mount described in section 5.3. It is situated in the octagon at the bottom of the vacuum chamber and screwed to two copper rods, which ensure good thermal conductivity to the $10\,\mathrm{K}$ stage. The electronic connections to the mount are provided by pogo-pins[2]. This allows the trap mount to be removed easily. To access the trap mount, the whole cryostat is tilted and the vacuum chamber is opened using the bottom flange of the octagon.

As depicted in figure 5.2, a ALVASOURCE 3-Ca-150-C oven is connected to one of the ports of the octagon. It is used to produce a beam of neutral Ca-atoms at the trapping location. The other BK7 viewports provide optical access for the required lasers, which

[1] Advanced Research Systems, GMX-20
[2] Mill-Max, 0929-0-15-20-75-14-11-0.

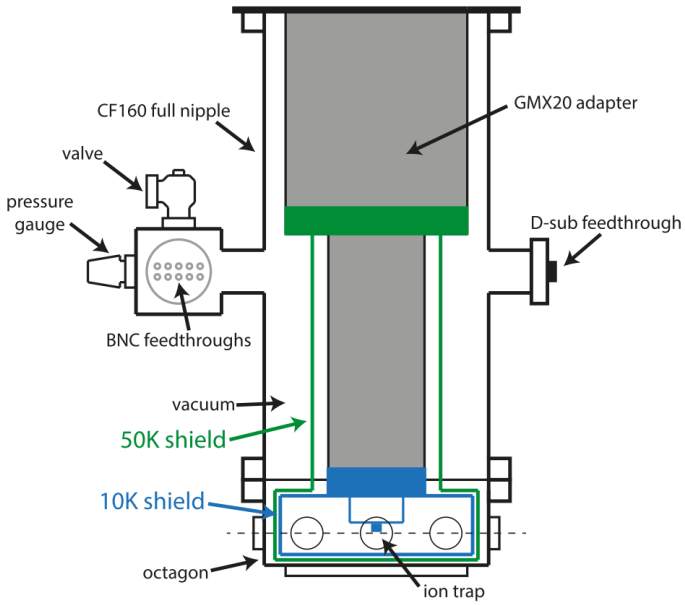

Figure 5.1: Schematic cross section of the croystat and vacuum setup, taken from [29]. The vacuum chamber consists of a CF160 full nipple, a CF160 octagon at the bottom and the GMX20 adapter which surrounds the two cooling stages of the cryostat. The two cooling stages are connected to 50 K and 10 K copper shields providing the thermal isolation and electromagnetic shielding of the ion trap. Two BNC feedthroughs and a D-sub feedthrough provide the electrical connections for the trap and the temperature sensors. A vacuum pump station is connected to the chamber via the valve. Figure courtesy of Michael Niedermayr.

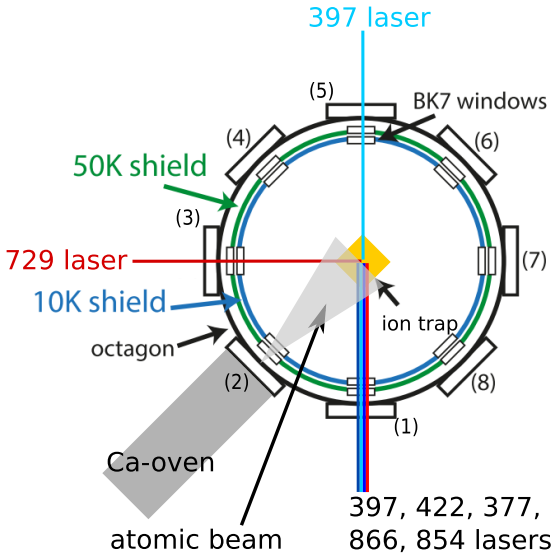

Figure 5.2: Schematic cross section of the octagon. Laser access is provided by the viewports (1),(3) and (5) and BK7 windows integrated in the 50 K and 10 K shields. An ALVASOURCE 3-Ca-150-C oven is attached to port (2) in order to produce a beam of neutral Ca-atoms at the trapping location. Additional optical access is provided by the remaining viewports, which are not used at the moment. Magnetic coils are attached to the viewports (1),(3),(5) and (7) to produce a homogeneous magnetic field at the trapping location.

have to be overlapped at the trapping position. For more information about the laser setup it is referred to [29, chapter 4.3].

The bottom flange of the octagon consists of another BK7 viewport, which together with an objective allows one to collect the fluorescence of the ion. The fluorescence light is then split up by a 50/50 beamsplitter. One part is sent to a CCD camera[3] and the other to a photomultiplier tube[4].

Finally, two pairs of magnetic coils are attached to four viewports and provide a homogeneous magnetic field of several gauss at the ion trap. This splits up the Zeeman sublevels in order to resolve the transitions for optical pumping, sideband cooling, and qubit addressing as described in section 2.4.

5.2 Filterboard and RF-resonator

Technical noise and electromagnetic pickup can lead to voltage noise on the electrodes (see section 3.1). This results in motional heating of the ion. In order to minimize this noise, appropriate filters have to be integrated in the electronic circuits. For that reason low-pass filters are implemented in the DC lines installed on printed circuit boards (PCBs) close to the trap. The PCBs are part of the trap mount described in the next section and shown in figure 5.4.

For the DC-electrodes RC low-pass filters with a cut-off frequency of $17\,\mathrm{kHz}$ are installed on these PCBs. Moreover, pi filters with a cut-off frequency of $4.8\,\mathrm{kHz}$ are added outside of the vacuum chamber. A schematic is shown in figure 4.9 and detailed informations about the used components can be found in [29, section 4.2.3].

An RF-resonator is used to amplify the RF-voltage provided by a function generator. The resonator makes it possible to operate the trap with an RF input power below $100\,\mathrm{mW}$. Beside that, it serves as a filter for all frequencies outside a small range around the resonance frequency. The resonator used in this thesis is built similarly to the one described in [29, 67]. A schematic of the electronic circuit is shown in figure 5.3. The RLC resonator consists of several elements. A homebuilt copper coil provides the inductance L. The capacitance C is mainly given by the capacitance between the RF-electrodes of the trap and electrical ground. A matching network is used to minimize the reflections of the incoming signal. In order to measure a fraction of the RF-voltage on the trap, a capacitive divider is part of the circuit. These components are all installed on a PCB close to the trap inside the cryostat. Their disposition can be seen on the photo in figure 5.4.

The resonator has two important properties: the intrinsic quality factor Q_{int} and the resonance frequency f_0. f_0 is given by

$$f_0 = \frac{1}{2\pi\sqrt{LC}} \tag{5.1}$$

and Q_{int} is defined by

$$Q_{\mathrm{int}} = \frac{1}{R}\sqrt{\frac{L}{C}}. \tag{5.2}$$

[3] Andor, iXon+ A-DU897-DCS-BBB
[4] Hamamatsu, H7360-02

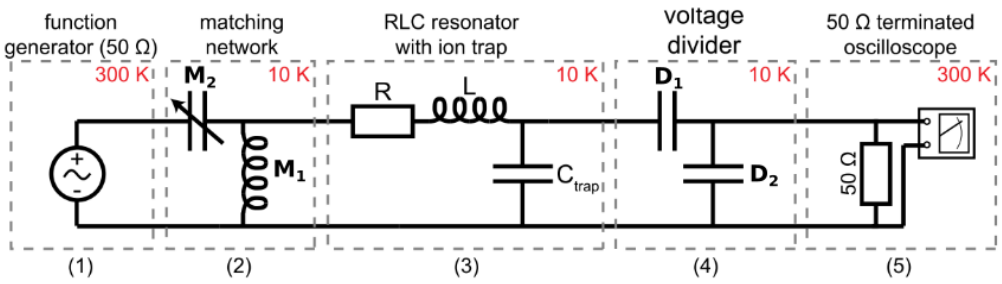

Figure 5.3: Schematic of the RF-resonator circuit used to drive the trap. The signal of the function generator (1) is stepped up by the RLC resonator (3), where the trap itself is part of the capacitance C. The inductance L is provided by a homebuilt copper coil. The resistance R is mainly produced by the resistance of the coil. In order to minimize the reflection of the incoming signal, a matching network (2) is installed before the resonator. It consists of a variable capacitor M_2 and an additional copper coil M_1. The two capacitors C_1 and C_2 are used as a voltage divider (4) and are called capacitive divider. They allow to measure a fraction of the RF-voltage on the trap using e.g. an oscilloscope (5) or an RF spectrum analyser. The function generator and the oscilloscope are outside of the vacuum chamber ($T = 300\,\mathrm{K}$). The other parts are installed on the trap mount and are thermally anchored to the 10K-stage of the cryostat. Figure courtesy of Michael Niedermayr [29].

f_0 (MHz)	Q_{int}	L(µH)	C(pF)	M_1(pF)	M_2(µH)	C_1(pF)	C_2(pF)	$R(\Omega)$
17.505(1)	1514(10)	6.5(1)	13(2)	12-100	0.17(1)	2.5	1000	0.47(5)

Table 5.1: Component list of the RLC resonator including the matching network and the capacitive divider at $T \approx 10\,\mathrm{K}$. f_0 is the resonance frequency of the newly built resonator together with a mounted YBCO trap. The capacitance of C_1,C_2 and M_2 are taken from their datasheets. The inductances of the coils were measured with a Q-Meter[5] before their installation to the PCB. f_0 and Δf are measured with a frequency analyser[6]. The capacitance of the resonator C is then calculated using equation (5.1) and Q_{int} is given by equation (5.3). Finally, R is obtained with equation (5.2).

Q_{int} can be obtained by measuring the resonance frequency f_0 and the $-3\,\mathrm{dB}$ full-width voltage gain bandwidth of the resonance Δf. In a measurement, the full electronic circuit has to be taken into account, i.e. the matching network influences the measured value Q_{meas}. It was shown by [67] that

$$\begin{aligned} Q_{\mathrm{int}} &= 2Q_{\mathrm{meas}}, \\ \text{with} \quad Q_{\mathrm{meas}} &= \frac{f_0}{\Delta f}. \end{aligned} \tag{5.3}$$

The values of the different components of the resonator are given in table 5.1. The measured resonance frequency is $f_0 = 17.505(1)\,\mathrm{MHz}$. The quality factor is $Q_{\mathrm{int}} = 1514(10)$. It is higher than the $Q = 1200$ reported in [29], which is most likely due to the fact that the trap electrodes have no resistance in the superconducting state (in [29] the trap electrodes are made of gold).

[5] HP 4342A Q-Meter
[6] VIA BRAVO II

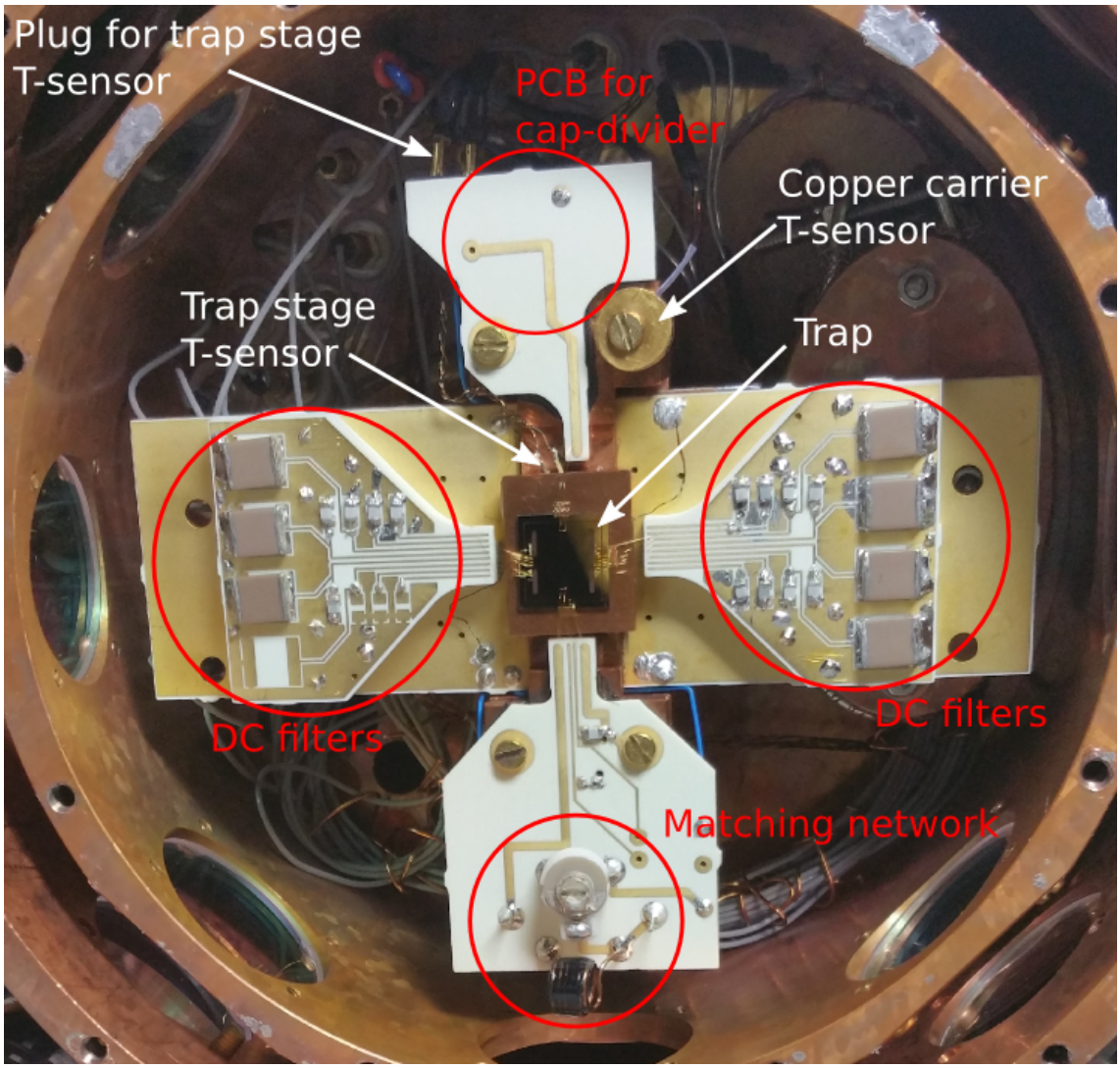

Figure 5.4: Trap installed in the cryostat. The trap is glued onto the copper plate forming the trap stage in the center of the picture. The trap stage is part of the trap mount described in section 5.3 and is surrounded by PCBs. The trap is electrically connected to the RF-resonator on the PCB at the bottom and to the DC lines on the PCBs on the left and on the right side of the trap with bonding wires. On the PCBs containing the DC lines, half of the capacitors of the DC filters are visible. The other half together with the resistors are on the back side of the PCB. On the PCB holding the matching network, a variable capacitor and a small homebuilt copper coil are installed. The large coil for the RF-resonator is soldered to the back side of the matching network PCB. The capacitive divider is also soldered on the back side. The trap stage temperature sensor is connected by phosphor bronze wires with a plug. Another temperature sensor is screwed to the copper carrier that forms the rigid mount for the PCBs and the trap stage. The two copper cylinders with optical windows around the trap mount are the 50 K and 10 K shields.

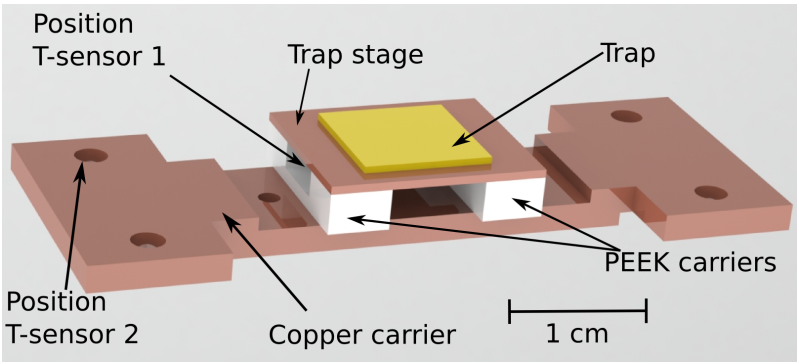

Figure 5.5: Schematic of the variable-temperature trap mount. The trap is glued to a $0.6\,\mathrm{mm}$ thin copper piece called trap stage. The trap stage is thermally decoupled from the copper carrier by two U-formed $3\,\mathrm{mm}$ thick PEEK carriers. To heat up the trap locally 6 resistors are glued to the back side of the trap stage (see figure 5.6). In addition a temperature sensor (T-sensor 1) is glue to measure its temperature.d to the trap stage to control the trap temperature. A second sensor (T-sensor 2) is screwed to the copper carrier.

To characterise the resonator further, the temperature dependence of Q was measured and the result is shown in figure 6.2. Q is decreasing with increasing temperature, dominated by the resistance increase of the copper coil. The temperature dependence has consequences for the design of the variable-temperature trap mount and is discussed in the next section.

5.3 Variable-temperature trap mount

For this thesis, we need to be able to adjust the temperature of the trap, so that the ion can be used to probe the superconducting transition. The new trap mount has to fulfil several criteria: First, the trap has to be thermally decoupled from the cold stage. Second, a local heater and a temperature sensor have to be installed close to the trap. Thirdly, the temperature of the filterboard and the resonator should be affected as little as possible by the local heater in order to minimise possible effects on the electric field noise. The DC-filter characteristics can vary with temperature, because they depend on the capacitance and the resistance of the installed components on the filterboard.

The temperature of the resonator coil is even more critical. If it is heated up from $10\,\mathrm{K}$ to $100\,\mathrm{K}$, the Q of the resonator is reduced by a factor of 3 (see figure 6.2). As the gain of the resonator is proportional to $\sqrt{Q}$ this would cause the need for a higher input power to drive the trap. The higher input power may increase the technical noise level, which is also less filtered in a resonator with reduced Q.

The new trap mount fulfils these criteria and it is presented in this section.

5.3.1 Modifications to the existing setup

A schematic of the new trap mount is shown in figure 5.5. The trap is glued on a $0.6\,\mathrm{mm}$ thin copper piece forming the trap stage. On the backside of the trap stage six $R = 470\,\Omega$

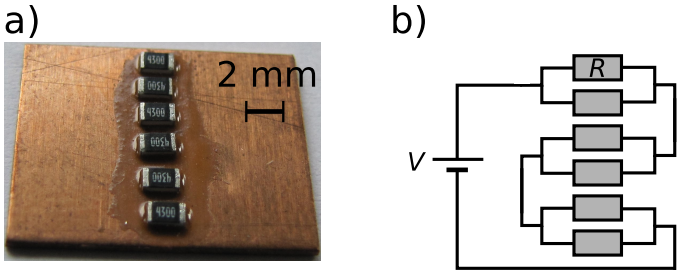

Figure 5.6: a) $R = 470\,\Omega$ resistors (Yageo Europe RC1206) glued to the trap stage with Epotek H74. **b)** Electronic connection of the resistors leading to an overall resistance of $705\,\Omega$ connected to a power supply to apply a voltage V for heating the trap stage.

resistors[7] are glued with Epotek H74 epoxy[8]. They are connected with solder to form 3 pairs of two parallel resistors each (see figure 5.6). These pairs are connected in series resulting in a total resistance of $705\,\Omega$. They are connected to the PCB by phosphor bronze wires[9] in order to minimise the thermal conductivity between the PCB and the trap stage. According to the specifications, the wires have a thermal conductivity which is 100 times smaller compared to common copper wires of the same diameter.

Two U-formed $3\,\mathrm{mm}$ thick polyether ether ketone (PEEK) carriers are used to thermally decouple the trap stage from the copper carrier and provide rigid mounting of the trap stage. They are glued with H74 to the trap stage and the copper carrier. In the first tests, the adhesion did not withstand the cooling cycle inside the cryostat due to the mismatch of the temperature expansion coefficients of copper and PEEK[10]. A solution for that is obtained in the following way: PEEK stripes of approximately 1 mm width and 0.125 mm thickness are positioned between the copper and the PEEK before H74 is added. This enables one to apply a thicker layer of H74 in a controlled way. The larger thickness of adhesive leads to a reduced stress at low temperatures.

A temperature sensor[11] is glued to the trap stage with H74. In order to be able to take the whole mount out of the cryostat, the electrical connections of the temperatures sensor must be removable. A self-made plug is thus added and connected to the sensor by phosphor-bronze wires. The plug consists of a pair of Millmax connectors[12] that are fixed in a $4\,\mathrm{mm}$ x $4\,\mathrm{mm}$ x $6\,\mathrm{mm}$ big piece of PEEK that is glued to the bottom side of the cap-divider PCB. The plug and the wire connections can be seen in figure 5.4. It is impossible to avoid that the sensor and its electronic connection are placed very close to the electrical lines carrying the RF-signal. Consequently, a typical trap drive RF-voltage of $170\,\mathrm{V}$ causes a pickup on the sensor's connection line leading to an RF current through the temperature sensor diode. The temperature is determined by measuring the resistance of the diode. As the resistance depends on the current through the diode, the RF-pickup can perturb the temperature measurement. The wires are twisted to minimize the pickup.

[7] Yageo Europe RC1206
[8] EPO-TEK H74 cured at $150\,^\circ\,\mathrm{C}$ for approx. $10\,\mathrm{min}$
[9] $1\,\mathrm{cm}$ Lakeshore Phosphor Bronze 36 AWG
[10] in the range of 50-300 K: $\alpha_{\mathrm{Cu}} \approx (13-17)\cdot 10^{-6}\,\mathrm{K}^{-1}$ and $\alpha_{\mathrm{PEEK}} \approx (25-50)\cdot 10^{-6}\,\mathrm{K}^{-1}$ [68, 69]
[11] Lakeshore DT-670C-SD: Silicon Diode with $32\,\mathrm{mK}$ precision and $1\,\mathrm{K}$ tolerance band for $T < 305\,\mathrm{K}$
[12] Millmax 0672

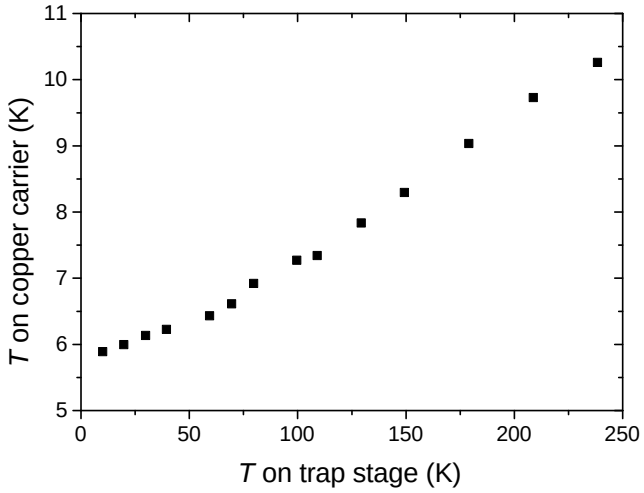

Figure 5.7: Temperature of the copper carrier versus the temperature of the trap stage during local heating of the trap stage. The trap stage was heated from $10\,\mathrm{K}$ to $238\,\mathrm{K}$, while the copper carrier temperature change only from $5.9\,\mathrm{K}$ to $10.3\,\mathrm{K}$.

However, an error of up to $20\,\mathrm{K}$ was observed in the measured temperature. For that reason a $1.5\,\mu\mathrm{F}$ capacitor[13] is soldered to the temperature sensor plug to provide a short circuit for RF-signals between the two connections. In this way the RF induced error of the temperature measurement is reduced to less than $0.3\,\mathrm{K}$.

The second temperature sensor[14] is screwed onto the copper carrier. As the PCB boards with the filters and the resonator have a good thermal connection to the copper carrier, the sensor gives an estimate of their temperature.

5.3.2 Performance of the thermal decoupling

After cooling down the cryostat, the local heater is used to increase the temperature of the trap stage. To measure the insulation between the copper carrier and the trap stage, the trap stage was heated up to $238\,\mathrm{K}$. At the same time the temperature of the copper carrier was increased by less than $5\,\mathrm{K}$ (see figure 5.7). A measurement of the resonator Q versus the temperature of the trap stage is discussed in section 6.1.2 and shows that the Q of the resonator is hardly affected by the local heating of the trap stage.

In figure 5.8, it can be seen that less than $160\,\mathrm{mW}$ are needed to reach $120\,\mathrm{K}$, which is the maximum temperature considered in this project.

These two results show that the trap stage is well thermally decoupled from the rest of the setup including the copper carrier and the PCBs. Therefore influences on the heating rate of the trap from the surrounding setup can be excluded while the temperature of the trap can be adjusted.

[13] KEMET T350A

[14] Lakeshore DT-670B-Cu: Silicon Diode with $32\,\mathrm{mK}$ precision and $0.5\,\mathrm{K}$ tolerance band for $T < 305\,\mathrm{K}$

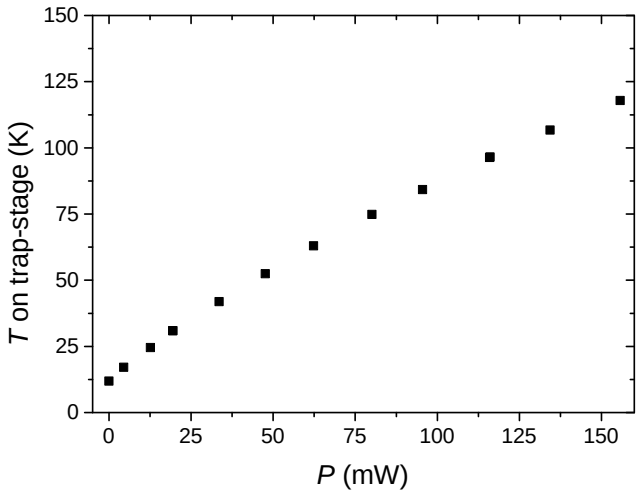

Figure 5.8: Temperature of the trap stage versus the power P dissipated in the local heater. The power $P = IV$ was obtained by measuring the current I and the voltage V outside of the vacuum chamber. The resistance of the wires connecting the power source with the local heater is around $30\,\Omega$ which is much smaller than the resistance $R \approx 0.7\,\mathrm{k}\Omega$ of the local heater. Consequently, the actually dissipated power at the trap stage is a few percent smaller than the measured values.

5.3.3 Trap installation

The process described here was fully carried out in our cleanroom[15]. Humidity can degrade the superconducting properties of YBCO. In order to protect the chips from humidity, they are stored in a desiccator, which is constantly evacuated by a membrane pump and kept dry by silica gel. Before the installation of a trap chip in the experiment, the protective photoresist covering the trap chip (see section 4.2.2) is removed by 5 minutes ultrasonic bath of acetone and additional 5 minutes in a ultrasonic bath of methanol. It is then glued to the trap stage with varnish VGE 7031[16]. We have chosen varnish as the adhesive, because it can be removed by an ultrasonic bath of acetone and an additional ultrasonic bath of methanol. This enables removing the trap without damage and to reuse it later. However, according to the specifications it consists of (30-60) % ethyl alcohol that evaporates while it is cured. Consequently, the adhesive looses a lot of weight leading to a bad thermal contact between the trap stage and the trap that is further discussed in section 6.2.1. Additionally, the mismatch of the thermal expansion coefficients of sapphire (the trap substrate) and copper causes a degradation of the adhesion during cooling cycles. Until now the adhesion of 2 out of 5 installed traps did not withstand several cooling cycles. Therefore the adhesive has to be considered as too fragile for a reliable trap installation. It is currently investigated if the adhesion can be improved in the same way like for the adhesion of the PEEK carriers: PEEK stripes of approximately 1 mm width and 0.125 mm thickness are positioned between the trap stage and the trap before varnish

[15] Viktor-Franz-Hess building, 4th floor, room 4/17; cleanroom class ISO 4 (ISO 14644-1 cleanroom standards)

[16] Varnish cured at 100 °C for approx. 1 h

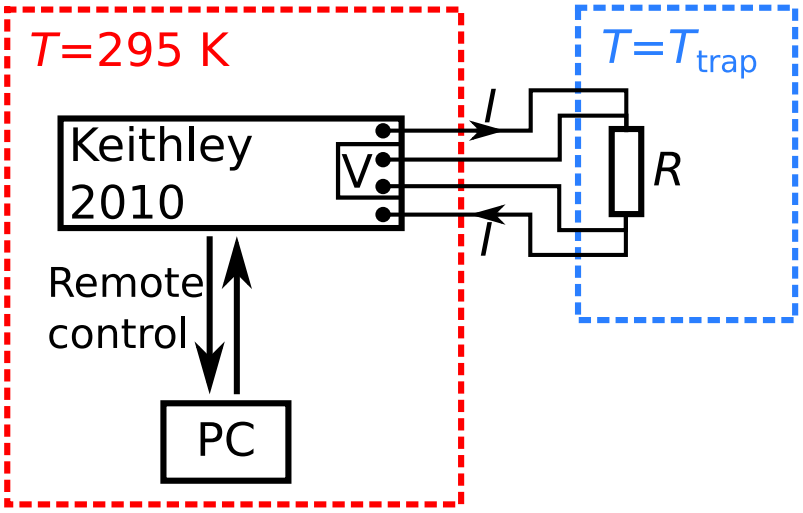

Figure 5.9: 4-wire resistance measurement setup. A Keithley 2010 multimeter is connected twice to each end of the meander R. One pair of connections is used to send a constant current I and the other connection is used to measure the voltage drop V on the meander. The multimeter is controlled by a LabVIEW program on the PC. The thermal gradient between the multimeter and the meander resistance ($T_{\mathrm{trap}} = 10\,\mathrm{K} - 120\,\mathrm{K}$) can produce thermal offset voltages. They are compensated using a method described in the main text.

is added. This enables one to use a thicker layer of varnish in a controlled way. Thus the stress on the varnish is distributed over this layer and should make the bond more reliable during thermal cycling.

After curing the adhesive, the trap electrodes are connected to the PCBs by gold wire bonds with $25\,\mu\mathrm{m}$ diameter (the wire bonds are shown on the photo in figure 6.5).

5.4 4-wire resistance measurement

On both meander designs there are additional meanders which are identical to the meanders connected to the meander-electrode (see figure 4.10 and figure 4.13). In this way the meander resistance $R(T)$ can be measured during the trap operation. Knowing $R(T)$ and T allows us to calculate the Johnson noise from the meander.

In order to determine $R(T)$ with a 4-wire measurement, the meander is connected twice at each end. We used a digital multimeter[17] to perform the measurement via remote control from the PC. A schematic is shown in figure 5.9. One of the two connections is used to send a constant current I through the meander and the other connection is used to measure the voltage drop V on the meander. Temperature gradients along the cables between the multimeter ($T = 295\,\mathrm{K}$) and the meander inside the cryostat ($T = 10\,\mathrm{K} - 120\,\mathrm{K}$) can produce thermal offset voltages V_{T} due to the Seebeck-effect [70]. These are compensated automatically by the multimeter in the following way [71]: It measures two voltages (V_{m1} and V_{m2}) per measurement cycle. First

$$V_{\mathrm{m1}} = RI_{\mathrm{rs}} + V_{\mathrm{T}}, \tag{5.4}$$

[17] Keithley 2010 multimeter with 7.5 digit resolution

with a reduced source current $I_{\mathrm{rs}} = 10\,\mu\mathrm{A}$ and then

$$V_{\mathrm{m2}} = RI_{\mathrm{fss}} + V_{\mathrm{T}}, \tag{5.5}$$

with a full-scale source current I_{fss}, which depends on the resistance range. A table of the I_{fss} value vs resistance range is given in the datasheet of the multimeter. Subtracting (5.5) from (5.4) gives

$$V_{\mathrm{m1}} - V_{\mathrm{m2}} = R(I_{\mathrm{rs}} - I_{\mathrm{fss}}) \tag{5.6}$$

and therefore

$$R = \frac{V_{\mathrm{m1}} - V_{\mathrm{m2}}}{I_{\mathrm{rs}} - I_{\mathrm{fss}}}. \tag{5.7}$$

This resistance measurement is logged using a LabVIEW program, together with the temperature and the pressure. Results for $R(T)$ are presented in section 6.1.1.

Chapter 6

Experimental Results

The aim of this project is to measure heating rates in the specially designed YBCO-traps at different temperatures. The superconducting properties of YBCO should allow us to compare the effects of Johnson noise with an yet unknown noise source within a temperature difference of a few kelvins. In order to perform these measurements two requirements must be fulfilled.

First, YBCO must be in the superconducting state below T_c. This was verified by 4-wire resistance measurements of an on-chip YBCO-meander structure. The results are shown in section 6.1.1 and allowed us to determine T_c. Additionally, the superconducting transition was observed in the resonator Q measurements presented in section 6.1.2.

Second, the temperature of the trap T_trap must be known precisely in order to measure the temperature dependence of the heating rate Γ_h in the YBCO-traps. Temperature gradients between the sensor and the trap must be taken into account. The characterisation of these gradients and the resulting corrections are discussed in section 6.2.

Furthermore, a comparison between simulation and experiment was performed in order to test the accuracy of the simulations. A HTCYK1-trap was used to measure the secular frequencies of a trapped ion for different voltage settings. The measurements were compared with the secular frequencies obtained in the simulation. The results are analysed in section 6.3.

Finally, heating rate measurements were performed in the superconducting state (with $T_\mathrm{trap} < T_\mathrm{c}$) both for a HTCYK1-trap (section 6.4.1) and a two-meander trap (section 6.4.2). We were not able to measure Γ_h for $T_\mathrm{trap} > T_\mathrm{c}$ so far, as is discussed in section 6.4.2.

6.1 Observation of the superconducting transition

6.1.1 4-wire resistance measurements of a YBCO-meander structure

One of the requirements for the project is that YBCO must be in the superconducting state below T_c. Furthermore, knowing the temperature dependence of the meander resistance $R(T)$ and T allows us to calculate the Johnson noise from the meander. In this way it will be possible to compare the expected noise level with the heating rate measurements.

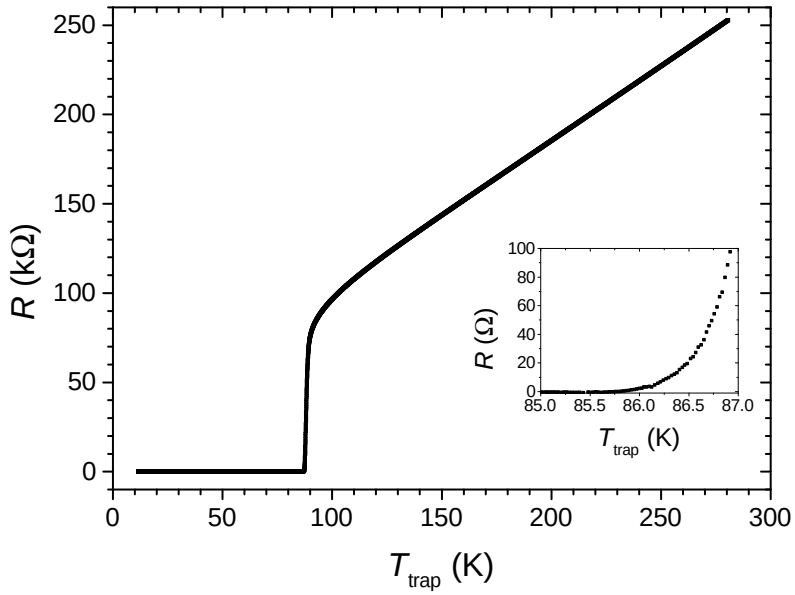

Figure 6.1: 4-wire resistance measurement of a YBCO meander structure during the cool down of the cryostat. The temperature was measured with the sensor on the trap stage. The inset shows the absence of measurable resistance ($R < 5 \times 10^{-5}\,\Omega$) below $T_\mathrm{c} = 85.7(2)\,\mathrm{K}$.

The superconducting state was confirmed by measuring the resistance of a YBCO-meander structure on the trap chip with a 4-wire measurement scheme. The meander is connected twice at each end to a multimeter[1] and a current is sent through one pair of the connections while the other pair is used to measure the voltage. In addition with the compensation of thermal offset voltages (see section 5.4), this allowed us to measure the resistance with a high precision (down to around $10^{-5}\,\Omega$).

The 4-wire resistance measurement was performed on three different trap chips during several cool down and warm up cycles of the cryostat. It should be noted that a warm up process means that the cryostat is turned off and it slowly warms up until it reaches room temperature, no additional heating is applied to speed up this process. During the thermal cycling, the temperature of the trap chip changes with a rate of approximately $1\,\mathrm{K/min}$. The slow rate minimises the temperature gradients between the trap chip and the sensor on the trap stage (the position of the sensor is described in section 5.3.1). The temperature of the trap T_trap was measured with this sensor [2] and a Cryo-con[3] temperature controller. An example of a measurement curve during a cool down cycle is presented in figure 6.1 showing the typical temperature dependence of YBCO: For $T_\mathrm{trap} > 100\,\mathrm{K}$, the resistance R depends linearly on T_trap. Cooling the chip further down leads to a sharp decrease of R until it drops to zero below T_c. All measurements of $R(T_\mathrm{trap})$ reproduced this expected behaviour.

[1] Keithley 2010 multimeter with 7.5 digit resolution
[2] Lakeshore DT-670C-SD: Silicon Diode with $32\,\mathrm{mK}$ precision and $1\,\mathrm{K}$ tolerance band for $T < 305\,\mathrm{K}$
[3] Cryo-con Model 24 from Cryogenic Control Systems, Inc

Cycling process	cool down 1	cool down 2	cool down 3	warm up
T_c	85.8(1)	84.9(2)	85.7(2)	85.1(2)

Table 6.1: Critical temperature T_c for four different thermal cycling processes. In the superconducting state, the measured resistance fluctuates with σ due to imperfect compensation of thermal voltages and the limited resolution of the multimeter. We obtained T_c by finding the temperature at which the mean value of $R \approx 2\sigma$. The given error results from the accuracy of determining T_c in the described way. The difference between the measured values of T_c can result from varying temperature gradients in the setup caused a by different cooling rate of the cryostat in each cycle.

Below T_c, we were able to show that the resistance is below $R < 5 \times 10^{-5}\,\Omega$ by using the compensation method minimising the influence of thermal offset voltages presented in section 5.4 and a probing current of $I_{fss} = 10\,\mathrm{mA}$. In the superconducting state, the measured resistance fluctuates with σ due to imperfect compensation of thermal voltages and the limited resolution of the multimeter. The resolution of the multimeter and therefore also σ depend on the probing current I_{fss}. For $I_{fss} = 10\,\mathrm{mA}$, it was measured that $\sigma \approx 5 \times 10^{-5}\,\Omega$. We obtained T_c by finding the temperature at which the mean value of $R \approx 2\sigma$.

To measure T_c precisely the influence of the probing current on the resistance has to be considered: If I_{fss} exceeds the critical current I_c, YBCO leaves the superconducting state leading to a lower temperature at which the resistance exceeds 2σ. Ceraco measured a critical current density of $j_c = 3.3\,\mathrm{MA/cm^2}$ at $T = 77\,\mathrm{K}$. For the meander with a thickness of $50\,\mathrm{nm}$ and a width of $10\,\mu\mathrm{m}$, this leads to $I_c = 17\,\mathrm{mA}$ at $T = 77\,\mathrm{K}$. I_c decreases with increasing temperature T so that I_c can be exceeded close to T_c [23]. This shifts the observed T_c to lower temperatures. Comparing the probing current $I_{fss} = 10\,\mathrm{mA}$ with $I_{fss} = 10\,\mu\mathrm{A}$, we observed that T_c is shifted by approximately $0.5\,\mathrm{K}$. Therefore the lowest probing current $I_{fss} = 10\,\mu\mathrm{A}$ was used to determine T_c.

Although the thermal cycling happens at a slow rate of about $1\,\mathrm{K/min}$, small temperature gradients remain. These vary slightly between the thermal cycling processes leading to a spread of the observed T_c in a range of $0.9\,\mathrm{K}$. This spread can be caused a by different cooling rate of the cryostat in each cycle. The obtained critical temperatures during three cool down and one warm up process are given in table 6.1. Taking the average, the phase transition was observed at

$$T_c = 85.4\,\mathrm{K} \pm 0.2\,\mathrm{K}(\textit{sys1}) \pm 1\,\mathrm{K}(\textit{sys2}), \tag{6.1}$$

where the first error (sys1) is the systematic error from small residual temperature gradients during the measurements. It is calculated from averaging over the measurements in table 6.1. The second error (sys2) is the systematic error resulting from the limited accuracy of the temperature sensor. The fact that the measurement of T_c during a warm up lies within the spread of the measurements during the cool down cycles shows that there are no large temperature gradients between the sensor on the trap stage and the trap. Additionally, the result for T_c agrees with the measurement made by Ceraco $T_c = 85.6(5)\,\mathrm{K}$. This confirms that during a cool down (or warm up) of the cryostat the temperature sensor on the trap stage provides an accurate value for the trap temperature. This assumption is not valid when the local heater (see section 5.3.1) is used to change the trap temperature.

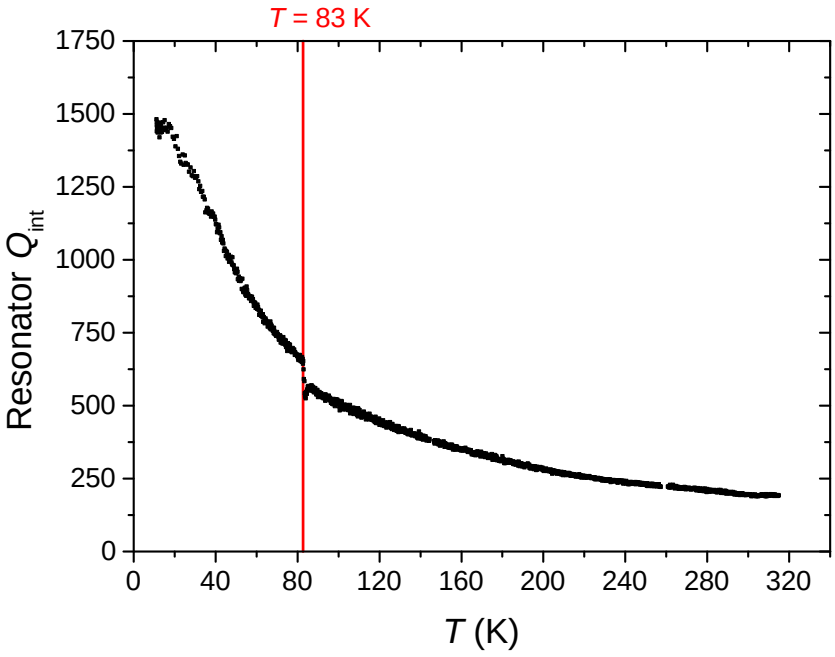

Figure 6.2: Intrinsic resonator quality factor Q_{int} as a function of the resonator temperature T. The data was taken during a cool down of the cryostat. The red line shows the temperature T_{c} at which a sharp increase of Q_{int}, caused by the phase transition of YBCO, is observed. As T_{c} is defined as the temperature at which the resistance starts to increase, the red line shows the beginning of the jump in the Q-measurement. The difference between the maximal quality factor in the plot ($Q_{\mathrm{int}} \approx 1450$) and the value 1514(10) given in table 5.1 is explained by the fact that f_0 is shifted by $0.2\,\mathrm{MHz}$ during the measurement. As f_0 had to stay within the measurement width of the spectrum analyser, the spectrum analyser was not set to its maximum resolution.

In this case the temperature gradients between the trap stage and the trap are not negligible and the temperature of the sensor has to be corrected. The correction and a 4-wire measurement where the local heater was used are both presented in section 6.2.2.

6.1.2 The superconducting transition in the resonator-Q measurement

Measuring the intrinsic quality factor Q_{int} of the resonator provides another possibility to show that the trap is in the superconducting state below T_{c}. To determine Q_{int}, a spectrum analyser[4] is used to measure the gain of the resonator as a function of the frequency. The output power of the spectrum analyser is $5\,\mathrm{dBm}$ and does not affect the temperature of the resonator. The data was analysed by a MATLAB-script that determines the resonance frequency f_0 and the $-3\,\mathrm{dB}$ full-width voltage gain bandwidth of the resonance Δf. From this measurement Q_{int} is calculated as described in detail in section 5.2. The temperature

[4] VIA Bravo 2 from AEA Technology Inc.

of the trap T_{trap} was measured with the trap stage sensor [5] and a Cryo-con[6] temperature controller.

A measurement of the quality factor Q_{int} during a cool down of the cryostat is shown in figure 6.2. While the temperature is decreased from $300\,\mathrm{K}$ to $83(2)\,\mathrm{K}$, Q_{int} increases smoothly, without jump. This increase is due to the reduction of the resistance of the resonator copper coil. At $83(2)\,\mathrm{K}$, Q_{int} jumps by about 18 %. Cooling down further until $13\,\mathrm{K}$ leads to a smooth increase of Q_{int}, again caused by the reduction of the resonator coil. Apart from the jump, the curve is similar to the one reported in [67], where a similar resonator together with a silicon trap was used. Therefore the jump at $T = 83(2)\,\mathrm{K}$ is expected to be caused by the superconducting transition of the trap chip. The fact that the jump is a rather small feature compared to the overall decrease of Q_{int} over the whole temperature range leads to a reduced accuracy in determining the position of the jump. Therefore the measurement of T_{c} from this curve is significantly less accurate than in resistance measurements of the meander structure. This can be the reason of the slight deviation between these measurements.

The change in the resonator-Q due to the phase transition of YBCO at $T = T_{\mathrm{c}}$ can be observed in a more pronounced way if the trap stage is heated with the local heater while the rest of the resonant circuit stays at cold temperatures. The result of this measurement can be seen in figure 6.3. Q_{int} is reduced by only about 2 % from $T \approx 10\,\mathrm{K}$ to $T = 90.5(5)\,\mathrm{K}$. At $T = 90.5(5)\,\mathrm{K}$, Q_{int} jumps by around 23 % due to the phase transition of YBCO. The measured temperature at which the phase transition occurs is significantly different from $T_{\mathrm{c}} = 85.4(1.2)\,\mathrm{K}$ obtained by the 4-wire-measurements during cool downs and warm ups of the cryostat. A correction for the temperature sensor is presented in section 6.2.2. Using this correction the critical temperature derived from the Q-measurement of the resonator is shifted from 90.5(5) K to $86.7(1.5)\,\mathrm{K}$, showing good agreement with the value obtained by the 4-wire-measurements.

As the spectrum analyser has a fixed output power of $5\,\mathrm{dBm}$, the measurements were performed with that power. One could object that the conclusion is not valid during trapping, where an input power of around $17\,\mathrm{dBm}$ is used. It is shown in the following calculation that the higher input power has no significant effect on the observable T_{c}. Therefore the resonator-Q measurements confirm the result of the 4-wire measurements that the trap chip is in the superconducting state for $T < T_{\mathrm{c}}$.

Ceraco measured a critical current density of $j_{\mathrm{c}} = 3.3\,\mathrm{MA/cm^2}$ at $T = 77\,\mathrm{K}$. For the smaller RF-electrode with a thickness of $50\,\mathrm{nm}$ and a width of $200\,\mu\mathrm{m}$, this leads to $I_{\mathrm{c}} = 330\,\mathrm{mA}$ at $T = 77\,\mathrm{K}$. The current I running through this electrode is given by

$$I = \frac{1}{3}\Omega_{\mathrm{RF}} V_{\mathrm{RF}} C = 83\,\mathrm{mA}, \tag{6.2}$$

where $\Omega_{\mathrm{RF}} = 2\pi \cdot 17.5\,\mathrm{MHz}$ is the radio-frequency, $V_{\mathrm{RF}} = 175\,\mathrm{V}$ is a typical RF-voltage for trapping, $C \approx 13\,\mathrm{pF}$ is the capacitance of the resonator and the factor $1/3$ results from the two parallel RF-electrodes. At $77\,\mathrm{K}$ the relation between the current and the critical current is about $I/I_{\mathrm{c}} \approx 4$. In the 4-wire measurement with a current of $I = 10\,\mathrm{mA}$, this relation was $I/I_{\mathrm{c}} \approx 2$ and shifted the observable critical temperature by only $0.5\,\mathrm{K}$

[5] Lakeshore DT-670C-SD: Silicon Diode with 32 mK precision and 1 K tolerance band for $T < 305\,\mathrm{K}$

[6] Cryo-con Model 24 from Cryogenic Control Systems, Inc

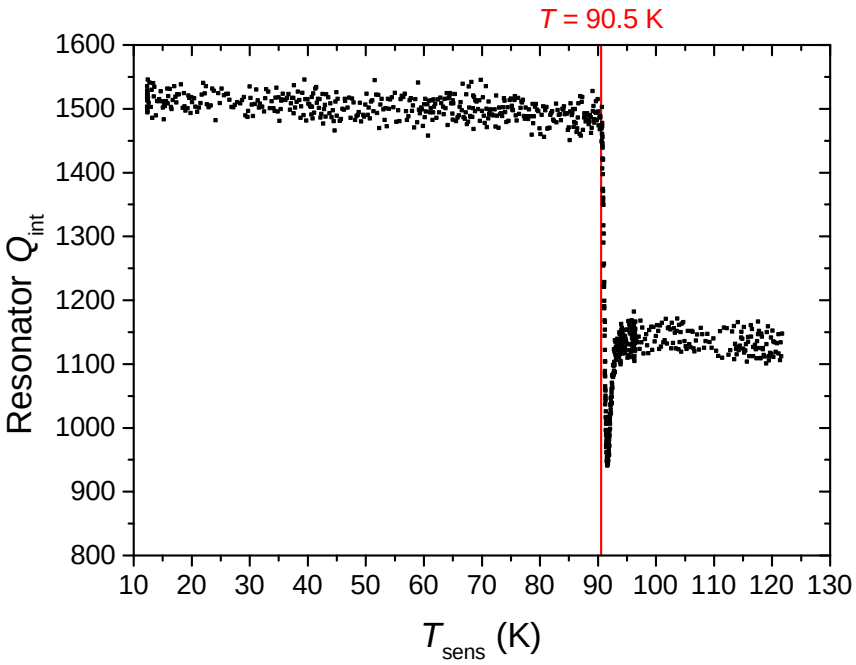

Figure 6.3: Quality factor Q_{int} of the resonator as a function of the temperature of the trap stage T_{sens}. Q_{int} was determined from the measurements with a spectrum analyser. The trap stage was only heated by the local heater. $Q_{\mathrm{int}}(T)$ shows a step-like behaviour, where the red line shows the temperature T_{c} at which a sudden change of Q is observed due to the phase transition of YBCO. As T_{c} is defined as the temperature at which the resistance starts to increase, the red line shows the beginning of the jump in the Q-measruement. For $T < 90\,\mathrm{K}$, Q_{int} stays constant within $2\,\%$, then it drops. For $T_{\mathrm{sens}} > 93\,\mathrm{K}$ it does not drop further, because the resistance is then given by the gold layer on top of the YBCO-film. Between $90\,\mathrm{K}$ and $93\,\mathrm{K}$ Q_{int} first drops below 950 before it goes up again to 1150. We have not observed a similar drop in the resonator gain monitored by the voltage on the capacitive divider while the temperature was increased above T_{c}. Therefore we suspect that drop to be an artificial result of our measurement scheme. Scanning the frequency to calculate one data point for Q_{int} takes the time t_m which is a few seconds. During that time the resistance of the trap chip is not constant, because around T_{c} it increases sharply within a temperature difference of a few kelvins. As we scan the temperature by manually changing the voltage on a power supply, a relevant temperature change happens within the measurement time t_m. Additionally, within the same time-scale the resonance frequency is changing. In total it jumps by about $10\,\mathrm{kHz}$. This influences the measurement and leads to the artificial drop in Q_{int}. This effect was repeatedly observed but not further investigated, because it does not alter the conclusions from this figure.

(see section 6.1.1). Consequently, the effect of a typical RF-voltage for trapping on the observable T_c is even smaller than $0.5\,\mathrm{K}$ and can be neglected.

Two other important conclusions can be drawn from the measurements presented in this section:

First, the fact that above T_c the resonator-Q drops by 23 % lead to a drop of the RF-voltage in the experiment by only about 12 %. This enabled us to keep an ion in the trap while we heat the trap stage from cold temperatures to temperatures above T_c without a stabilisation of the RF-voltage on the trap.

Second, the measurement where only the trap stage is heated up (figure 6.3), shows that Q_{int} is reduced by only about 2 % from $T \approx 10\,\mathrm{K}$ to $T = 86.7(1.5)\mathrm{K}$. Consequently, the temperature of the resonator coil is not much affected by the local heater on the trap stage showing a good thermal decoupling of the coil from the local heater. This confirms the good thermal insulation presented in section 5.3.2.

6.2 Measurement of the actual trap temperature

As mentioned in the last section, the temperature measured by the trap stage sensor can deviate from the actual trap temperature by several kelvins when the trap stage is heated with the local heater. Therefore the temperature needs to be corrected. Due to the high thermal conductivity of copper it is assumed that the temperature gradients on the trap stage are negligible. As the trap and the temperature sensor are directly glued to the trap stage, one could expect that the sensor provides an accurate temperature of the trap itself. The measurement of T_c in section 6.1.1 confirms that this assumptions holds during a cool down or a warm up of the cryostat. However, if the trap stage is heated by the local heater, the bonding wires cause a non-negligible heat flow W_{bonds} between the heated trap and the cold PCBs. The actual temperature of the trap T_{trap} is therefore smaller than the measured temperature T_{sens}. The difference is discussed in section 6.2.1. The 4-wire-resistance measurements allow us to correct the temperature measured with the stage sensor so that it matches the actual trap temperature within 1 K. The correction is presented in section 6.2.2.

6.2.1 Temperature difference between the trap stage and the trap

In order to discuss the origin of the temperature difference between the trap stage and the trap, the heat transfer between the different parts of the setup is discussed in this section. A schematic of the relevant thermal connections and temperatures is shown in figure 6.4. The local heater heats up the trap stage. The thermal conductivity from the trap stage to the trap is given by the heat flow through the varnish W_{varnish}. As discussed later in this section, in the final setup this thermal conductivity is increased by bonding wires from the trap stage to the trap creating the heat flow $W_{\mathrm{bonds,2}}$. The trap electrodes are connected with the PCBs by bonding wires creating a heat flow $W_{\mathrm{bonds,1}}$ from the trap to the cold PCBs. It can be calculated that the radiative heat transfer W_{rad} between the trap and the surrounding setup is $W_{\mathrm{rad}} \ll 10^{-7}\,\mathrm{W}$ (see appendix B). The required power to heat up the trap stage to $100\,\mathrm{K}$ is around $100\,\mathrm{mW}$ (see section 5.3.2). Therefore the radiative heat

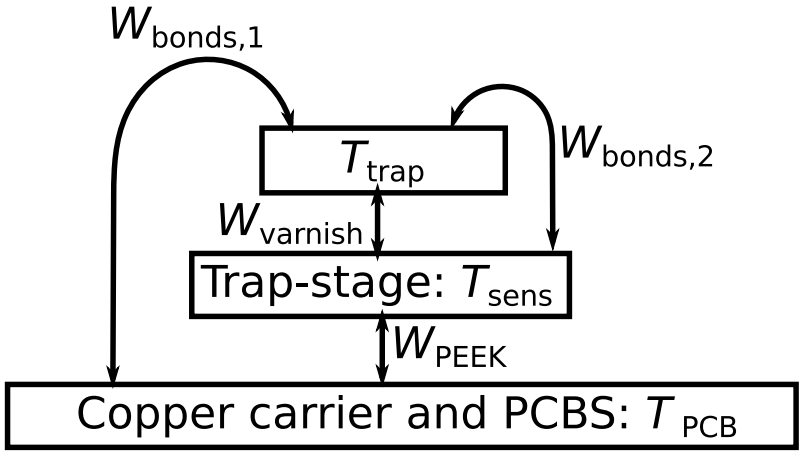

Figure 6.4: Thermal connections around the trap. W_{PEEK} is the heat flow from the copper carrier to the trap stage through the PEEK-carriers. W_{varnish} is the heat flow from the trap stage to the trap through the varnish. The heat flow from the trap stage to the trap is increased by 90 additional bonding wires ($W_{\mathrm{bonds,2}}$). $W_{\mathrm{bonds,1}}$ is the heat flow from the trap to the PCBs through the bonding wires. The local heater is attached to the trap stage and therefore the temperature measured with the sensor attached to the trap stage $T_{\mathrm{sens}} > T_{\mathrm{trap}}, T_{\mathrm{PCB}}$. Important for the temperature correction is the difference $T_{\mathrm{trap}} - T_{\mathrm{sens}}$.

transfer can be neglected.

The heat flow $W_{\mathrm{bonds,1}}$ causes a temperature difference between the sensor on the trap stage (T_{sens}) and the trap (T_{trap}). This temperature difference $T_{\mathrm{sens}} - T_{\mathrm{trap}}$ depends on the exact values of $W_{\mathrm{bonds,1}}$, the heat flow through the varnish W_{varnish} and the heat flow through the additional bonding wires $W_{\mathrm{bonds,2}}$.

From the measurements made by Ceraco and our 4-wire resistance measurements, the critical temperature is known to be $85.6(5)\,\mathrm{K}$. While heating up the trap, we can determine the time when it reaches the critical temperature by measuring the resistance of the YBCO-meander structure (see section 6.1.1). Measuring the trap stage temperature with the sensor allows us to estimate the temperature difference between the trap stage and the trap $T_{\mathrm{sens}} - T_{\mathrm{trap}}$.

Our preliminary measurements were done without bonding wires between the trap stage and the trap. At the time when the resistance measured by the 4-wire measurement started to increase, we measured $T_{\mathrm{sens}} \approx 135\,\mathrm{K}$ leading to $T_{\mathrm{sens}} - T_{\mathrm{trap}} \approx 50\,\mathrm{K}$ This big difference was caused by a bad conductivity W_{varnish} resulting from the small contact area between the trap and the trap stage. Before the varnish is cured, the contact area is about $0.5\,\mathrm{cm}^2$. However, while it is cured, it looses a significant amount of weight as described in section 5.3.3. This reduces the contact area and leads to the bad conductivity W_{varnish}.

To improve the thermal conductivity between the trap and the trap stage, 90 bonding wires are placed from the gold surface of the electrical ground plane on the trap to the trap stage (see figure 6.5). They are placed in the middle of the four sides of the trap and lead to $T_{\mathrm{sens}} \approx 89\,\mathrm{K}$ at $T_{\mathrm{trap}} = T_{\mathrm{c}}$ and thus $T_{\mathrm{sens}} - T_{\mathrm{trap}} \approx 3\,\mathrm{K}$. This temperature difference still limits the accuracy of the trap temperature measurement. A correction of the sensor is discussed in the next section.

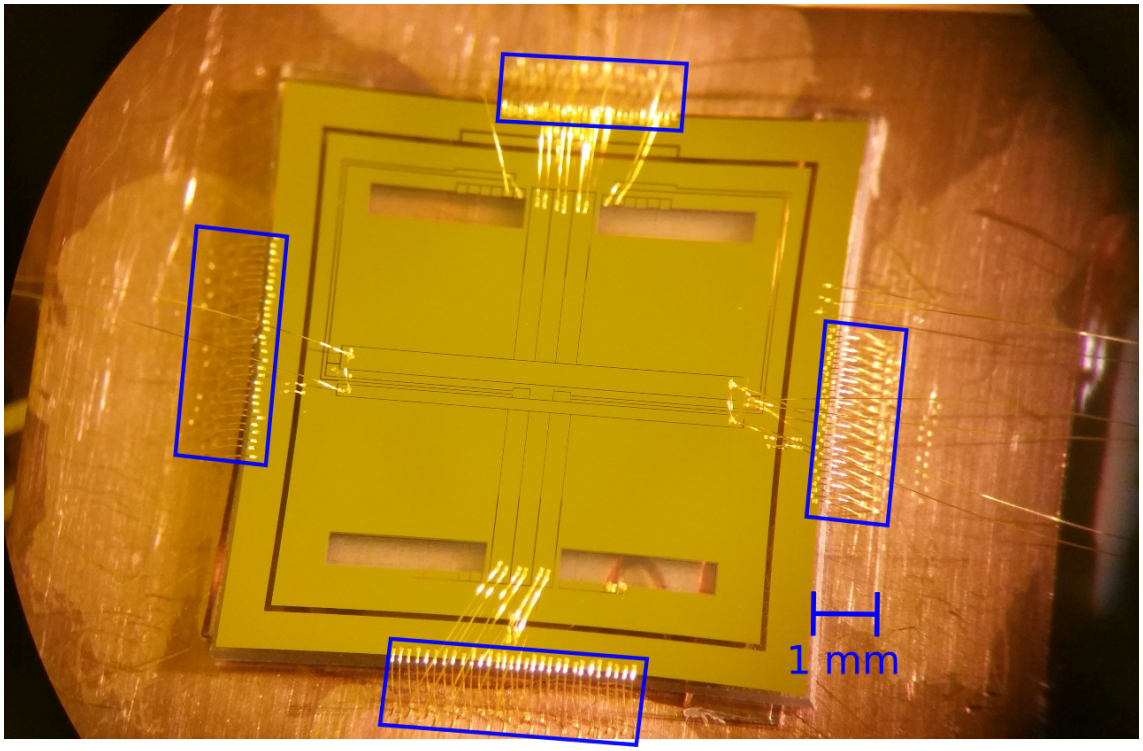

Figure 6.5: Two-meander YBCO-trap installed on the trap stage. Bonding wires connect the trap electrodes with the PCBs that surround the trap stage. The thermal conductivity between the trap stage and the trap is increased by making 90 bonding wire connections between the trap and the trap stage (indicated by the blue rectangles). No bonding wires are placed in the corners of the trap to minimise stray lights from the lasers that are shone diagonal over the trap. The four transparent rectangular parts of the trap chip are the meander-structures where the gold layer was removed.

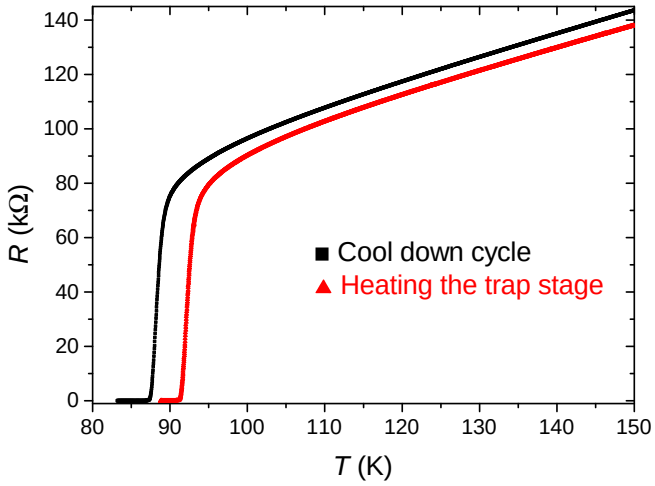

Figure 6.6: Resistance measurement of a meander structure on the trap chip. The black data points were taken during a cool down of the cryostat. In this case the temperature sensor gives an accurate measurement of the temperature of the trap. For the red data points only the trap stage was heated while the cryostat was cooled down to approximately $10\,\mathrm{K}$ leading to a temperature difference between the trap stage, where the sensor is placed, and the trap. This reduces the accuracy of the temperature measurement.

6.2.2 Correction of the trap stage temperature sensor

During a cool down or a warm up, the temperature difference between the temperature sensor and the trap are small as discussed in section 6.1.1. In the previous section it was shown that this temperature difference is significantly higher when the local heater is used. In both cases the resistance of a YBCO-meander structure on the trap can be measured with a 4-wire measurement. In the following it is shown how the 4-wire resistance measurement in the first situation can be used as a reference for the second situation and a correction of the trap stage temperature sensor is determined. Figure 6.6 shows the resistance measurement in both situations and the data is used for the correction.

First it is discussed that a single resistance measurement during a cool down can be taken for the correction. The agreement between our measurements of T_c with the 4-wire resistance measurements and the measurements made by Ceraco confirms that during a cool down (or a warm up) process of the cryostat the trap stage temperature sensor measures accurately the temperature of the trap. The temperature difference between a cool down and a warm up process can be determined by measuring the temperature at a specific resistance R. In the first few kelvins above T_c the resistance has a sharp increase and therefore the measurement is very sensitive to small temperature gradients. At $T = 90\,\mathrm{K}$ the temperature difference was approximately $0.6\,\mathrm{K}$. It decreases to $< 0.3\,\mathrm{K}$ above $100\,\mathrm{K}$. If one compares two cool down cycles the difference at $T = 90\,\mathrm{K}$ is smaller than $0.2\,\mathrm{K}$ and it is negligible ($< 0.03\,\mathrm{K}$) above $100\,\mathrm{K}$. These small differences allow us to use a single cool down (or warm up) measurement for the calibration.

The measurement of the resistance during a cool down is indicated by $R_\mathrm{trap}(T_\mathrm{trap})$. If

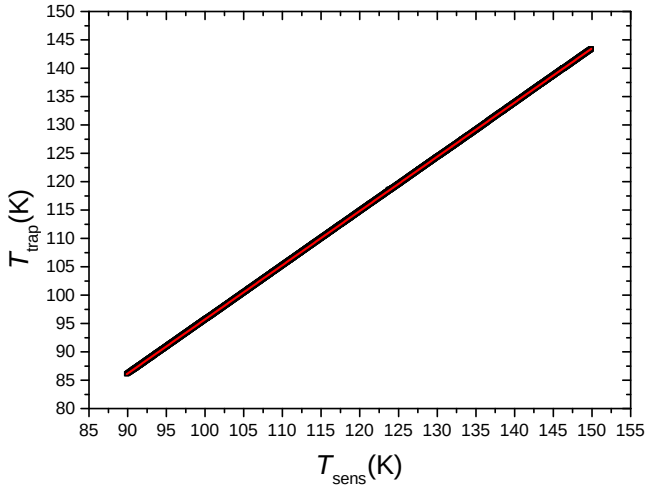

Figure 6.7: Calibration curve of the trap temperature T_{trap} depending on the temperature of the sensor T_{sens} when only the trap stage is heated. The black points are the data obtained with the correction method described in the main text. The red line is a linear fit of the data given by $T_{\mathrm{trap}} = 0.95542(1) \cdot T_{\mathrm{sens}} + 0.1889(3)\,\mathrm{K}$.

the trap stage is heated up with the local heater, the resistance measurement is indicated by $R_{\mathrm{sens}}(T_{\mathrm{sens}})$. This leads to the following correction of the sensor temperature:

$$T_{\mathrm{trap}}(T_{\mathrm{sens}}) = R^{-1}_{\mathrm{trap}}(R_{\mathrm{sens}}), \tag{6.3}$$

with R^{-1}_{trap} defined as the inverse function of $R_{\mathrm{trap}}(T_{\mathrm{trap}})$. An example of such a correction is given in the following.

$R_{\mathrm{trap}}(T_{\mathrm{trap}})$ contains about 1500 data points in the range $T = (86 - 143)\,\mathrm{K}$. The data can be interpolated linearly. For technical convinience, we used MATLAB functions that interpolate the data with piecewise cubic hermite polynomials. Choosing hermite polynomials instead of a linear interpolation does not alter the result. The same interpolation was done on a measured $R_{\mathrm{sens}}(T_{\mathrm{sens}})$ curve. Equation 6.3 is used to obtain the correction curve plotted in figure 6.7. It shows that T_{trap} depends linearly on T_{sens}. A linear fit of the data is given by

$$T_{\mathrm{trap}} = 0.95542(1) \cdot T_{\mathrm{sens}} + 0.1889(3)\,\mathrm{K}, \tag{6.4}$$

where only the errors from the linear fit are given in the brackets. Assuming that the dependence stays linear below $86\,\mathrm{K}$, equation (6.4) provides a correction for the whole relevant temperature range down to $10\,\mathrm{K}$.

The accuracy of this correction can be estimated with two known temperature values. The first one is at the phase transition of the superconductor. Using the correction, the trap temperature at the phase transition for the measured value $T_{\mathrm{sens}} = 89.1(1)\,\mathrm{K}$ is calculated to be 85.3(1) K and agrees with the reference from Ceraco $T_{\mathrm{c}} = 85.6(5)\,\mathrm{K}$. The second point is at the coldest reachable temperature (in this case it was at $13\,\mathrm{K}$[7]). The local heater

[7]The temperature is higher than the coldest temperature in figure 5.7, because the performance of the cryostat was slowly degrading during the time measurements have been taken in this thesis.

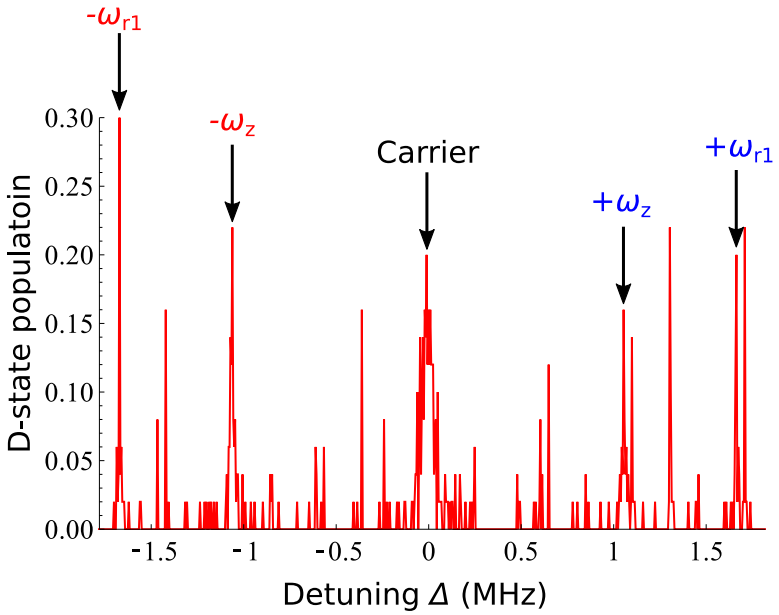

Figure 6.8: Spectroscopy on the $S_{1/2}$-$D_{5/2}$ transition with 729 nm laser-light. The origin of the horizontal axis is set to the carrier transition. Due to the higher coupling strength of the carrier transition compared to the sidebands, the carrier peak is broader than the sideband peaks. The length of the 729 nm laser pulse was 1 ms and therefore much longer than the typical time for one carrier rabiflop (about 14 µs), which is the time for transferring the whole population from the $S_{1/2}$-state to the $D_{5/2}$-state. Due to this pulse length one would expect a D-state population of approximately 0.5 on resonance [31]. The maximum population at the peaks is only around 0.25, because optical pumping was not applied during the pulse sequence. This causes that approximately half of the population is in the $m = 1/2$ Zeeman sublevel of the $S_{1/2}$-state and is not affected by the 729 nm laser pulse.

is not used at this temperature and therefore the difference between T_{trap} and T_{sens} should be negligible. Taking the correction from equation (6.4), $T_{\mathrm{trap}} - T_{\mathrm{sens}} = -0.4\,\mathrm{K}$.

This difference shows that the accuracy of the correction lies within 1 K. This accuracy is sufficient for characterising the temperature dependence of the heating rates.

6.3 Comparison of trap simulation with measured trap frequencies

The *electrode package* is an efficient tool for simulating surface traps as described in section 4.3 [56]. In ion trap quantum-information techniques like rearranging ion strings or single-ion addressing, the potential along the trapping sites must be known with an accuracy better than a few percent [72, 73]. Therefore it is of great interest to know if the trap simulations predict accurately the observed trap potential.

Differences between simulations and experiment can have four different origins:

- **Stray fields from surfaces close to the trap chip:** Charges on electrically isolated

materials or potential differences between metallic surfaces can cause stray electric fields.

- **Stray fields from the trap surface:** Surface contaminations can cause stray electric fields.

- **Fabrication tolerances:** Finite resolution in the chip patterning leads to differences between the nominal and the real size of the electrodes.

- **The limited accuracy of the numerical simulation:** The *electrode package* uses the 2D gapless and the infinite plane approximations (see section 4.3.1).

The electric stray field from the experimental setup $\vec{E}_\mathrm{s}$ can be compensated by shim voltages and if necessary it can be reduced by shielding the trapping area with a metallic cage. However, stray fields from the trap cannot be reduced by shielding or other changes in the setup and can limit the usability of surface-electrode traps [72]. Consequently, errors from stray fields of the surrounding setup are less critical than stray fields form the chip. It is shown in the following that measuring the trapping frequencies enables us to exclude stray fields from the surrounding setup from the possible origins for differences between simulation and experiment.

The distance d between the ion's position and the parts in the experimental setup surrounding the trap is much higher than the ion-electrode separation ($d \gtrapprox 1\,\mathrm{cm} \gg 226\,\mu\mathrm{m}$). The electric stray field from these parts decreases with the distance d. As the curvature of the potential is the derivative of the electric field, it decreases faster than the electric field with the distance d. For example, a stray charge will create a mirror charge on a near metallic surface resulting in a dipole. The strength of the electric field of a dipole decreases as $|\vec{E}_\mathrm{s}| \propto d^{-3}$. The curvature κ of its potential decreases as $|\kappa| = |\nabla \vec{E}_\mathrm{s}| \propto d^{-4}$. Therefore at the ion's position it can be assumed that the curvature κ resulting from stray fields of the surrounding setup is negligibly small compared to the curvature resulting from stray fields coming from the trap surface or from the RF- and DC-voltages.

The trapping frequencies ω_i are proportional to the curvature of the potential at the ion's position. The discussion above shows that this curvature is dominantly produced by stray fields from the trap surface and by the RF- and DC-voltages. Consequently, measuring ω_i enables one to detect differences between the simulations and the experiment that result mainly from stray fields from the trap and the limited accuracy of the numerical simulations. We can measure the trapping frequencies with a high precision as the low linewidth $729\,\mathrm{nm}$ laser allows us to do sideband spectroscopy [30]. The used pulse sequence for the spectroscopy is explained in section 2.4.6. An example of a spectroscopy measurement is shown in figure 6.8.

The measurements of ω_i were performed with an ion trapped in a HTCYK1-trap installed on the existing trap mount (see [29]). In order to compare the simulations with the measurements, the voltages on the trap electrodes must be known. The DC-voltages can be measured directly with a multimeter, and the RF-voltage with the capacitive divider in the resonant circuit (see section 5.2). However, the relation $c = V_\mathrm{RF}/V_\mathrm{cd}$ between the voltage on the capacitive divider V_cd and the RF-voltage on the trap V_RF has to be determined first. In section 6.3.1, we present the measurement of the radial trapping frequencies for

five different RF-voltages and a simulation of radial frequencies versus RF-voltage. c is then obtained by finding the optimal agreement between simulation and measurements.

Comparing the simulated with the measured secular frequencies for the five different RF-voltages is not sufficient to test the agreement between simulation and experiment, because determining c minimised possible deviations between simulation and experiment. Therefore in section 6.3.2, we present the measurements of the trapping frequencies for three different sets of DC-voltages with the same RF-voltage and discuss the deviation between simulation and experiment for these measurements.

6.3.1 Determining the applied RF-voltage

The capacitive divider in the RF resonator circuit consists of two capacitors C_1 and C_2 (see section 5.2). Nominally the RF-voltage V_{RF} on the trap is given by

$$V_{\mathrm{RF}} = \frac{C_2}{C_1 + C_2} \cdot V_{\mathrm{cd}} = c \cdot V_{\mathrm{cd}}, \quad \text{with} \quad c \approx 401 \tag{6.5}$$

where V_{cd} is the voltage measured on the capacitive divider and the values $C_1 = 2.5\,\mathrm{pF}$ and $C_2 = 1\,\mathrm{nF}$ are the nominal values of the capacitors used in the setup. At cryogenic temperatures the values of C_1 and C_2 can differ from the nominal values. Furthermore, as C_1 is quite small ($2.5\,\mathrm{pF}$), the actual capacitance can be higher due to additional capacitance from the wires and the rest of the circuit. Therefore equation (6.5) gives only a rough estimate of the ratio $V_{\mathrm{RF}}/V_{\mathrm{cd}}$.

This ratio was determined more precisely by the following procedure: The radial trap frequencies were calculated as a function of the RF-voltage with a simulation of the trap in the *electrode package*. For 5 different RF-voltages the radial frequencies of a trapped ion were measured by sideband spectroscopy with the $729\,\mathrm{nm}$ laser. The measured data and the simulations are plotted together in figure 6.9 and are discussed later in this section. To compare the simulation with the measurement, the applied DC-voltages have to be included in the simulation. It is explained in the following that these DC-voltages are not directly the voltages on the electrodes.

The experiment is started with DC-voltages obtained from the simulation overlapping the ion's position with the RF-minimum. However, stray electric fields in the experiment shift the ion away from the RF-minimum. With micromotion compensation methods (see section 2.4.5) these stray fields are compensated. As expected, the compensation does not depend on the applied RF-voltage and therefore the same DC-set DC-α was used during the measurements for all 5 RF-voltages. In our experiment this compensation was not done with ideal shim-voltages, i.e. the trapping frequencies were changed during the compensation process and therefore we had to measure DC-α with a multimeter[8] with an accuracy below 0.1 %.

[8] Keysight U1251B

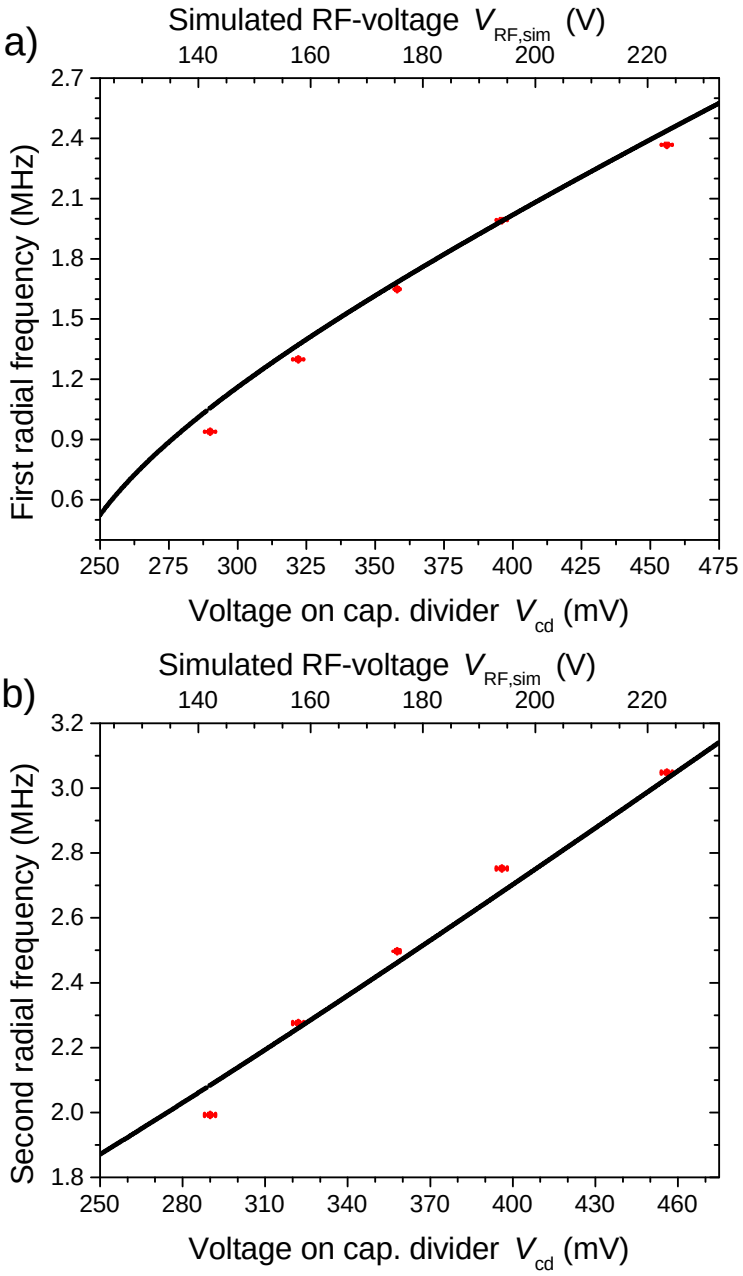

Figure 6.9: Measured radial frequencies compared to the simulated frequencies. In both graphs, the red points show the measured radial frequencies at the measured voltage on the capacitive divider V_{cd}, which is proportional to the amplitude of the RF-voltage V_{RF} on the trap. The black points belong to the upper horizontal axis and show the dependence of the radial frequencies on $V_{\mathrm{RF,sim}}$ obtained by a simulation of the trap with the *electrode package*. In **a)** the first radial frequency is displayed. The second, larger radial frequency is given in **b)**.

DC-set	1	2	3
ω_z (MHz)	1.050	0.822	1.135
$\vec{E}_\mathrm{s}$ (V/m)	$109 \cdot (-0.98, 0.02, 0.07)$	$112 \cdot (-0.99, 0.03, -0.12)$	$19 \cdot (0.06, 0.34, 0.94)$
Electrode	DC-voltage (V)		
TL	29.348	17.850	34.313
TM	-29.583	-18.179	-34.466
TR	29.269	17.805	34.178
BL	6.671	4.174	7.616
BM	-29.230	-17.762	-34.197
BR	6.633	4.154	7.290
C	0.905	0.484	1.255

Table 6.2: DC-sets for the simulations corresponding to DC-β, the corresponding simulated axial frequency ω_z and the calculated electric stray field $\vec{E}_\mathrm{s}$ given in magnitude times orientation. DC-set 1 was used for the calibration of the capacitive divider in section 6.3.1, where we varied the RF-voltage while keeping the same set of DC-voltages. All three sets were used for comparing the secular frequencies from the simulation with the experiment in section 6.3.2, where the RF-voltage was kept constant and the three different sets of DC-voltages were used to obtain the secular frequencies. We did not observe drifts in the stray electric field during a day. However, the difference between the stray electric field between the measurements for the different DC-sets could result from changing stray electric fields as the measurements were done on different days.

The stray fields are not present in the simulation and therefore in a simulation with DC-α the trapping position was shifted about $1.3\,\mu\mathrm{m}$ away from the RF-minimum. This can be corrected by including an offset field in the simulation shifting the trapping position into the RF-minimum. The secular frequencies obtained in a simulation including the offset field differ from the ones without offset field by several tens of kHz (up to about 7 %) due to the anharmonicity of the RF-pseudopotential. This is in the same order of magnitude as the deviation between simulation and experiment which we discuss in the following section and shows the importance of including the offset field in the simulation.

Technically we produced the offset field in the simulation by calculating ideal shim voltages at the trapping position obtained from a simulation with DC-α (see section 4.3.2). DC-β is then the sum of DC-α and the applied shim-voltages. The electric field from the shim-voltages at the ion's position corresponds to the strength of the offset stray electric field in the experiment. For the measurements in this section it was $\vec{E}_\mathrm{s} = 109 \cdot (-0.98, 0.02, 0.07)\,\mathrm{V/m}$. As expected, it points dominantly in the x-direction orthogonal to the trap surface, because the closest surface to the ion is the trap underneath the ion.

The DC-set DC-β used for the simulation for the plots in figure 6.9 is given as DC-set 1 in table 6.2. The two plots show the measured trapping frequencies for 5 different voltages V_cd corresponding to 5 different RF-voltages. The peak-to-peak voltage on the capacitive divider was measured with an oscilloscope and was divided by two such that V_cd corresponds to the amplitude of that voltage. In both plots the simulated trapping frequencies are given as a function of the simulated RF-voltage $V_\mathrm{RF,sim}$. The relation between the RF-voltage on the trap V_RF and the voltage on the capacitive divider V_cd is

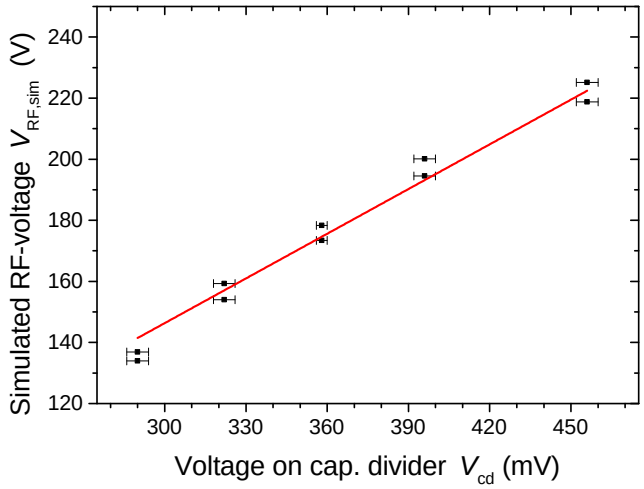

Figure 6.10: The voltage on the capacitive divider versus the simulated RF-voltage based on the data presented in figure 6.9. Each measured voltage V_{cd} in this figure was assigned a voltage $V_{\mathrm{RF,sim}}$ by looking up which voltage $V_{\mathrm{RF,sim}}$ corresponds to the measured radial frequency. The red line is a linear fit of the data with $V_{\mathrm{RF,sim}} = 490(6)V_{\mathrm{cd}}$.

given by $c = V_{\mathrm{RF}}/V_{\mathrm{cd}}$. It was determined by finding the constant c that leads to the best agreement between the simulated secular frequencies and the experimental data-points:

$$c = 490(6), \tag{6.6}$$

where the estimated error was obtained in the following way: Each measured voltage V_{cd} in figure 6.9 was assigned a voltage $V_{\mathrm{RF,sim}}$ by looking up which voltage $V_{\mathrm{RF,sim}}$ corresponds to the measured radial frequency. A linear fit of these data points estimates the error in equation 6.6 (see figure 6.10). The with $V_{\mathrm{RF}} = cV_{\mathrm{cd}}$ calculated RF-voltages differ from the datapoints in figure 6.10 by maximal $8\,\mathrm{V}$ (up to about $6\,\%$).

6.3.2 Comparison of simulated and measured trap frequencies

Testing the agreement between simulation and experiment for the five different RF-voltages in the previous section is influenced by our method of determining the RF-voltage on the trap, because determining c minimised possible deviations between simulation and experiment. Therefore in this section, we present the measurements of the trapping frequencies for three different sets of DC-voltages with the same RF-voltage and discuss the deviation between simulation and experiment for these measurements. Especially the deviation in the axial frequencies is of great interest, because the axial frequencies are not affected by the RF-voltage and therefore the deviation is not influenced by our method of determining the RF-voltage on the trap.

The three different DC-voltage sets are given in table 6.2. The simulated and the measured trapping frequencies are presented in table 6.3. Within the error bars the simulation shows good agreement with the measurements. The maximum deviation in the radial fre-

DC-set		ω_z (MHz)	ω_{r1} (MHz)	ω_{r2} (MHz)
1	Experiment	0.824(1)	1.871(1)	2.362(1)
	Simulation	0.822	1.92(6)	2.38(5)
	Difference	**0.002(1)**	**-0.05(6)**	**-0.02(5)**
2	Experiment	1.056(1)	1.648(1)	2.497(2)
	Simulation	1.050	1.68(7)	2.46(5)
	Difference	**0.006(1)**	**-0.04(7)**	**0.03(5)**
3	Experiment	1.135(1)	1.466(1)	2.498(1)
	Simulation	1.135	1.58(7)	2.50(5)
	Difference	**0.000(1)**	**-0.11(7)**	**0.00(5)**

Table 6.3: Simulated and measured trapping frequencies for 3 DC-voltage sets given in table 6.2. The *electrode package* was used for the simulations. The measurement was done with sideband spectroscopy on the $S_{1/2}$ to $D_{1/2}$ transition with a $729\,\mathrm{nm}$ laser. The error estimation in the simulated radial frequencies results from the uncertainty of the RF-voltage calculated with equation (6.6) ($V_{\mathrm{RF}} = 175(4)\,\mathrm{V}$). The axial frequency ω_z depends only on the DC-voltages and not on the RF-voltage. The DC-voltages were measured with a multimeter with an accuracy below 0.1 % and the corresponding voltage set DC-β was obtained with the *electrode package*. That is why no error bars are assigned to the simulation results for ω_z.

quencies is $0.11(7)\,\mathrm{MHz}$ corresponding to a relative error of 7 %. The deviation in the axial frequency ω_z is below 0.6 %.

Including the results from the previous section it can be summarized that the maximum relative deviation in the radial frequencies is 11 % and the average deviation is 3 %. The axial frequencies show an excellent agreement to within 0.6 %. The difference in the agreement can be explained by the fact that the DC-voltages are known with higher precision than the RF-voltage.

In [58], it is claimed that the error in simulating the trapping frequencies of surface-electrode ion traps produced by the gapless plane approximation under realistic conditions is in the worst cases up to 5 %. In the same paper R. Schmied derives higher order corrections of the simulation to reduce these errors.

Based on this, we expect that the deviation in the radial frequencies is mainly caused by stray fields. Taking the agreement in the axial frequencies into account, additional measurements and a more precise simulation need to be done in order to determine if the deviation results from stray fields or from simulation errors.

The agreement in the radial frequencies is comparable to the observations made by C. Hempel. He reported in his PhD thesis a deviation of 8 % between simulations with finite element method (FEM) and measurements of trapping frequencies in a blade design ion trap with an ion-electrode separation of $565\,\mu\mathrm{m}$ [74].

U. Warring et al. measured the trapping frequencies in a surface-electrode ion trap with an ion-electrode separation of $30\,\mu\mathrm{m}$ and compared it to a simulation of the trap using the gapless plane approximation [75]. They reported stray fields with a curvature of approximately $10^7\,\mathrm{V/m^2}$ leading to a complete mismatch of the measured trapping frequencies with the simulation, the stray field resulted in an axial frequency of about $1.4\,\mathrm{MHz}$ without applying DC-voltages [76]. After including these stray fields in the

simulations, an agreement to within 10 % was found. To compare these results with our measurements, the smaller ion-electrode separation must be taken into account. U. Warring et al. model the measured stray fields with a rectangular patch that is biased to $-1.15\,\mathrm{V}$. Its size is $\delta z = 35\,\mu\mathrm{m}$ and $\delta x = 5\,\mu\mathrm{m}$ and it is located on the chip surface with the patch centre displaced by $z = 3\,\mu\mathrm{m}$ and $x = -35\,\mu\mathrm{m}$ relative to the trap centre. At the ion-electrode separation of the HTCYK1-trap ($226\,\mu\mathrm{m}$) this patch produces a curvature of approximately $10^4\,\mathrm{V/m^2}$. This would shift a trapping frequency of $1\,\mathrm{MHz}$ by $2\,\mathrm{kHz}$ which has the same order of magnitude as the deviation in the axial frequencies in HTCYK1.

In summary, we expect that the deviation in the radial frequencies is mainly caused by stray fields. The origin of the deviation in the axial frequencies can not be determined from our measurement. It can either result from stray fields or from the limited accuracy of the simulation. However, the excellent agreement of the axial frequencies within 0.6 % motivates to further investigate differences between simulation and experiment in the YBCO-traps.

6.4 Heating rate measurements

We performed heating rate measurements with the ratio method on two YBCO-traps. We tested the HTCYK1-trap which was used for the measurements of the trapping frequencies described in the previous section. The result is presented in section 6.4.1. The measurements on a two-meander trap are discussed in 6.4.2.

The heating rate measurements were performed in the following way. First an ion was trapped and the micromotion was minimised by the methods described in section 2.4.5. We optimised the detuning and the pulse length for Doppler cooling (section 2.4.2) and sideband cooling (section 2.4.3). After cooling the ion close to the ground state, the mean phonon number $\bar{n}$ was determined by red and blue sideband pulses on the $729\,\mathrm{nm}$ transition as described in section 3.3. Different waiting times t_{wt} were included between ground state cooling and measuring $\bar{n}$. The heating rate Γ_{h} was obtained from a linear fit of the data. An example is shown in figure 6.11.

6.4.1 Trap without meander structures

The HTCYK1-trap was installed on a standard trap mount, which is not thermally decoupled from the coldhead of the cryostat and does not have local heaters (see [29]). The heating rate measurement was performed at $T = 10(2)\,\mathrm{K}$ determined with the temperature sensor mounted on the copper carrier. The accuracy is therefore limited by the sensor and the small residual temperature gradients in the copper carrier. The heating rate measurement is shown in figure 6.11 and leads to

$$\begin{aligned} & \Gamma_{\mathrm{h}} = 0.29(4)\,\mathrm{phonons/s} \\ \text{at} \quad & T = 10(2)\,\mathrm{K} \\ \text{and} \quad & \omega_z = 2\pi \cdot 1.056\,\mathrm{MHz}. \end{aligned} \tag{6.7}$$

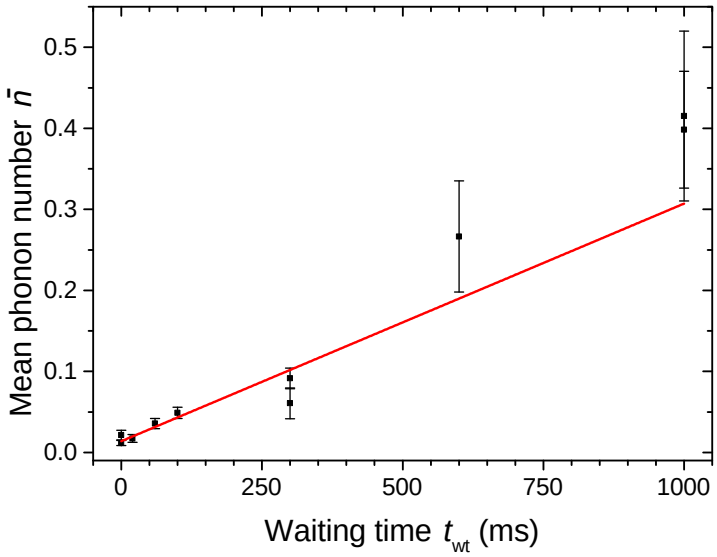

Figure 6.11: Heating rate measurement with the HTCYK1-trap. The mean phonon number $\bar{n}$ was determined with the ratio method (section 3.3) for different waiting times. $\Gamma_\mathrm{h} = 0.29(4)\,\mathrm{phonons/s}$ is given by the slope of the linear fit through the data points.

This heating rate is slightly below the lowest heating rates of the silicon traps with almost the same trap design ($\Gamma_\mathrm{h} = 0.33(4)\,\mathrm{phonons/s}$) [45]. It is the lowest heating rate ever reported in our lab for a chip with a $226\,\mu\mathrm{m}$ ion-electrode distance, at $\omega_z \approx 2\pi \cdot 1\,\mathrm{MHz}$. More YBCO-traps have to be tested before drawing detailed conclusions. It has to be noted, that the surface of this YBCO-trap is covered with gold. Nevertheless, it is a promising result for further investigations of YBCO as a trap material.

6.4.2 Two-meander design

The results presented in this section were obtained with a two-meander design trap (see section 4.5.2). In the two-meander design the meander-electrodes are symmetric with respect to the trapping position. When the trap is operated above T_c it is expected that an RF-pickup voltage is present on the meander-electrodes (see section 4.4.3). Due to the symmetry of the design the electric field from the RF-pickup should have a minimum at the trapping position. Therefore it is expected that it does not prevent compensation of the micromotion.

The trap was installed on the variable-temperature trap mount (see section 5.3). A picture of the bonded trap is shown in figure 6.5 on page 68. The two middle-sized meanders were connected to the two meander-electrodes and therefore the heating rate is expected to be around $\Gamma_\mathrm{h} \approx 2 \times 10^3\,\mathrm{phonons/s}$ at $T = 100\,\mathrm{K}$ (see table 4.4). Another meander of the same size on the upper part of the chip was connected to the multimeter for the 4-wire measurement. After one week of trap operation, the meander used for the 4-wire measurement was not conducting current anymore. The possible reasons for that are discussed later in this section. Furthermore, during the trap operation, an electrical short to

T (K)	ω_z (MHz)	Γ_h (phonons/s)
12(3)	0.9417	1.8(1)
12(3)	0.8769	3.1(3)
75(10)	0.9257	7.2(6)

Table 6.4: Result of heating rate measurements on the two-meander design at temperature T and axial frequency ω_z. The results are discussed in the main text.

ground with variable resistance to ground was found in the connection of the temperature sensor. This short and the failed meander are the reasons why the temperature for the following measurements could only be estimated by observing the phase transition in the resonator and by using the second temperature sensor on the copper carrier (see section 5.3.1). The results can be seen as preliminary measurements and will be redone with a working temperature sensor.

For $T < T_c$ three heating rate measurements were performed and the results are given in table 6.4. The two heating rate measurements at $T = 12(3)\,\mathrm{K}$ showed an average heating rate $\Gamma_h = 2.5(2)\,\mathrm{phonons/s}$ for $\omega_z \approx 0.9\,\mathrm{MHz}$. This is an order of magnitude higher than the heating rate in the HTCYK1-trap. The difference can not be explained by the meander-electrodes, because below T_c it was verified that the YBCO-meander structure is in the superconducting state $R = 0$ (see section 6.1.1). As Johnson noise is proportional to the resistance R, the meander-structures should not affect the heating rate for $T < T_c$. It is rather expected that the higher heating rate is due to fluctuations from trap to trap. It is comparable to the fluctuations between $0.33(4)\,\mathrm{phonons/s}$ and $3.3(2)\,\mathrm{phonons/s}$ that were reported for the silicon traps [45].

The measurement at $T = 75(10)\,\mathrm{K}$ showed $\Gamma_h = 7.2(6)\,\mathrm{phonons/s}$. This correspond to an increase by a factor of 3 from $12(3)\,\mathrm{K}$ to $75(10)\,\mathrm{K}$. This increase agrees with the results reported in [61, 62].

The trap was operated above T_c at $T \approx 100\,\mathrm{K}$. It was possible to load and trap an ion at this temperature. It was also possible to load an ion at $12\,\mathrm{K}$ and keep it while warming up the trap to $T \approx 100\,\mathrm{K}$ using the local heater. However, RF-pickup on the meander-electrodes caused additional micromotion at $T \approx 100\,\mathrm{K}$. From the simulation of the two-meander design it was expected that the micromotion should be fully compensable at the point where the RF-minimum from the RF-pickup and the RF-minimum from the RF-electrodes are overlapping. In the experiment a minimum of the micromotion was found along the trap axis. However, it was not possible to fully compensate the micromotion. This can have the following reasons: The RF-minima may not overlap completely due to limited accuracy of the simulations or due to microfabrication tolerances. The RF-pickup on the two meander-electrodes could have a different phase and a different amplitude due to temperature gradients on the chip or microfabrication tolerances that break the symmetry of the trap design.

During the trap operation at $T \approx 100\,\mathrm{K}$, we were not able to achieve ground state cooling. This could be explained by the following: The residual micromotion reduces the cooling efficiency of Doppler- and Sideband-cooling. Furthermore, due to Johnson-noise produced by the meanders, the heating rate is significantly higher than below T_c. It is expected to be $\Gamma_h \approx 2 \times 10^3\,\mathrm{phonons/s}$ at $T = 100\,\mathrm{K}$ (see table 4.4). The lowest achiev-

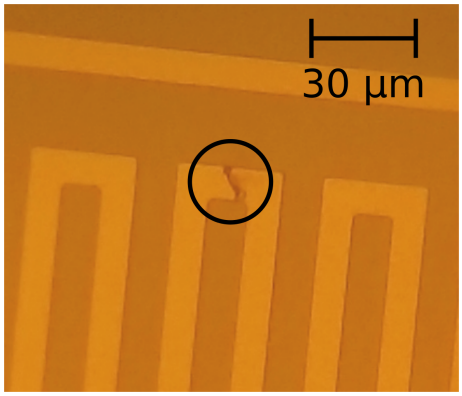

Figure 6.12: Damage in the test meander structure apparent as the dark region across the meander inside the black circle. The small gap could have been produced by a high current pulse that "burned" the meander-structure at a weak point.

able phonon number was $\bar{n} = 15(7)\,\mathrm{phonons}$. This phonon number creates huge error bars in the determination of $\bar{n}$ and the informative value of a heating rate measurement would have been very little. The Doppler recooling method would enable one to measure heating rates without ground state cooling [17]. However, it is not suitable for our project, because it does not resolve the motional sidebands. Therefore it can not be determined if the heating rate is due to heating in the axial mode or in the other modes. Furthermore it would prevent from measuring the frequency scaling of the noise.

Consequently, it was decided to take out the trap, fix the issues with the temperature sensor and change the meander size for the meander-electrode. Additionally, another meander on the upper part of the chip has to be connected for the 4-wire measurement to replace the meander with the failure.

Taking out the trap enabled us to make a picture of the meander failure shown in figure 6.12. The cause of the failure is unknown. It could have been caused by a high current pulse produced by the multimeter exceeding the critical current at the weakest point of the meander-structure and creating a small gap in the meander. The reason for that current pulse is not determined yet and will be investigated in the future.

Next steps

The measurements with the two-meander trap presented above were the last measurements of this thesis. They show that the heating rate in the two-meander trap is comparable to the low heating rates observed in the silicon traps [45]. For the measurements on the two-meander trap, the middle sized meander out of three different meander sizes was connected to the meander-electrodes. The smallest meander size is by a factor 3 shorter than the middle sized meander. The heating rate from the smallest meander is expected to be around $8.4 \times 10^2\,\mathrm{phonons/s}$ at $T = 100\,\mathrm{K}$ (see table 4.4) and therefore by two orders of magnitude higher than the measured Γ_h below T_c. The smaller resistance of the smallest meander should reduce the RF-pickup voltage (see section 4.4.3). The next step will be to try to perform heating rate measurements above T_c with a two-meander trap and the smallest meander size. If it is still not possible to ground state cool the ion, a bypass ca-

pacitor can be added to further reduce the RF-pickup voltage on the meander-electrodes.

Chapter 7

Summary and Outlook

The aim of the YBCO-project is to investigate the characteristics of the electric field noise produced by Johnson noise and compare it to the characteristics of the electric field noise from unknown sources, possibly from the trap surface near the ion. In this way it should be possible to improve the understanding of anomalous heating in ion traps. The project was started with the work described in this Master's thesis.

The high-temperature superconductor YBCO was chosen as a trap electrode material to enable the characterisation of Johnson noise and anomalous heating in the same trap. Below the critical temperature T_c, the resistance of YBCO vanishes. Therefore Johnson noise is negligibly small compared to anomalous heating and allows to investigate anomalous heating. Above T_c, we want to characterise Johnson noise. Two different designs were made, both ensuring that Johnson noise is the dominant source of motional heating above T_c. The Yedikule-3 design from M. Niedermayr's PhD thesis was taken as a basis for the new designs [29]. Based on the heating rate measurements on the Yedikule-3 silicon and silica traps and the temperature dependence of heating rates reported in [61, 62], we estimated the motional heating in the YBCO-traps around T_c. Additionally, we simulated the electric field noise produced by Johnson noise from one DC-electrode. This allowed us to calculate that in the adapted Yedikule-3 design, the HTCYK1, the required resistance to make Johnson noise dominant above T_c is $R \approx 1\,\mathrm{M\Omega}$. It was shown that if such a high resistance is connected to a DC-electrode, it prevents from RF-grounding the DC-electrode. Consequently, an RF-pickup voltage on the DC-electrode can cause non-compensable micromotion or prevent from trapping an ion. Therefore the HTCYK1 was modified in a way to reduce the required resistance R. In the one-meander design R was reduced by approximately a factor of 42 and in the two-meander design by approximately a factor of 17. The two-meander design minimises the effects of RF-pickup voltages on the meander-electrodes by overlapping the RF-minimum of the pickup voltages with the RF-minimum of the trap. Additional means to reduce the RF-pickup voltage by a bypass capacitor or a second RF signal were presented.

The existing cryogenic setup cannot be operated at variable temperatures. Therefore a new trap mount was built. It consists of a trap stage made of copper and two PEEK carriers that thermally decouple the trap stage from the surrounding setup cooled by the cryostat. The temperature of the trap T_trap can be varied with a local heater consisting of resistors glued to the trap stage. T_trap can be measured with a sensor placed on the

trap stage. It was possible to heat up the trap stage from $10\,\mathrm{K}$ to $238\,\mathrm{K}$ while keeping the temperature of the surrounding setup below $11\,\mathrm{K}$. This thermal decoupling ensures that the filterboard for the DC-electrodes and the resonator circuit stay at cold temperatures and their properties are not affected by the temperature changes of the trap stage.

Furthermore, a 4-wire resistance measurement of a meander-structure on the trap-chip was integrated in the experimental setup. This resistance measurement, together with the temperature and the pressure are logged using a LabVIEW program. This enabled us to verify that the YBCO-traps are in the superconducting state below T_c. We were able to determine that $T_\mathrm{c} = (85.4 \pm 0.2 \pm 1)\,\mathrm{K}$. Additionally, the 4-wire measurement gives us the resistance of the YBCO-meander structure above T_c allowing us to calculate the expected magnitude of Johnson noise.

The traps were installed on the trap mount by glueing them onto the trap stage with varnish. The thermal conductivity between the trap stage and the trap was increased by adding 90 bonding wires between the trap stage and the trap. However, when the local heater was used to heat the trap stage, we observed a temperature difference of a few kelvin between the trap stage and the trap. To measure the trap temperature precisely, a correction method for the trap stage temperature sensor was presented. It uses the results of the 4-wire resistance measurements and allows to measure T_trap with an accuracy of $1\,\mathrm{K}$.

The simulation of the traps for this project were performed with the *electrode package*. It uses the infinite plain and the gapless approximation. Consequently, it is of great interest to compare the simulations with experimental measurements. We measured the secular frequencies for different RF- and DC-voltages in a HTCYK1 trap by sideband spectroscopy of the $S_{1/2}$ to $D_{5/2}$ transition on a trapped $^{40}Ca^{+}$-ion. The measured radial frequency have an average deviation from the simulations of 3 %. The axial frequencies show an excellent agreement within 0.6 %. We expect that the deviations result from electric stray fields in the setup, but further investigations are necessary to verify this assumption.

Finally, heating rate measurements were performed in a HTCYK1 trap and a two-meander trap. The heating rate in the HTCYK1 trap was $\Gamma_\mathrm{h} = 0.29(4)\,\mathrm{phonons/s}$ at $T = 10(2)\,\mathrm{K}$ and $\omega_z = 2\pi \cdot 1.056\,\mathrm{MHz}$. In the two-meander trap $\Gamma_\mathrm{h} \approx 2\,\mathrm{phonons/s}$ at $T = 12(2)\,\mathrm{K}$ and $\omega_z \approx 2\pi \cdot 0.9\,\mathrm{MHz}$. The results are comparable to the heating rates measured in the silicon traps and therefore they are among the lowest heating rates reported in the literature [45].

In the two-meander trap it was possible to keep a trapped ion while the temperature of the trap was increased above T_c. However, it was not possible to cool the ion to the ground state above T_c preventing us from performing heating rate measurements. This can be due to a combination between the non-compensable micromotion that reduces the cooling efficiency and the high heating rate produced by Johnson noise from the meanders.

For the measurements on the two-meander trap, the middle sized meander out of three different meander sizes was connected to the meander-electrodes. The smallest meander size is by a factor 3 shorter than the middle sized meander. The heating rate from the smallest meander is expected to be around $8.4 \times 10^2\,\mathrm{phonons/s}$ at $T = 100\,\mathrm{K}$. Based on the performed heating rate measurements below T_c, it is expected that Johnson noise is dominant above T_c with the smallest meander size. The next step in this project will be to

suppress the micromotion above T_c. It will be first tested if the smallest meander size on the trap reduces the pickup voltage enough to better compensate micromotion and cool the ion to the ground state. Additionally, a bypass capacitor may be used to further reduce the pickup voltage if necessary. Furthermore, new YBCO-traps with a thicker YBCO-film will be ordered to reduce the resistance of the meanders. With these means it should be possible to perform heating rate measurements above T_c and investigate the effects of Johnson noise.

Besides that, the already fabricated wafer contains traps, where the gold layer is completely removed underneath the trapping position of the ion. Consequently, it will be possible to examine the surface noise characteristics of YBCO to find out if they differ from the noise characteristics of other ion trap materials.

Appendix A

Capacitive coupling C_{C} between the RF-electrode and the TM-electrode

The RF-grounding of the TM-electrode is analysed in section 4.4.3. In this example it is discussed how the meander connected to the TM-electrode affects the RF-grounding of this electrode. To perform this calculation, the capacitive coupling C_{C} between the RF-electrode and the TM-electrode is approximated in this chapter.

A.1 Lower bound estimate

The lower bound $C_{\mathrm{C}} > 0.03\,\mathrm{pF}$ is calculated with the *electrode package* in the following way: The RF-electrode and the TM-electrode are defined such that they are separated by the gap size ($10\,\mu\mathrm{m}$). The voltage on the RF-electrode is set to $1\,\mathrm{V}$. The electric field $\vec{E}(x,z)$ on the surface[1] of the TM-electrode is calculated with *System.individual_potential*. The induced charge Q on the TM-electrode is then given by [77]

$$Q = \epsilon_{\mathrm{r}}\epsilon_0 \oint_S \vec{E}(x,z)\vec{n_z}da, \tag{A.1}$$

where the integral is taken over the whole surface of the electrode S, $\vec{e_y}$ is the unity vector orthogonal to the surface, ϵ_0 is the vacuum permittivity and $\epsilon_{\mathrm{r}} \approx 10$ is the relative permittivity of sapphire. In the *electrode package* the $10\,\mu\mathrm{m}$ space between the electrodes is grounded and shields the two electrodes from each other. Therefore a numerical calculation with equation (A.1) gives a lower bound for Q. The lower bound for C_{C} is then given by

$$C_{\mathrm{C}} = \frac{Q}{U}, \tag{A.2}$$

where $U = 1\,\mathrm{V}$ is the voltage difference between the RF-electrode and the TM-electrode.

[1] In the *electrode package* it is not possible to calculate the electric field directly on the surface. Therefore it was calculated $10^{-5}\,\mu\mathrm{m}$ above the surface. The height was chosen after going closer and closer to the surface until no further difference was observed within 11 siginifact digits.

A.2 Upper bound estimate

The upper bound is obtained by estimating the fraction $C_{\mathrm{C}}/C_{\mathrm{trap}}$, where C_{trap} is the capacitance between the RF-electrode and the rest of the trap surface. C_{trap} can be approximated by

$$C_{\mathrm{trap}} \approx C_{\mathrm{resonator}} - C_{\mathrm{cd}}, \tag{A.3}$$

where $C_{\mathrm{resonator}} \approx 13\,\mathrm{pf}$ is the capacitance in the RLC resonant circuit (see section 5.2) and $C_{\mathrm{cd}} = 2.5\,\mathrm{pf}$ is capacitance to ground from the capacitive divider. From the geometry of the trap (see figure 4.4) it can be seen that $C_{\mathrm{C}}/C_{\mathrm{trap}} < 1/20$. This leads the upper bound $C_{\mathrm{C}} < 0.5\,\mathrm{pF}$.

Appendix B

Radiative heat transfer between the trap and the surrounding setup

In section 6.2.1 the temperature difference between the trap stage and the trap is discussed. The relevant thermal connections are given in figure 6.4. In this appendix it is verified that radiative heat transfer between the trap and the surrounding setup can be neglected.

The radiative heat transfer W_{rad} between two surfaces is given by [53]

$$W_{\mathrm{rad}} = \sigma E A (T_2^4 - T_1^4),$$

where $\sigma = 5.7 \times 10^{-8}\,\mathrm{W}/(\mathrm{m}^2\mathrm{K}^4)$ is the Stefan-Boltzmann constant, E is a material dependent factor, A is the surface area of the smaller surface from the two given surfaces and T_2 and T_1 are the temperatures of the two surfaces. If one of the surfaces is highly reflective like e.g. metal, than $E \ll 1$. The trap is covered by highly reflective gold and it has a surface area of about $A \approx 1\,\mathrm{cm}^2$. For a heated trap with $T_2 \approx 100\,\mathrm{K}$ and a cold surrounding setup with $T_1 \approx 100\,\mathrm{K}$, the radiative heat transfer is

$$W_{\mathrm{rad}} \ll 10^{-7}\,\mathrm{W}.$$

The required power to heat up the trap stage to $100\,\mathrm{K}$ is around $100\,\mathrm{mW}$ (see section 5.3.2). Therefore the radiative heat transfer can be neglected.

Appendix C

Ipython code for trap simulations

In this section an example code for simulating an ion trap with the electrode package is provided. In this code the trap layout of HTCYK1 is used. The coordinate system in the *electrode package* (x_e, y_e, z_e) is defined such that x_e and y_e span the plane of the trap surface and z_e gives the height over the surface. In the presentation of the results in section 4.3.3 a different coordinate system (x_r, y_r, z_r) was used to follow the convention that z_r points along the trap axis. Additionally, the origin of x_r and y_r was shifted so that it coincides with the ion position. The relation of the two coordinate systems is given by

$$\begin{aligned} x_\mathrm{r} &= y_\mathrm{e} - 166\,\mu\mathrm{m} \\ y_\mathrm{r} &= z_\mathrm{e} \\ z_\mathrm{r} &= x_\mathrm{e}. \end{aligned}$$

The code is presented as it appears in Ipython notebook [78]. It is split into several blocks which are computed one after another. In the following every block starts with "In []:".

```
In [ ]: import matplotlib.pyplot as plt, numpy as np, scipy.constants as ct
        from __future__ import division
        from electrode import (System, PolygonPixelElectrode, euler_matrix,
            PointPixelElectrode, PotentialObjective,
            PatternRangeConstraint, shaped)

        np.set_printoptions(precision=4) # have numpy print fewer digits

        %pylab inline

In [ ]: # Global definition of trap parameters. Used for all cells in this notebook

        L = 1e-6 # µm length scale
        Vrf = 176. # RF peak voltage in V
        M = 40*ct.atomic_mass # ion mass
        Q = 1*ct.elementary_charge # ion charge
        Omega = 2*np.pi*18.97e6 # RF frequency in rad/s

        # RF voltage in parametrized form so that the resulting potential equals the RF pseudopotential in eV
        Urf = Vrf*np.sqrt(Q/M)/(2*L*Omega)

        # GND cover plane above trap
        c_height=1000*L
        c_switch=0 # set to "0" to switch effect of cover_plane off, "2" to switch it on

In [ ]: # First the electrode layout is defined. Pay attention that the direction matters in this case.
```

```
        def trap(dcwidth, dclength, centertop ,rfbottom, rftop):
            dcw, dcl, ct, rb, rt,  = dcwidth, dclength,  centertop , rfbottom, rftop
            electrodes =[
                        ("rf", [[(-3830, 465), (3830, 465), (3830, ct), (-3830, ct)],
                                 [(-3830, ct), (-3315, ct), (-3315, -5), (+3315, -5),
                                  (3315, ct), (3830, ct), (3830, rb), (-3830, rb)]]),
                        ("tl", [[(-3/2*dcw, rt+dcl), (-3/2*dcw, rt), (-1/2*dcw, rt), (-1/2*dcw, rt+dcl)]]),
                        ("tm", [[(-1/2*dcw, rt+dcl), (-1/2*dcw, rt), (1/2*dcw, rt), (1/2*dcw, rt+dcl)]]),
                        ("tr", [[(1/2*dcw, rt+dcl), (1/2*dcw, rt), (3/2*dcw, rt), (3/2*dcw, rt+dcl)]]),
                        ("bl", [[(-3/2*dcw, rb), (-3/2*dcw, -dcl+rb), (-1/2*dcw, -dcl+rb), (-1/2*dcw, rb)]]),
                        ("bm", [[(-1/2*dcw, rb), (-1/2*dcw, -dcl+rb), (1/2*dcw, -dcl+rb), (1/2*dcw, rb)]]),
                        ("br", [[(1/2*dcw, rb), (1/2*dcw, -dcl+rb), (3/2*dcw, -dcl+rb), (3/2*dcw, rb)]]),
                        ("c", [[(-3315, -5),(3315, -5),(3315, ct),(-3315, ct)]])
                        ]
            s = System([PolygonPixelElectrode(name=n, paths=map(np.array, p))
                        for n, p in electrodes])

            #Initialize the type of voltages (rf for RF voltages and dc for DC voltages) and set the voltages
            #In this example the DC-voltages are not set yet, because they are determined later
            s["rf"].rf = Urf
            s["tl"].dc = 0.
            s["tm"].dc = 0.
            s["tr"].dc = 0.
            s["bl"].dc = 0.
            s["bm"].dc = 0.
            s["br"].dc = 0.
            s["c"].dc = 0.
            return s

In [ ]: #Generate the trap layout
        s = trap(360., 2995., 255., -415., 465.)

        #Plot the electrodes
        fig, ax = plt.subplots(1, 3, figsize=(30, 30))
        s.plot(ax[0])

        s.plot_voltages(ax[1], u=s.rfs)
        #u = s.rfs sets the voltage-type for the voltage plot to RF-voltages (DC are not shown)
        s.plot_voltages(ax[2], u=s.dcs)
        #u = s.dcs sets the voltage-type for the voltage plot to DC-voltages (RF are not shown)

        xmax = 4000
        ymaxn = 4000
        ymaxp = 4000

        ax[0].set_title("colour")
        # ax[0] addresses the first plot in the subplots - set_title gives this plot a title
        ax[1].set_title("rf-voltages")
        ax[2].set_title("dc-voltages")

        for axi in ax.flat:
            axi.set_aspect("equal")
            axi.set_xlim(-xmax, xmax)
            axi.set_ylim(-ymaxn, ymaxp)

In [ ]: # Determine the RF minimum
        x0 = s.minimum((0., 165.9, 225.), axis=(0, 1, 2), coord=np.identity(3), method="Newton-CG")
        print x0

In [ ]: # get secular frequencies  == pseudopotential modes
        try:
            curv_z, mod_dir=s.modes(x0,sorted=False)
            omega_sec = np.sqrt(Q*curv_z/M)/(L*2*np.pi) * 1e-6
            print "secular frequencies: (%.4g, %.4g, %.4g) MHz" % (omega_sec[0],omega_sec[1],omega_sec[2])
            print "in directions ", mod_dir
        except:
            print "secular frequencies not found"
```

```
In [ ]: #Plot the pseudopotential

        with s.with_voltages(dcs = 0*s.dcs, rfs = None):
            # in with_voltages, all electrodes have to be listed in an array
            # (the array for dcs also contains the RF electrode)

            # 2D plot settings
            n=100    # resolution of meshgrid = resolution of 2D plots
            xmin, xmax = -500, 500
            ymin, ymax = 0, 350
            zmin, zmax =  150, 400
            x_cut, y_cut, z_cut = x0[0], x0[1], x0[2]# position of the yz-, xz-, xy- crossection
            v = np.arange(0, 0.7, 0.05)# set the range for contour lines
            v_min, v_max = 0, 0.7# set the range for colour map (range in eV)

            fig = plt.figure()
            fig.set_size_inches(25,10)
            fs = 26
            ls = 23

            # z-x cross section
            ax1 = plt.subplot2grid((2,2), (0,0))
            ax1.set_title("z-x cross section" ,fontsize=fs)
            ax1.set_xlabel('z ($10^{-6}$m)',fontsize=fs)
            ax1.set_ylabel('x ($10^{-6}$m)',fontsize=fs)
            ax1.tick_params(axis='x', labelsize=ls)
            ax1.tick_params(axis='y', labelsize=ls)
            # np.mgrid returns a dense multi-dimensional "meshgrid".
            xyz = np.mgrid[xmin:xmax:1j*n, ymin:ymax:1j*n, z_cut:z_cut+1]
            pot = shaped(s.potential)(xyz)
            x, y, p = (_.reshape(n, n) for _ in (xyz[0], xyz[1], pot))
            CS=ax1.contour(x, y, p, v, cmap=plt.cm.hot)
            im = ax1.imshow(p.T, origin='lower', vmin=v_min, vmax=v_max, extent=(xmin,xmax,ymin,ymax))
            im.set_interpolation('bilinear')

            # z-y cross section
            ax2 = plt.subplot2grid((2,2), (1,0))
            ax2.set_title("z-y cross section " ,fontsize=fs)
            ax2.set_xlabel('z ($10^{-6}$m)',fontsize=fs)
            ax2.set_ylabel('y ($10^{-6}$m)',fontsize=fs)
            ax2.tick_params(axis='x', labelsize=ls)
            ax2.tick_params(axis='y', labelsize=ls)
            xyz = np.mgrid[xmin:xmax:1j*n, y_cut:y_cut+1, zmin:zmax:1j*n]
            pot = shaped(s.potential)(xyz)
            x, z, p = (_.reshape(n, n) for _ in (xyz[0], xyz[2], pot))
            CS=ax2.contour(x, z, p, v, cmap=plt.cm.hot)
            im = ax2.imshow(p.T, origin='lower', vmin=v_min, vmax=v_max, extent=(xmin,xmax,zmin,zmax))
            im.set_interpolation('bilinear')

            # x-y cross section
            ax3 = plt.subplot2grid((2,2), (0,1), rowspan=2)
            ax3.set_title("x-y cross section" ,fontsize=fs)
            ax3.set_xlabel('x ($10^{-6}$m)',fontsize=fs)
            ax3.set_ylabel('y ($10^{-6}$m)',fontsize=fs)
            ax3.tick_params(axis='x', labelsize=ls)
            ax3.tick_params(axis='y', labelsize=ls)
            xyz = np.mgrid[x_cut:x_cut+1, ymin:ymax:1j*n, zmin:zmax:1j*n]
            pot = shaped(s.potential)(xyz)
            x, z, p = (_.reshape(n, n) for _ in (xyz[1], xyz[2], pot))
            CS=ax3.contour(x, z, p, v, cmap=plt.cm.hot)
            im = ax3.imshow(p.T, origin='lower', vmin=v_min, vmax=v_max, extent=(ymin,ymax,zmin,zmax))
            im.set_interpolation('bilinear')

            # add a colorbar
            cb = fig.colorbar(im, ax=ax3, shrink=0.9)
            cb.ax.tick_params(labelsize=ls)
            cb.set_label('Potential energy (eV)', fontsize = fs)
```

```
            show()

In [ ]: # Determine proper DC voltages with the function shims

        # If it is not possible to DC bias the RF electrode,
        # then define a new system of electrodes s1 which excludes the RF-electrode
        s1 = System([e for e in s if not e.rf])

        # Give the constraints for system.shims
        derivs = "xx x y z ".split()

        u_cal = s1.shims((x0 , None, deriv) for deriv in derivs)

        # Define variables for confinement in x-direction (uxx) and shim voltage sets (ux,uy,uz)
        uxx = 1*np.array(u_cal[0])
        ux = 1*np.array(u_cal[1])
        uy = 1*np.array(u_cal[2])
        uz = 1*np.array(u_cal[3])

In [ ]: # Define the voltage set for confinement in x-direction
        u_set = 0.1805e-4*np.array([0 , uxx[0], uxx[1], uxx[2], uxx[3], uxx[4], uxx[5], uxx[6]])
        print u_set

In [ ]: # Apply the voltage set
        with s.with_voltages(dcs = u_set, rfs = None):

            # Check if the minimum was shifted
            x = s.minimum( (0., 165.9, 225.), axis=(0, 1, 2), coord=np.identity(3), method="Newton-CG")
            x_shift = x-x0
            print 'The minimum was shifted by: (%.3g, %.3g, %.3g)' % (x_shift[0], x_shift[1], x_shift[2])

            # Get trap frequencies
            try:
                curv_z, mod_dir=s.modes(x0,sorted=False)
                omega_sec=np.sqrt(Q*curv_z/M)/(L*2*np.pi) * 1e-6
                print "secular frequencies: (%.4g, %.4g, %.4g) MHz" % (omega_sec[0],omega_sec[1],omega_sec[2])
                print "in directions ", mod_dir
            except:
                print "secular frequencies not found"

In [ ]: # Plot the combined potential and pseudopotential

        with s.with_voltages(dcs = u_set, rfs = None):

            # 2D plot settings
            n=100    # resolution of meshgrid = resolution of 2D plots
            xmin, xmax = -500, 500      #set the plot ranges
            ymin, ymax = 0, 350
            zmin, zmax =  150, 400
            x_cut, y_cut, z_cut = x0[0], x0[1], x0[2]# position of the yz-, xz-, xy- crossection
            v = np.arange(0.3, 1.5, 0.05)# set the range for contour lines (range in eV)
            v_min, v_max = 0.4, 1.5# set the range for colour map (range in eV)
            fs = 26  #set the fontsize
            ls = 23  #set the labelsize

            fig = plt.figure()
            fig.set_size_inches(25,10)

            # z-x cross section
            ax1 = plt.subplot2grid((2,2), (0,0))
            ax1.set_title("z-x cross section" ,fontsize=fs)
            ax1.set_xlabel('z ($10^{-6}$m)',fontsize=fs)
            ax1.set_ylabel('x ($10^{-6}$m)',fontsize=fs)
            ax1.tick_params(axis='x', labelsize=ls)
            ax1.tick_params(axis='y', labelsize=ls)
            xyz = np.mgrid[xmin:xmax:1j*n, ymin:ymax:1j*n, z_cut:z_cut+1]
            pot = shaped(s.potential)(xyz)
```

```
            x, y, p = (_.reshape(n, n) for _ in (xyz[0], xyz[1], pot))
            CS=ax1.contour(x, y, p, v, cmap=plt.cm.hot)
            im = ax1.imshow(p.T, origin='lower', vmin=v_min, vmax=v_max, extent=(xmin,xmax,ymin,ymax))
            im.set_interpolation('bilinear')

            # z-y cross section
            ax2 = plt.subplot2grid((2,2), (1,0))
            ax2.set_title("z-y cross section " ,fontsize=fs)
            ax2.set_xlabel('z ($10^{-6}$m)',fontsize=fs)
            ax2.set_ylabel('y ($10^{-6}$m)',fontsize=fs)
            ax2.tick_params(axis='x', labelsize=ls)
            ax2.tick_params(axis='y', labelsize=ls)
            xyz = np.mgrid[xmin:xmax:1j*n, y_cut:y_cut+1, zmin:zmax:1j*n]
            pot = shaped(s.potential)(xyz)
            x, z, p = (_.reshape(n, n) for _ in (xyz[0], xyz[2], pot))
            CS=ax2.contour(x, z, p, v, cmap=plt.cm.hot)
            im = ax2.imshow(p.T, origin='lower', vmin=v_min, vmax=v_max, extent=(xmin,xmax,zmin,zmax))
            im.set_interpolation('bilinear')

            # x-y cross section
            ax3 = plt.subplot2grid((2,2), (0,1), rowspan=2)
            ax3.set_title("x-y cross section" ,fontsize=fs)
            ax3.set_xlabel('x ($10^{-6}$m)',fontsize=fs)
            ax3.set_ylabel('y ($10^{-6}$m)',fontsize=fs)
            ax3.tick_params(axis='x', labelsize=ls)
            ax3.tick_params(axis='y', labelsize=ls)
            xyz = np.mgrid[x_cut:x_cut+1, ymin:ymax:1j*n, zmin:zmax:1j*n]
            pot = shaped(s.potential)(xyz)
            x, z, p = (_.reshape(n, n) for _ in (xyz[1], xyz[2], pot))
            CS=ax3.contour(x, z, p, v, cmap=plt.cm.hot)
            im = ax3.imshow(p.T, origin='lower', vmin=v_min, vmax=v_max, extent=(ymin,ymax,zmin,zmax))
            im.set_interpolation('bilinear')

            # add colorbar
            cb = fig.colorbar(im, ax=ax3, shrink=0.9)
            cb.ax.tick_params(labelsize=ls)
            cb.set_label('Potential energy (eV)', fontsize = fs)

            show()
```

```
In [ ]: with s.with_voltages(dcs = u_set, rfs = None):

            # Get trap minimum
            try:
                x0 = s.minimum( (x0[0] , x0[1], x0[2]), axis=(0, 1, 2))
                p_tot0=s.potential(x0, 0)[0] #potential in the minimum
                print "potential minimum: %.4g" % p_tot0,"eV  at (%.3g, %.3g, %.3g)μm" % (x0[0],  x0[1],   x0[2])
            except:
                print " minimum not found"

            # Get saddle point
            try:
                # Here an approximate position of the saddle point has to be given; it can be seen in the plots
                xs, p_tots = s.saddle([x0[0], 90, 300])
                difference = p_tots-p_tot0
                print "saddle point: %.4g eV  at (%.3g, %.3g, %.3g)" % (p_tots, xs[0],xs[1],xs[2])
                print "Trap depth: %.4g eV" % (difference)
            except:
                print " saddle not found"

            # Plot a cross line through the saddle-point (xs) and the trap minimum (x0)

            # First create a vector through x0 and xs
            saddle_axe = xs - x0
            sa = saddle_axe
            # Calculate the length of the vector
            sa_modulus = np.sqrt((sa*sa).sum())
```

```
        # Initialize the vector
        # (the *1j is used to create the specified number of equidistant points)
        resolution = 1000 #set the resolution
        cross_line=np.mgrid[-1.:2.:resolution*1j]
        line_pot=np.copy(cross_line)

        # Get potential along this cross_line
        for i in range (0,resolution):
            x, y, z = x0[0] + cross_line[i]*sa[0], x0[1] + cross_line[i]*sa[1], x0[2] + cross_line[i]*sa[2]
            line_pot[i]=s.potential((x,y,z), 0)[0]

        # Plot the potential
        fig = plt.figure()
        fig.set_size_inches(12,5)
        ax = plt.subplot2grid((1,1), (0,0))
        ax.plot(cross_line*sa_modulus,line_pot, 'b',lw=5)
        max_vertical_size=abs( np.max(line_pot)-np.min(line_pot) )
        plt.axis([sa_modulus*cross_line[0], sa_modulus*cross_line[resolution-1], 0.4200, 0.55])
        plt.grid(b=True, which='both', color='0.25',linestyle='-')
        ax.set_xlabel('Distance from minimum ($10^{-6}$m)',fontsize=17)
        ax.set_ylabel('Potential (eV)',fontsize=17)
        ax.tick_params(axis='x', labelsize=15)
        ax.tick_params(axis='y', labelsize=15)
```

```
In [ ]: # Johnson_noise is calculated for T=100K and R = 1 Ohm
        T = 100.
        R = 1.
        kb = 1.3806488e-23  #Boltzmann constant

        # Choose an electrode (given by its number) -> the numbers start with 0
        e_number = 2
        # Choose the secular frequency -> the direction of the heating (given by its number)
        sf_number = 0

        # Define an axis along which you want to change the ion's postion:
        shuttle_axe = np.array([1., 0., 0.])
        sa = shuttle_axe

        # Define the distance over which you want to vary the position:
        shuttle_distance = 2000
        sd = shuttle_distance

        # Define the resolution
        resolution = 1000

        # Cross line around x0 along the given axis:
        char_distance = np.zeros(resolution)
        johnson = np.zeros(resolution)
        cross_line = np.mgrid[-sd/2:sd/2:resolution*1j]


        # Initialize E_int_t
        E_ind_t = np.zeros((3,1))

        for i in range(0,resolution):
            # Set the point
            x = x0 + cross_line[i]*sa
            # Calculate the electric field from the electrode at x
            E_ind = s.individual_potential(x, derivative=1)
            # Rotate the coordinate system so that you get the electric field along the trap modes
            E_ind_t = np.dot(mod_dir,np.matrix.transpose(E_ind[e_number]))
            # Calculate characteristic distance:
            char_distance[i] = 1/(E_ind_t[sf_number])
            # Calculate Johson noise
            johnson[i] = 4*kb*T*R/((char_distance[i]*L)**2)

        # Plot Johnson noise as a function of the ion's position
        plt.close('all')
```

```
fig, ax2 = plt.subplots(1, 1, figsize=(10, 6))
ax2.plot(cross_line, johnson, 'b',lw=5)
ax2.set_xlabel('$z$ ($10^{-6}$m)', fontsize=20)
ax2.set_ylabel('$S_\mathrm{E}}$ ($\mathrm{V^{2}m^{-2}Hz^{-1}}$)', fontsize=20)
ax2.tick_params(axis='x', labelsize=15)
ax2.tick_params(axis='y', labelsize=15)
plt.rc('font', size=15)
plt.show()
```

Bibliography

[1] Moore, G. E. Progress in Digital Integrated Electronics. *IEEE, IEDM Tech. Digest* 11 (1975).

[2] Waldrop, M. M. More than moore. *Nature* **530**, 114 (2016).

[3] Wecker, D., Bauer, B., Clark, B. K., Hastings, M. B. & Troyer, M. Gate-count estimates for performing quantum chemistry on small quantum computers. *Phys. Rev. A* **90**, 022305 (2014).

[4] Ladd, T. D. *et al.* Quantum computers. *Nature* **464**, 45 (2010).

[5] Feynman, R. P. Simulating physics with computers. *International Journal of Theoretical Physics* **21**, 467 (1982).

[6] Ortiz, G., Gubernatis, J. E., Knill, E. & Laflamme, R. Quantum algorithms for fermionic simulations. *Phys. Rev. A* **64**, 022319 (2001).

[7] Häffner, H., Roos, C. F. & Blatt, R. Quantum computing with trapped ions. *Physics Reports* **469**, 155 (2008).

[8] Cirac, J. I. & Zoller, P. Quantum Computations with Cold Trapped Ions. *Phys. Rev. Lett.* **74**, 4091 (1995).

[9] Sørensen, A. & Mølmer, K. Entanglement and quantum computation with ions in thermal motion. *Phys. Rev. A* **62**, 22311 (2000).

[10] Cirac, J. I. & Zoller, P. A scalable quantum computer with ions in an array of microtraps. *Nature* **404**, 579 (2000).

[11] Kumph, M. *2D Arrays of Ion Traps for Large Scale Integration of Quantum Information Processors*. Ph.D. thesis, Universität Innsbruck (2015).

[12] Kielpinski, D., Monroe, C. & Wineland, D. J. Architecture for a large-scale ion-trap quantum computer. *Nature* **417**, 709 (2002).

[13] Kumph, M., Brownnutt, M. & Blatt, R. Two-dimensional arrays of radio-frequency ion traps with addressable interactions. *New J. Phys.* **13**, 073043 (2011).

[14] Knoop, M., Marzoli, I. & Morigi, G. (eds.) *Ion Traps for Tomorrow's Applications* (IOS Press, 2013).

[15] Monroe, C. & Kim, J. Scaling the ion trap quantum processor. *Science* **339**, 1164 (2013).

[16] Hughes, M. D., Lektisch, B., Broersma, J. A. & Hensinger, W. K. Microfabricated ion traps. *Contemporary Physics* **52**, 505 (2011).

[17] Brownnutt, M., Kumph, M., Rabl, P. & Blatt, R. Ion-trap measurements of electric-field noise near surfaces. *Rev. Mod. Phys.* **87**, 1419 (2015).

[18] Monroe, C. *et al.* Resolved-Sideband Raman Cooling of a Bound Atom to the 3D Zero-Point Energy. *Phys. Rev. Lett.* **75**, 4011 (1995).

[19] Daniilidis, N. *et al.* Surface noise analysis using a single-ion sensor. *Phys. Rev. B* **89**, 245435 (2014).

[20] Harlander, M. *Architecture for a Scalable Ion-trap quantum computer*. Ph.D. thesis, Universität Innsbruck (2012).

[21] Johnson, J. B. Thermal agitation of electricity in conductors. *Phys. Rev.* **32**, 97 (1928).

[22] Nyquist, H. Thermal agitation of electric charge in conductors. *Phys. Rev.* **32**, 110 (1928).

[23] Pavuna, D. & Cyrot, M. *Introduction to superconductivity and High-Tc Materials* (World Scientific Publishing Co. Pte. Ltd., 1992).

[24] Kadin, A. M. *Introduction to Superconducting Circuits* (Wiley-Interscience, 1999).

[25] Fischer, E., Osberghaus, O. & Paul, W. Ein Ionenkäfig. *Forsch. MBer. d. Wirtsch. Ministeriums Nordrhein-Westfalen* **415** (1958).

[26] Paul, W. Electromagnetic traps for charged and neutral particles. *Rev. Mod. Phys.* **62**, 531 (1990).

[27] Meixner, J., Schäfke, F. & Wolf, G. *Mathiuesche Funktionen und Sphäroidfunktionen* (Springer-Verlag, 1980).

[28] Gosh, P. K. *Ion Traps* (Oxford University Press, 1995).

[29] Niedermayr, M. *Cryogenic surface ion traps*. Ph.D. thesis, Universität Innsbruck (2015).

[30] Roos, C. F. *Controlling the quantum state of trapped ions*. Ph.D. thesis, Leopold-Franzens-Universität Innsbruck (2000).

[31] Foot, C. J. *Atomic Physics* (Oxford, 2005).

[32] James, D. F. V. Quantum dynamics of cold trapped ions with application to quantum computation. *Appl. Phys. B.* **66**, 181 (1998).

[33] Jin, J. & Church, D. A. Precision lifetimes for the Ca^+ $4p^2P$ levels: Experiment challenges theory at the 1% level. *Phys. Rev. Lett.* **70**, 3213 (1993).

[34] Barton, P. A. *et al.* Measurement of the lifetime of the $3d^2D_{5/2}$ state in $^{40}Ca^+$. *Phys. Rev. A* **62**, 032503 (2000).

[35] Lechner, R. *Photoionisation of ^{40}Ca with a frequency-doubled 422 nm laser and a 377 nm laser diode*. Master's thesis, Universität Innsbruck (2010).

[36] Wineland, D. J. & Itano, W. M. Laser cooling of atoms. *Phys. Rev. A* **20**, 1521 (1979).

[37] Schmidt-Kaler, F. *et al.* Ground state cooling, quantum state engineering and study of decoherence of ions in Paul traps. *J. Mod. Opt.* **47**, 2573 (2000).

[38] Blatt, R. & Zoller, P. Quantum jumps in atomic systems. *Eur. J. Phys* **9**, 250 (1988).

[39] Berkeland, D. J., Miller, J. D., Bergquist, J. C., Itano, W. M. & Wineland, D. J. Minimization of ion micromotion in a Paul trap. *J. Appl. Phys.* **83**, 5025 (1998).

[40] Hite, D. A. *et al.* 100-fold reduction of electric-field noise in an ion trap cleaned with in situ argon-ion-beam bombardment. *Phys. Rev. Lett.* **109**, 103001 (2012).

[41] Turchette, Q. A. *et al.* Heating of trapped ions from the quantum ground state. *Phys. Rev. A* **61**, 063418 (2000).

[42] Daniilidis, N. *et al.* Fabrication and heating rate study of microscopic surface electrode ion traps. *New J. Phys.* **13**, 1 (2011).

[43] Allcock, D. T. C. *et al.* Reduction of heating rate in a microfabricated ion trap by pulsed-laser cleaning. *New J. Phys.* **13**, 123023 (2011).

[44] H. J. Metcalf, P. v. d. *Laser Cooling and Trapping* (Springer-Verlag, 1999).

[45] Niedermayr, M. *et al.* Cryogenic surface ion trap based on intrinsic silicon. *New J. Phys.* **16**, 113068 (2014).

[46] Onnes, H. K. The resistance of pure mercury at helium temperatures. *Comm. Phys. Lab. Univ. Leiden 120b* **120b** (1911).

[47] Meissner, W. & Ochsenfeld, R. Ein neuer Effekt bei Eintritt der Supraleitfähigkeit. *Naturwissenschaften* **21**, 787 (1933).

[48] Hammerl, G. *Neue Verfahren zur Optimierung von Bandsupraleitern*. Ph.D. thesis, Universität Augsburg (2004).

[49] Bednorz, J. G. & Muller, K. A. Possible High T_c Superconductivity in the Ba-La-Cu-O System. *Zeitschrift für Physik B* **64**, 189 (1986).

[50] Dai, P. *et al.* Synthesis and neutron powder diffraction study of the superconductor $HgBa_2Ca_2Cu_3O_{8+\delta}$ by Tl substitution. *Physica C* **243**, 201 (1995).

[51] Gao, L. *et al.* Superconductivity up to 164 K in $HgBa_2Ca_{m-1}Cu_mO_{2m+2+\delta}$ (m=1, 2, and 3) under quasihydrostatic pressures. *Phys. Rev. B* **50**, 4260 (1994).

[52] Drozdov, A. P., Eremets, M. I., Troyan, I. A., Ksenofontov, V. & Shylin, S. I. Conventional superconductivity at 203 kelvin at high pressures in the sulfur hydride system. *Nature* **525**, 73 (2015).

[53] Ekin, J. W. *Experimental Techniques for low-temperature measurements* (Oxford University Press, 2006).

[54] Semerad, R. data sheet hts coatings. http://www.ceraco.de/hts-films/ (2016).

[55] Madou, M. *Fundamentals of Microfabrication* (CRC Press, 1997).

[56] Jördens, R. Numerical tools for rf ion traps. https://github.com/nist-ionstorage/electrode (2016).

[57] Wesenberg, J. H. Electrostatics of surface-electrode ion traps. *Phys. Rev. A.* **78**, 1 (2008).

[58] Schmied, R. Electrostatics of gapped and finite surface electrodes. *New J. Phys.* **12**, 023038 (2010).

[59] Schmied, R. SurfacePattern: a Mathematica package for surface atom and ion traps. https://atom.physik.unibas.ch/people/romanschmied/code/SurfacePattern.php (2015).

[60] Schmied, R., Wesenberg, J. H. & Leibfried, D. Optimal surface-electrode trap lattices for quantum simulation with trapped ions. *Phys. Rev. Lett.* **102**, 2 (2009). 0902.1686.

[61] Chiaverini, J. & Sage, J. M. Insensitivity of the rate of ion motional heating to trap-electrode material over a large temperature range. *Phys. Rev. A.* **89**, 1 (2014).

[62] Labaziewicz, J. *et al.* Temperature Dependence of Electric Field Noise above Gold Surfaces. *Phys. Rev. Lett.* **101**, 180602 (2008).

[63] Allcock, D. T. C. *Surface-Electrode Ion Traps for Scalable Quantum Computing*. Ph.D. thesis, Hertford College Oxford (2011).

[64] den Otter, M. W. Approximate expressions for the capacitance and electrostatic potential of interdigitated electrodes. *Sensors and Actuators A* **96**, 140 (2002).

[65] Day, C. Basics and applications of cryopumps (2006).

[66] Brown, K. R. *et al.* Single-qubit-gate error below $\mathbf{10^{-4}}$ in a trapped ion. *Phys. Rev. A* **84**, 030303 (2011).

[67] Gandolfi, D., Niedermayr, M., Kumph, M., Brownnutt, M. & Blatt, R. Compact radio-frequency resonator for cryogenic ion traps. *Rev. Sci. Instrum.* **83**, 084705 (2012).

[68] Susheel Kalia, S.-Y. F. *Polymers at Cryogenic Temperatures* (Springer-Verlag, 2013).

[69] N. J. Simon, R. P. R., E. S. Drexler. Properties of Copper and Copper Alloys at Cryogenic Temperatures. *NIST Monograph* **177** (1992).

[70] Meschede, D. *Gerthsen Physik*, vol. 23 (Springer-Verlag, 2006).

[71] Keithley. *Model 2010 Multimeter User's Manual*, 5th edn. (2003).

[72] Brownnutt, M., Harlander, M., Hänsel, W. & Blatt, R. Spatially-resolved potential measurement with ion crystals. *Appl. Phys. B.* **107**, 1125 (2012).

[73] Harlander, M., Lechner, R., Brownnutt, M., Blatt, R. & Hänsel, W. Trapped-ion antennae for the transmission of quantum information. *Nature* **471**, 200 (2011).

[74] Hempel, C. *Digital quantum simulation, Schroedinger cat state spectroscopy and setting up a linear ion trap*. Ph.D. thesis, Universität Innsbruck (2014).

[75] Warring, U. *et al.* Techniques for microwave near-field quantum control of trapped ions. *Phys. Rev. A* **87**, 1 (2013).

[76] Warring, U. (2016), private communication.

[77] Jackson, J. D. *Classical Electrodynamics* (Wiley, 1998), 3rd edn.

[78] `http://ipython.org/notebook.html` (2016).

Leopold-Franzens-Universität Innsbruck

Eidesstattliche Erklärung

Ich erkläre hiermit an Eides statt durch meine eigenhändige Unterschrift, dass ich die vorliegende Arbeit selbständig verfasst und keine anderen als die angegebenen Quellen und Hilfsmittel verwendet habe. Alle Stellen, die wörtlich oder inhaltlich den angegebenen Quellen entnommen wurden, sind als solche kenntlich gemacht.

Die vorliegende Arbeit wurde bisher in gleicher oder ähnlicher Form noch nicht als Magister-/Master-/Diplomarbeit/Dissertation eingereicht.

_____ _____

Datum Unterschrift